Multinuclear Magnetic Resonance Spectroscopy in the Human Brain at Ultra High-field

Carolina Campanha Fernandes, MSc.

Thesis submitted to the University of Nottingham
for the degree of Doctor of Philosophy



Sir Peter Mansfield Imaging Centre
University of Nottingham
2017

"Recomeça...se puderes, sem angústia e sem pressa e os passos que deres, nesse caminho duro do futuro, dá-os em liberdade, enquanto não alcances não descanses, de nenhum fruto queiras só metade."
Miguel Torga

Abstract

In this thesis, new acquisition and analysis methods are described for multinuclear magnetic resonance spectroscopy (MRS) for the quantification of brain metabolites at ultra high magnetic field strengths (7 T).

An analytical model was derived for the optimisation of the stimulated echo acquisition mode (STEAM) sequence timing parameters for lactate detection. The effects of the chemical shift displacement artefact on the J-modulated signal for a weakly-coupled spin system were considered in the three applied directions of field gradients and the product operator formalism was used to obtain expressions for the signal modulation in each compartment of the excited volume. The validity of this model was demonstrated experimentally in a phantom and acquisitions with optimised parameters were performed on a healthy volunteer. The spectra acquired with an echo time (TE) of 144 ms and with an optimised mixing time and TE of 288 ms showed easily detectable lactate peaks in the normal human brain. Additionally, the acquisition with the longer TE resulted in a spectrum with less lipid/macromolecular (MM) contamination. The simulations demonstrated that the proposed analytical model is suitable for correctly predicting the resulting lactate signal. With the optimised parameters, it was possible to use a simple sequence with sufficient signal-to-noise ratio (SNR) to reliably distinguish lactate from overlapping resonances in a healthy brain at ultra high-field.

Estimation of metabolic changes during neuronal activation represents a challenge for *in vivo* MRS, especially for metabolites with low concentration and signal overlap, such as lactate. This thesis also includes work focused on the reliable quantification of lactate during a paradigm with 15 minutes of visual stimulation. The lipid and MM signals were significantly reduced by using a long TE (144 ms) sequence and the remaining MM signals in the vicinity of the lactate peak were individually fitted with simulated Lorentzian peaks, to ensure a good fit of the

inverted lactate doublet. Statistically significant changes in lactate (∼10%) and glutamate (∼3%) levels during stimulation were detected in the visual cortex and agree with previous measurements. Furthermore, the use of a prolonged stimulation period unveiled a distinctive metabolic response pattern, which can provide further insight into brain activation mechanisms.

^{13}C MRS combined with the infusion of labelled substrates is able to provide unique information on the relationship between neuroenergetics and brain function. However, the lack of sensitivity associated with the general complexity of ^{13}C experiments has hampered its widespread use for research into human brain disease. In this study, a new methodology for acquisition and analysis of ^{13}C signal is presented for the study of neuroenergetics and neurotransmission in a deep brain structure - anterior cingulate cortex - that is thought to play a major role in the processing of sensory information and can be impaired in patients with schizophrenia. *In vitro* testing was performed to evaluate the performance of the implemented sequence for signal localisation and polarisation transfer, both proving adequate for the intended purpose. *In vivo* data were acquired in four subjects, one diagnosed with early schizophrenia, with a protocol which involved 60 minutes of infusion of [1-^{13}C]glucose. Turnover curves for the labelled products were generated from the dynamic ^{13}C spectra with a temporal resolution of 10 minutes and were in agreement with the ones obtained from rodent experiments. Therefore, the feasibility of ^{13}C experiments for the study of psychosis was here demonstrated, taking advantage of the increase in SNR at ultra high-field for determination of metabolic fluxes.

Keywords: magnetic resonance spectroscopy, ultra high-field, chemical shift displacement artefact, lactate, brain metabolism, visual stimulation, ^{13}C magnetic resonance spectroscopy.

Acknowledgements

This thesis is the result of the dedication and support of colleagues, friends and family; each in their own way contributed to the feeling of accomplishment at the end of this journey.

First of all, to my supervisor from the University of Lisbon, Eduardo Ducla-Soares, who has guided me for the last 10 years. His classes developed my passion for Magnetic Resonance and inspired me to pursue a PhD. His words of encouragement were always present, even when I was no longer his student. Obrigada, Professor!

To my supervisor at the Sir Peter Mansfield Imaging Centre, Peter Morris, who I am very thankful for giving me the opportunity to spend the last few years unravelling the enigmas of Spectroscopy with someone that contributed so much to the field.

To Chen and Bernard, my post-docs and friends, who supported me, taught me, and were always present in my times of need to fight against the 7 T's own will. Two of the greatest scientists and spectroscopists I have ever met! And to Carlos, who supervised me during his stay in Nottingham and provided precious advice in Portuguese, which made that period even more enjoyable.

To all those who were part of the Marie Curie program that made this such a pleasurable experience, one that I will never forget. In particular to my fellows Catarina and Nick. To Catarina, who I happen to have been friends with for 10 years and counting; it was incredible to share this experience with a fellow countrywoman and friend. And to Nick, who was also my desk neighbour and a constant up-lifting presence in Nottingham and abroad.

To all Sir Peter Mansfield Imaging Centre members that always made me feel so welcome and made this period one of the best of my life. We are truly a big family! In particular, to Clémentine, confidant of PhD struggles and partner in film nights, and to Ben Hunt, one of the best sources of advice during these years.

To all my Portuguese friends, whether in Portugal or in the UK that brought and kept a piece of my country here. To my family, Vó, Cristina, Vera, and André, who always made the return to Portugal something to look forward to. Obrigada por tudo! To Gill, for your kindness and friendship, providing me with a home away from home.

Finally, to the people who had the greatest influence on my happiness during these years, my boyfriend Ben and my parents (and Jarvis). To Ben, the largest source of love and support at the office and at home. I feel very privileged that I can share all parts of my life and form a "Power Couple" with you! To my parents, whose love transcends any border and who always made sure I could feel it here. I owe all my achievements to you. Amo-vos a todos!

Contents

1 Scope of the thesis **1**

2 Basic principles of nuclear magnetic resonance **4**
2.1 Classical description of spins 4
2.2 Quantum mechanical description of spins 6
2.3 Macroscopic magnetisation 9
2.4 Time evolution of the magnetisation: Bloch equations 10
2.5 Effect of RF pulses 11
2.6 Effect of relaxation 14

3 Fundamentals of magnetic resonance spectroscopy **21**
3.1 The origin of the MRS signal 21
3.1.1 Effect of spin interactions in MRS 24
3.1.1.1 Chemical shift 25
3.1.1.2 Scalar coupling 26
3.2 *In vivo* applications of MRS 29
3.2.1 Brain MRS in clinical practice 31
3.2.2 Study of neuroenergetics and neurotransmission 32
3.3 MRS techniques 34
3.3.1 Data acquisition 35
3.3.1.1 Spatial localisation 35
3.3.1.2 Water suppression 45
3.3.1.3 Techniques to reduce outer volume contamination . 47
3.3.1.4 Techniques to improve B_1 and B_0 homogeneity . . 48
3.3.1.5 Sensitivity 50
3.3.2 Data post-processing 51
3.3.2.1 Truncation 51
3.3.2.2 Apodisation 52
3.3.2.3 Zero filling 52
3.3.2.4 Phase and frequency correction 53
3.3.3 Spectral quantification 54

4 The effect of the chemical shift displacement artefact on the ^{1}H lactate signal **63**
4.1 Introduction 63
4.2 Theory 65
4.3 Methods 69

4.4 Results . . . 70
4.5 Discussion . . . 72

5 Investigation of cerebral metabolic changes during a prolonged visual stimulus using ^{1}H MRS 80
5.1 Introduction . . . 80
5.2 Methods . . . 83
5.2.1 MR measurements . . . 83
5.2.2 Data processing . . . 86
5.3 Results . . . 89
5.4 Discussion . . . 91

6 *In vivo* ^{1}H-localised ^{13}C MRS for deep human brain applications 99
6.1 Introduction . . . 99
6.2 Methods . . . 101
6.2.1 Sequence design . . . 101
6.2.2 MR measurements & data processing . . . 107
6.2.2.1 Phantom experiments . . . 107
6.2.2.2 Human experiments . . . 109
6.3 Results . . . 113
6.3.1 Phantom experiments . . . 113
6.3.2 Human experiments . . . 114
6.4 Discussion . . . 115

7 Final remarks 125

Appendix 130

Chapter 1

Scope of the thesis

Magnetic resonance spectroscopy (MRS) is a non-invasive technique that allows for simultaneous detection of numerous metabolites in a defined region of the body. In the specific case of brain MRS, this constitutes an invaluable source of information for the identification of the key mechanisms involved in a variety of neurological and psychiatric diseases, as well as in the response to external stimuli and in aging.

Despite being possible to perform MRS on any nucleus with a magnetic moment, the most metabolically relevant nuclei are ^{1}H, ^{13}C, ^{31}P and ^{23}Na. The focus of this thesis is on ^{1}H and ^{13}C MRS.

^{1}H currently remains the most employed nucleus in MRS, due to its high sensitivity. Since almost all metabolites contain ^{1}H, ^{1}H MRS is a convenient method to evaluate physiological alterations of important compounds.

In contrast to ^{1}H, in which the metabolites of interest have absorption peaks in a narrow chemical shift range, ^{13}C MRS is generally characterised by its high spectral resolution. The limiting factor for its use is the low sensitivity and natural abundance, thus it is normally necessary to use a ^{13}C-labelled substrate infusion to observe the generated labelled metabolic products. Although more technically and experimentally challenging than ^{1}H MRS, ^{13}C MRS remains a powerful tool for studying neurochemistry.

The introduction of ultra high-field systems (higher than 3 T) has led to a more accurate quantification of low concentration and poorly resolved metabolites, as a result of the increase in signal intensity and spectral resolution. However, the use of higher fields has also imposed additional constraints, especially regard-

ing data acquisition. Moreover, these technological advances do not guarantee a proper detection and quantification of brain metabolites. For example, even at ultra high-field accurate quantification of lactate remains challenging, due to its low concentration in the brain in normal conditions and overlap with other resonances.

The aim of the work described in this thesis was to develop methodologies focused on data acquisition, post-processing and spectral quantification compatible with ultra high-field, taking advantage of its benefits and attempting to circumvent its obstacles.

Chapter 2 provides a physical background for the nuclear magnetic resonance (NMR) theory, which forms the basis of the MRS signal generation and detection. In chapter 3, the focus is turned to MRS, more specifically on the details of the available techniques for spectral acquisition, post-processing and metabolite quantification. These two chapters provide the necessary information for the understanding of the subsequent experimental chapters.

One of the major limitations of ultra high-field MRS is the exacerbation of the chemical shift displacements artefacts, which can lead to the cancellation of the coupled spin system's signal if the sequence timing is not optimised. Chapter 4 describes the derivation of an analytical model for the characterisation of the coupled-^{1}H MRS signal under the effect of these artefacts for the optimisation of the stimulated echo acquisition mode (STEAM) sequence timings in order to improve the detection of lactate.

An accurate quantification of lactate is especially crucial in functional ^{1}H MRS experiments, where signal intensity is traded off for temporal resolution. In chapter 5, a complete methodology is described for the measurement of the changes in concentration of this metabolite during visual stimulation.

Brain metabolism can also be investigated using ^{13}C MRS, which provides the possibility of assessing the dynamics of glucose metabolism and measuring cycle rates related to neurotransmission and neuroenergetics. Chapter 6 demonstrates the feasibility of performing dynamic ^{13}C MRS in a deep brain region at ultra high-field.

Finally, in chapter 7 final remarks on the work presented in this thesis are given

and opportunities for future methodological development in these areas are suggested.

Chapter 2

Basic principles of nuclear magnetic resonance

Nuclear magnetic resonance (NMR) is the study of the magnetic properties and energy states of nuclei, through the examination of the interactions between a radiofrequency (RF) magnetic field and matter to identify and characterise molecular systems. In this chapter, the basic description of the phenomenon of NMR is given, providing a physical background for the following chapters, in which NMR is used for biomedical applications, and more specifically in magnetic resonance spectroscopy (MRS).

NMR can be described through a classical or quantum mechanical approach. However, only with quantum mechanics it is possible to obtain a complete quantitative description of the NMR phenomenon; the classical description is mainly used for the understanding of the NMR principles at a macroscopic level.

2.1 Classical description of spins

The rotation of a particle with mass m on a circular orbit with radius r, with a constant velocity v, is described using the orbital angular momentum:

$$\vec{L} = \vec{r} \times \vec{p} = rmv\vec{n}, \tag{2.1}$$

where $\vec{p}$ is the linear momentum vector and $\vec{n}$ the unit vector normal to the plane encircled by the object. The angular momentum can be changed with an external rotational force, torque, $\vec{T}$, which is defined as the cross product of force and the

orbital radius of the particle:

$$\vec{T} = \vec{r} \times \vec{F} = \vec{r} \times \frac{d\vec{p}}{dt} = \frac{d\vec{L}}{dt}. \tag{2.2}$$

If the rotating object is carrying a charge q, a current loop is created, inducing a magnetic dipole moment $\vec{\mu}$, described as the product of the current and the area of the circular orbit:

$$\vec{\mu} = \left[\frac{qv}{2\pi r}\right] \pi r^2 \vec{n}. \tag{2.3}$$

Using the relation of Eq. 2.1, it is possible to express the magnetic moment as a function of the orbital angular momentum:

$$\vec{\mu} = \frac{q}{2m}\vec{L} = \gamma\vec{L}, \tag{2.4}$$

where γ is the gyromagnetic ratio of a particle. In the next subsection, it is shown that this relation can also be obtained using a quantum mechanical approach.
When the rotating object is placed in a static magnetic field $\vec{B_0}$, the torque from Eq. 2.2 can be described as:

$$\vec{T} = \vec{\mu} \times \vec{B_0}. \tag{2.5}$$

From Eqs. 2.2, 2.4 and 2.5, we obtain:

$$\frac{d\vec{\mu}}{dt} = \gamma\vec{\mu} \times \vec{B_0}. \tag{2.6}$$

The torque keeps the angle between the magnetic field and the magnetic moment constant, thus making it precess around $\vec{B_0}$ (Figure 2.1). Equivalently,

$$\frac{d\vec{\mu}}{dt} = \vec{\mu} \times \vec{\omega_0}, \tag{2.7}$$

yielding the Larmor equation $\omega_0 = \gamma B_0$, which expresses the frequency of this precession (ω_0) as a function of the magnitude of the magnetic field.
The potential energy associated with this torque is given by:

$$E = -\vec{\mu} \cdot \vec{B_0} = -\mu B_0 cos\theta, \tag{2.8}$$

where θ is the angle between the magnetic moment and the magnetic field. The energy is minimum (for positive γ) when the magnetic moment is parallel to the magnetic field ($-\mu B_0$), and maximum when both are antiparallel with respect to each other ($+\mu B_0$). In the next section, it will be shown how a quantum mechanical approach can be used to describe the interaction between electromagnetic waves and nuclear spins.

2.2 Quantum mechanical description of spins

In the quantum mechanical approach, a particle is characterised by the spin angular momentum $\vec{S}$. In contrast to the orbital angular momentum, the spin angular momentum is a vector independent of the particle motion or position. Its magnitude is given as:

$$|\vec{S}| = \hbar\sqrt{I(I+1)}, \tag{2.9}$$

where $\hbar$ is the Planck constant divided by 2π and I is the spin quantum number. The direction of the spin angular momentum can be changed with the influence of an external force. For example, in the absence of an external magnetic field, the spins orientate randomly. In the presence of a magnetic field, the spin angular momentum is quantised, and thus limited to discrete orientations and energy values given by:

$$S_z = \hbar m, \tag{2.10}$$

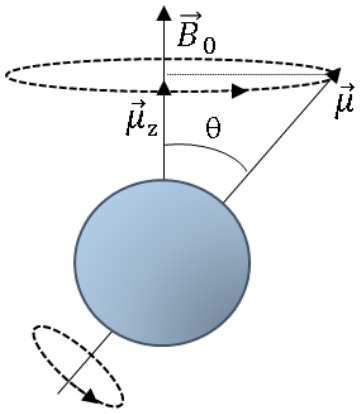


Figure 2.1: Schematic diagram of the precessional motion of a particle with magnetic moment $\vec{\mu}$ about an external magnetic field $\vec{B}_0$ applied in the z direction, with orientation θ from the μ vector (positive γ).

where m is the quantum number:

$$m = -I, -I+1, ..., I-1, I. \tag{2.11}$$

Therefore, a total of $2I+1$ distinct energy states are allowed. For protons, neutrons and electrons, the spin quantum number is 1/2. For nuclei, I can be deduced using the atomic mass and charge number, according to the following:

1. For nuclei with an odd mass number, I is half integer (1/2, 3/2, 5/2, e.g., ^{1}H, ^{13}C, ^{15}N, ^{31}P, ^{23}Na);

2. For nuclei with an even mass and charge number I is zero (e.g. ^{12}C, ^{16}O, ^{32}S);

3. For nuclei with an even mass number and odd charge number I is an integer number (e.g. ^{2}H, ^{14}N).

In NMR, nuclei with zero net spin are invisible. The main properties of a nucleus to consider for NMR experiments are listed in Table 2.1, which include spin, gyromagnetic ratio and natural abundance. Both gyromagnetic ratio and natural abundance affect the magnitude of the available magnetisation that will give rise to a measurable signal. This relation will be discussed in the next subsection.
By analogy with Eq. 2.4, spins are also characterised by a magnetic moment $\vec{\mu}$ which is related to their spin angular momentum:

$$\vec{\mu} = \gamma \vec{S}. \tag{2.12}$$

By combining Eqs. 2.10 and 2.12, we are able to obtain:

$$\mu = \gamma \hbar m. \tag{2.13}$$

In the quantum mechanical approach, the magnetic energy defined in Eq. 2.8 for the different states of a nucleus within an external magnetic field $\vec{B_0}$ along the z direction is given by:

$$E = -\mu_z B_0 = -\gamma \hbar m B_0. \tag{2.14}$$

Nucleus	Spin I	Gyromagnetic ratio γ ($MHzT^{-1}$)	Natural abundance (%)
^{1}H	1/2	42.577	99.985
^{13}C	1/2	10.708	1.108
^{31}P	1/2	17.254	100
^{23}Na	3/2	11.268	100

Table 2.1: List of important nuclei in NMR and their physical properties [1].

The distribution of $\vec{\mu}$ in the xy plane is random if a system is in equilibrium, thus $\mu_x = \mu_y = 0$. For a particle of spin $I = 1/2$, the observed energy is quantised in two values with $m = -1/2$ and $m = +1/2$, which correspond to an anti-parallel (highest energy) and parallel (lowest energy) orientation with respect to $\vec{B_0}$, respectively. For simplicity, the anti-parallel orientation is denoted as "spin-down" and the parallel orientation as "spin-up" (Figure 2.2).
The energy difference between the two states is as follows:

$$\Delta E = \gamma \hbar B_0 = \hbar \omega_0, \tag{2.15}$$

in which ω_0 is the Larmor frequency derived using the Planck relation. The resonance effect in NMR is achieved by application of an oscillating magnetic field, perpendicular to μ_z and at the Larmor frequency to induce a transition between energy levels.

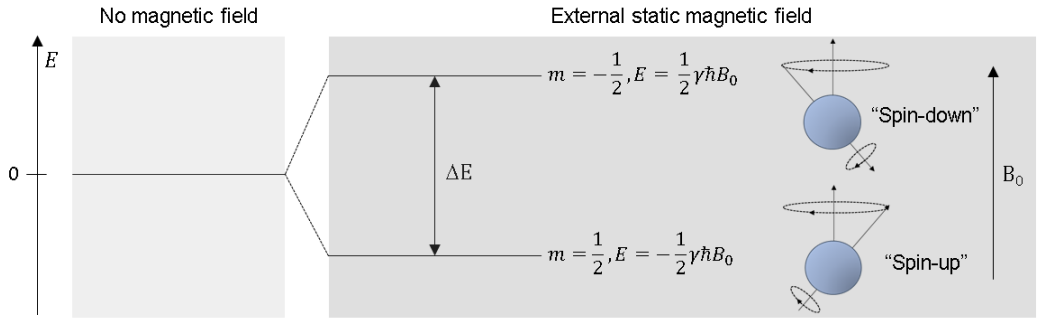


Figure 2.2: Illustration of the split into different energy levels E as a result of an applied external magnetic field in a particle with spin $I = 1/2$. The highest energy level corresponds to $m = -1/2$ and has an antiparallel orientation with regards to the magnetic field, while the lowest energy level is characterised by $m = 1/2$ and a parallel orientation.

2.3 Macroscopic magnetisation

The magnetisation $\vec{M}$ to which the NMR signal is proportional is given by the sum of the individual magnetic moments in a unit volume V:

$$\vec{M} = \frac{1}{V}\sum_{i=1}^{n}\vec{\mu_i}. \tag{2.16}$$

The sum is a vector sum and depends on the orientation of the individual spin angular momentum vectors. As such, to observe an NMR signal, the different levels - "spin-down" and "spin-up" - must be unevenly populated. In thermal equilibrium, the population of each state (P_m) is calculated according to the Boltzmann distribution, which gives the population distribution probability of a spin system with a certain energy and temperature T with respect to the total population:

$$P_m = \frac{N}{\sum_{m=-I}^{I}\exp\left(-\frac{E_m}{k_BT}\right)}\exp\left(-\frac{E_m}{k_BT}\right), \tag{2.17}$$

where N is the number of spins per unit volume and k_B is the Boltzmann constant. At body temperature (310.15 K, 37 °C - high temperature), the thermal energies are much higher than the nuclear magnetic energies, and thus there is only an extremely small excess of the population oriented parallel with respect to the magnetic field, which is the most energetically favourable. Therefore, the ratio of the two populations in the different spin states can be simplified using the expansion and truncation of the Taylor series, yielding:

$$\frac{P_{+1/2}}{P_{-1/2}} = \exp\left(\frac{\Delta E}{k_BT}\right) \sim 1 + \frac{\Delta E}{k_BT}. \tag{2.18}$$

Due to the small but measurable population difference, there is a net component of the magnetisation parallel to $\vec{B_0}$, along the z axis. From Eq. 2.16, the magnitude of the magnetisation at thermal equilibrium $\vec{M_0}$ is given by:

$$M_0 = \frac{1}{V}\sum_{i=1}^{n}\mu_i = P_{+1/2}\mu_{+1/2} + P_{-1/2}\mu_{-1/2} = \frac{1}{V}\frac{\gamma\hbar}{2}\left(P_{+1/2} - P_{-1/2}\right). \tag{2.19}$$

The population difference can be approximated to (see Chapter 6.1 of [2]):

$$P_{+1/2} - P_{-1/2} \sim \frac{P_{total}\Delta E}{2k_B T}, \tag{2.20}$$

which is added to Eq. 2.19 to yield:

$$M_0 = \frac{N\left(\gamma\hbar\right)^2 B_0}{4k_B T}, \tag{2.21}$$

using the definition of ΔE in Eq. 2.15. The equation for the equilibrium magnetisation contains important features related to the sensitivity of NMR experiments. For example, the quadratic dependence on the gyromagnetic ratio shows that nuclei with higher values of γ yield more intense NMR signals. A higher signal is also achieved at higher magnetic field strengths, shown by the linear dependence of M_0 on B_0. In addition, the number of spins in a sample, which is related to its natural abundance, is directly proportional to the equilibrium magnetisation. A more detailed explanation of the factors that affect the sensitivity of a NMR-based experiment will be given in subsection 3.3.1.5.

2.4 Time evolution of the magnetisation: Bloch equations

In order to observe the nuclear magnetisation, the precessional motion over time has to be detected. The time evolution of the magnetisation vector can be calculated through the Bloch equations, which are valid for any arbitrary magnetic field $\vec{B}$. From Eq. 2.6, it is possible to generalise to the case of macroscopic magnetisation, which corresponds to the summation of all the magnetic moments, as shown in Eq. 2.16, yielding:

$$\frac{d\vec{M}}{dt} = \vec{M} \times \gamma\vec{B}. \tag{2.22}$$

This is a system of three coupled linear differential equations:

$$\begin{aligned}\frac{dM_x}{dt} &= \gamma\left(M_y B_z - M_z B_y\right)\\ \frac{dM_y}{dt} &= \gamma\left(M_z B_x - M_x B_z\right)\\ \frac{dM_z}{dt} &= \gamma\left(M_x B_y - M_y B_x\right).\end{aligned} \tag{2.23}$$

The nuclear magnetisation can only be detected in the plane orthogonal to the $\vec{B_0}$ field (the detection coil is placed with its symmetry axis orthogonal to the static magnetic field). Therefore, the net longitudinal magnetisation (along z axis) needs to be rotated onto the transverse plane (xy plane). This can be achieved by the application of a time-varying magnetic field $\vec{B_1}$ in the transverse plane or more commonly referred to as an RF pulse, as it oscillates in the MHz range and has a limited duration. The process of rotating the magnetisation towards the detection axis is termed excitation and will be described in the next subsection with the use of the Bloch equations.

2.5 Effect of RF pulses

At thermal equilibrium, the phase of the spins is random, such that the net transverse magnetisation is zero. The application of the RF pulse has two effects: the two energy states will be more equally populated (transitions to the higher energy level occur) and the spins achieve a state of phase coherence. The first effect results in a decrease of longitudinal magnetisation and the second in the generation of transverse magnetisation.

The oscillating magnetic field is linearly polarised along the x axis and can be written as:

$$\vec{B_1} = 2B_{1,max}\cos\left(\omega_{rf}t\right)\vec{e_x}, \tag{2.24}$$

where $B_{1,max}$ is the maximum amplitude of the applied field and ω_{rf} its angular transmitter frequency. The linearly polarised field can be decomposed into two

circularly polarised fields rotating in opposite directions about the z axis:

$$\begin{aligned}\vec{B_1} = B_{1,max}\left[\cos\left(\omega_{rf}t\right)\vec{e_x} + \sin\left(\omega_{rf}t\right)\vec{e_y}\right] \\ + B_{1,max}\left[\cos\left(\omega_{rf}t\right)\vec{e_x} - \sin\left(\omega_{rf}t\right)\vec{e_y}\right].\end{aligned} \tag{2.25}$$

Only the component rotating with the magnetisation has a significant effect on the spins; the counter rotating component can be ignored, and the linearly polarised RF field acts as a circularly polarised field, however of lower amplitude:

$$\vec{B_1} = B_{1,max}\left[\cos\left(\omega_{rf}t\right)\vec{e_x} - \sin\left(\omega_{rf}t\right)\vec{e_y}\right]. \tag{2.26}$$

Modern scanners typically make use of quadrature transmit, in which two linearly polarised magnetic fields, perpendicular to each other and 90° out of phase (in time), are combined to generate a circularly polarised field. The advantage of using a circularly polarised field (quadrature mode) over a linearly polarised field is the reduction in RF drive power by factor of 0.5 to achieve the same B_1.
With the application of an RF field $\vec{B_1}$ and substituting B_z by B_0, the Bloch equations of Eq. 2.23 become:

$$\begin{aligned}\frac{dM_x}{dt} &= \gamma\left(M_yB_0 - M_zB_{1y}\right) \\ \frac{dM_y}{dt} &= \gamma\left(M_zB_{1x} - M_xB_0\right) \\ \frac{dM_z}{dt} &= \gamma\left(M_xB_{1y} - M_yB_{1x}\right).\end{aligned} \tag{2.27}$$

Until now, the Bloch equations have been described in a Cartesian frame fixed with respect to the laboratory (laboratory frame). However, it is more convenient to express these equations in a reference frame, which rotates about the $\vec{B_0}$ axis with the frequency ω, making the precession around the z axis appear stationary when $\omega = \omega_0$. The transformation of the magnetisation components to the rotating reference frame designated with the prime, (M'), is given as:

$$\begin{aligned}M'_x &= M_x\cos\left(\omega t\right) + M_y\sin\left(\omega t\right) \\ M'_y &= -M_x\sin\left(\omega t\right) + M_y\cos\left(\omega t\right) \\ M'_z &= M_z.\end{aligned} \tag{2.28}$$

Using this transformation, the Bloch equations of Eq. 2.27 can be described as below:

$$\begin{aligned}\frac{dM'_x}{dt} &= -\Omega M'_y - \gamma B'_{1,y} M'_z \\ \frac{dM'_y}{dt} &= \gamma B'_{1,x} M'_z + \Omega M'_x \\ \frac{dM'_z}{dt} &= \gamma B'_{1,y} M'_x - \gamma B'_{1,x} M'_y,\end{aligned} \tag{2.29}$$

where $\Omega = \omega_0 - \omega$, the resonance offset. Thus, in this reference frame, the precession frequency in the transverse plane appears to be reduced.

A convenient way to express the precessional motion of the magnetisation in this frame is to define an effective magnetic field vector, $\vec{B}_{eff}$, given as:

$$\vec{B}_{eff} = \left[B_{1,x} \cos\left(\omega_{rf} t\right), B_{1,y} \sin\left(\omega_{rf} t\right), \frac{\Omega}{\gamma} \right], \tag{2.30}$$

using the definition of $\vec{B}_1$ in Eq. 2.26. Its amplitude is calculated as below:

$$\begin{aligned}|\vec{B}_{eff}| &= \sqrt{\left[B_{1,x} \cos\left(\omega_{rf} t\right)\right]^2 + \left[B_{1,y} \sin\left(\omega_{rf} t\right)\right]^2 + \left(\frac{\Omega}{\gamma}\right)^2} \\ &= \sqrt{B_1^2 + \left[\frac{\Omega}{\gamma}\right]^2}.\end{aligned} \tag{2.31}$$

When the on-resonance condition is satisfied, i.e, when $\Omega = 0$, the magnetisation precesses about the $\vec{B}_{eff}$, which is, in this case, equal to the applied RF field (Figure 2.3a). The magnetisation, initially in the longitudinal direction, is rotated onto the transverse plane, by an amount expressed by the flip angle. The flip angle β depends on the amplitude of the RF field and it is calculated by integrating the rotation frequency of the magnetisation ω_1 during the pulse with duration τ:

$$\beta = \int_0^\tau \omega_1 dt = -\gamma \int_0^\tau B_1 dt = -\gamma B_1 \tau. \tag{2.32}$$

Immediately after the application of the RF pulse, the magnetisation appears static in the rotating reference frame. A $\beta = 90°$ will result in maximum transverse magnetisation, while $\beta = 180°$ inverts the magnetisation vector.

On the other hand, when the off-resonance effects are not negligible ($\Omega \neq 0$), the effective field has a z component and the magnetisation will precess about the

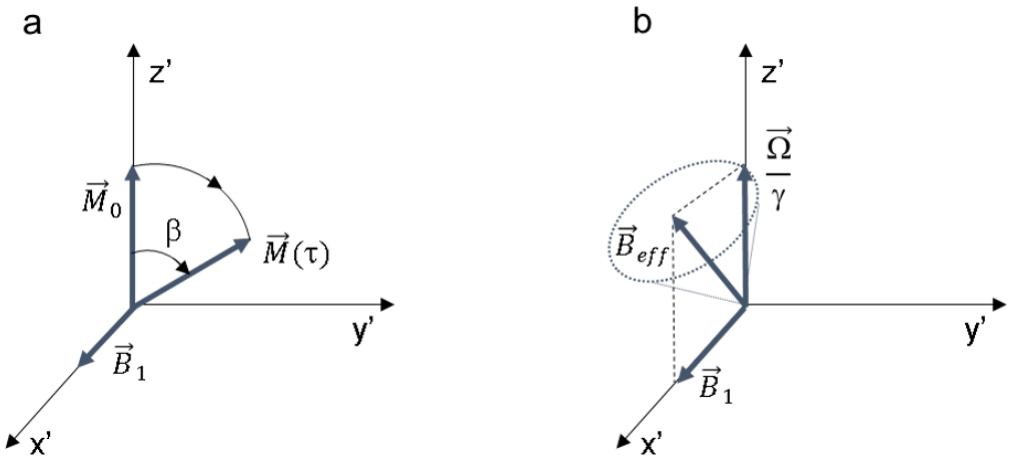


Figure 2.3: Schematic diagram of the effect of RF pulses in the rotating reference frame (x', y' and z'). An on-resonant (a) pulse $\vec{B_1}$ applied along the x axis tips the longitudinal magnetisation $\vec{M_0}$ onto the transverse plane. The final position of $\vec{M}$ depends on the pulse flip angle β and appears static in this frame. On the other hand, an off-resonant (b) irradiation yields a more complicated precessional motion around $\vec{B}_{eff}$, due to the contribution of the resonance offset Ω.

$\vec{B}_{eff}$ in a more complex manner (Figure 2.3b).

Although highly desirable, a homogeneously distributed RF transmit field cannot always be achieved, resulting in spatially varying flip angles (see Eq. 2.32). This can be circumvented with the use of adiabatic pulses. By manipulating the pulse amplitude and frequency, spins which experience different B_{eff} can be excited with the same flip angle. A more uniform excitation is then achieved as long as the adiabatic condition is met, i.e, the rotation frequency of the magnetisation during the pulse, γB_{eff}, is much larger than the change of direction of the effective magnetic field. More information on adiabatic pulses can be found in Chapter 6 of [3].

The solution of the Bloch equations presented above, which describes the NMR signal, excludes the effects of relaxation. These will be dealt in the next subsection.

2.6 Effect of relaxation

In an NMR experiment, the phenomenon which describes the return to the equilibrium state after a perturbation, e.g., application of an RF pulse, is denoted as relaxation. Two types of relaxation can be distinguished, spin-lattice, also known

as T_1 or longitudinal relaxation, and spin-spin, known as T_2 or transverse relaxation.

The longitudinal relaxation is related to the return to the initial magnetisation along the longitudinal axis. Another way to interpret this mechanism is to describe T_1 relaxation as the process of recovery of the Boltzmann population distribution of $m = -1/2$ and $m = +1/2$ spin states.

The time evolution of the longitudinal magnetisation is given by:

$$\frac{dM_z}{dt} = -\frac{M_z - M_0}{T_1}, \tag{2.33}$$

which can then be added to the Bloch equations described in the previous subsection. The solution of this equation is:

$$M_z = M_0 \left[1 - \alpha \exp\left(-\frac{t}{T_1}\right)\right], \tag{2.34}$$

where α is the inversion factor, which depends on the experiment: it takes the value of 1 if the magnetisation is initially in the transverse plane or 2 if the magnetisation is along -z, i.e, inverted. Therefore, T_1 relaxation can be defined as the time taken for longitudinal magnetisation to recover to 63% of its initial value following a 90° excitation. Figure 2.4a depicts the recovery of the initial magnetisation by T_1 relaxation.

The T_1 relaxation process is mediated by the energy exchange between nuclear spins and the surrounding matter (lattice). The rate with which the energy is exchanged is correlated with the overall rotational tumbling of the molecule in solution.

On the other hand, the motion of the molecules also induces a variation in the effective magnetic field experienced by the spins, which will lead to slightly different spin resonance frequencies. Thus, some spins will gain phase, while others will lose phase, leading to phase dispersion and a loss in phase coherence. This loss of coherence amongst the nuclei in the transverse plane is described by T_2 relaxation. In addition to these microscopic field variations caused by neighbouring spins, macroscopic field inhomogeneities create additional dephasing. Therefore, a relaxation constant T_2^* is introduced to take into account the intrinsic T_2 relax-

ation time of the tissue in addition to the one associated with field inhomogeneities $T_{2,\Delta B}$:

$$\frac{1}{T_2^*} = \frac{1}{T_2} + \frac{1}{T_{2,\Delta B}}. \tag{2.35}$$

Similarly to the longitudinal relaxation, the effects of the transverse relaxation can also be added to the Bloch equations in the form:

$$\frac{dM_{x/y}}{dt} = -\frac{M_{x/y}}{T_2^*}, \tag{2.36}$$

and the decay of the transverse magnetisation after a 90° RF pulse is described by the first order exponential decay:

$$M_{x/y} = M_0 \exp\left(-\frac{t}{T_2}\right). \tag{2.37}$$

T_2 relaxation can be considered to be the time for signal to decay, in a homogeneous static magnetic field, to 37% of its initial value, while T_2^* is the equivalent time, considering field inhomogeneities. In Figure 2.4b is depicted the exponential decay of the initial magnetisation through T_2 relaxation.

The influence of the random motion of the molecules within a magnetic field to their relaxation times is explained by the Bloembergen-Purcell-Pound theory

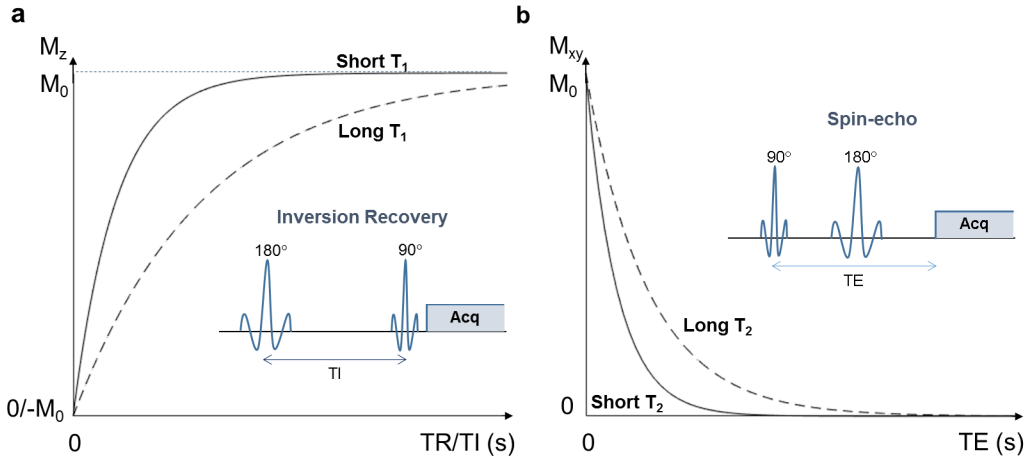


Figure 2.4: Recovery and decay of the initial magnetisation M_0 by T_1 (a) and T_2 (b) relaxation, respectively. The recovery of M_0 starts from 0, following a 90° excitation, and grows within the sequence TR or from -M_0, after an inversion pulse and builds-up with the TI. Measurement of T_1 relaxation times can be achieved by application of an inversion recovery sequence, repeated for several TIs. Measurement of T_2 relaxation times is performed with a spin-echo sequence for various TEs.

(BPP theory) [4]. Due to the Brownian molecular motion, the spins experience field fluctuations mediated by the interaction with neighbouring nuclei through dipolar coupling. These field variations can be described by the autocorrelation function, which is defined as a decaying exponential:

$$G(t) \propto \exp\left(-\frac{t}{\tau_c}\right), \tag{2.38}$$

in which τ_c is the correlation time, the time it takes for an average molecule to rotate one radian. The correlation time is proportional to the hydrodynamic volume (which relates to the size of the molecule), to the viscosity of the solution and decreases with the temperature. The autocorrelation function is converted to the frequency domain by applying a Fourier Transform to Eq. 2.38, resulting in the spectral density function, which provides a measure of the tumbling motion at a certain frequency:

$$J(\omega) = \int_0^\infty G(t) \exp(-i\omega t)\, dt \propto \frac{\tau_c}{1+\omega^2\tau_c^2}. \tag{2.39}$$

Therefore, for spin 1/2 nuclei, the dipolar longitudinal relaxation is given by:

$$\frac{1}{T_1} = \frac{3}{10}\left(\frac{\mu_0\hbar\gamma^2}{4\pi r^3}\right)^2 \left(J(\omega_0) + 4J(2\omega_0)\right), \tag{2.40}$$

where μ_0 is the vacuum permeability and r the distance between two spins. The dipolar transverse relaxation is expressed as:

$$\frac{1}{T_2} = \frac{3}{20}\left(\frac{\mu_0\hbar\gamma^2}{4\pi r^3}\right)^2 \left(3J(0) + 5J(\omega_0) + 2J(2\omega_0)\right). \tag{2.41}$$

Note the additional contribution from a low frequency component in Eq. 2.41, which causes the T_2 relaxation times to be less or equal to T_1 relaxation times. This is an expected consequence, as the return of the magnetisation to the longitudinal axis intrinsically causes the loss of magnetisation in the transverse plane. Figure 2.5 shows the relationship between relaxation times and the correlation time derived from Eqs. 2.39, 2.40 and 2.41 for ^{1}H spins at 3 T and 7 T, separated by 0.2 nm [5]. Efficient spin-lattice energy transfer requires that the frequencies

of the rotational tumbling match those of the nuclear spin transitions. Thus, T_1 relaxation is optimal if the average rate of motion corresponds to the Larmor precession frequency. At higher-fields, T_1 relaxation times increase, especially for molecules with higher correlation times. T_2 times decrease (faster decay) for less mobile molecules and the magnetic field strength has minimal influence on transverse relaxation processes.

To calculate the amount of magnetisation associated with a group of spins with a certain T_1 relaxation time during an NMR experiment, t in Eq. 2.34 is substituted by the repetition time (TR), which is the time between two consecutive excitation pulses. Similarly, the signal generated by a group of spins with a certain T_2 relaxation time is governed by the echo time (TE), which is the time between the excitation and the acquisition of the signal.

In order to choose the appropriate experimental parameters, it is crucial to have knowledge of the T_1 and T_2 relaxation times of the sample. Metabolite T_1 relaxation times can be measured using an inversion recovery (IR) sequence (Figure 2.4a), which consists of inverting the longitudinal magnetisation vector with a 180° pulse and rotating it to the transverse axis with a 90° pulse, so that the magnetisation can be measured. The pulse sequence is repeated several times with different values of the inversion time (TI), which corresponds to the time between

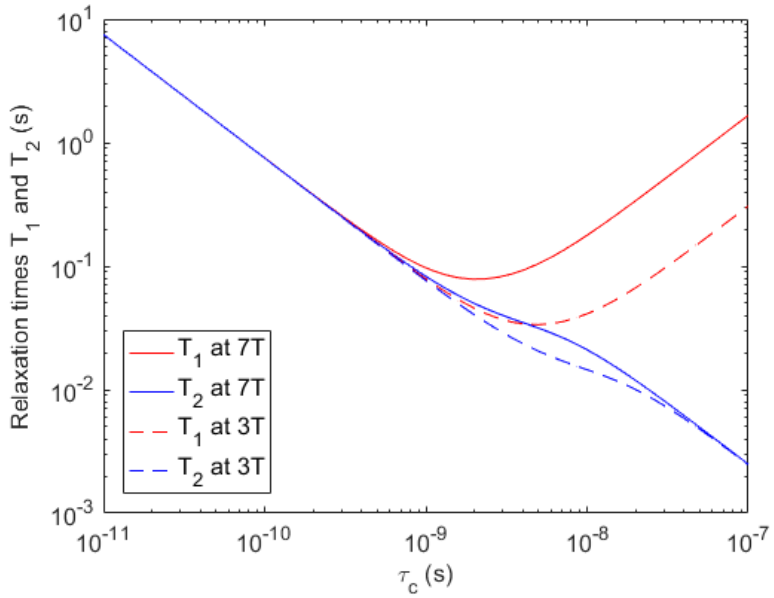


Figure 2.5: Relaxation times T_1 and T_2 at 3 T and 7 T as a function of the correlation time τ_c. Less mobile molecules are associated with higher correlation times.

inversion and excitation, to map the recovery of M_z, and the T_1 relaxation time is extracted from the curve. Metabolite T_1 relaxation times typically range from 940 ms to 2150 ms in the human brain at 7 T [6].

Measurement of T_2 relaxation times is carried out through a spin-echo experiment (Figure 2.4b), in which the contribution of the field inhomogeneities to T_2^* (see Eq. 2.35) can be refocused using the 180° refocusing pulse $TE/2$ seconds after the excitation. The T_2 relaxation time of a sample can be obtained by fitting the signal acquired from multiple spin-echo sequences with different TEs. Generally, metabolite T_2 relaxation times range from 61 ms to 200 ms in the human brain at 7 T [7].

Bibliography

[1] Robin A De Graaf. *In vivo NMR spectroscopy: principles and techniques*. John Wiley & Sons, 2013.

[2] E Mark Haacke, Robert W Brown, Michael R Thompson, and Ramesh Venkatesan. *Magnetic resonance imaging: physical principles and sequence design*, volume 82. Wiley-Liss New York, 1999.

[3] Matt A Bernstein, Kevin F King, and Xiaohong Joe Zhou. *Handbook of MRI pulse sequences*. Elsevier, 2004.

[4] Nicolaas Bloembergen, Edward Mills Purcell, and Robert V Pound. Relaxation effects in nuclear magnetic resonance absorption. *Physical review*, 73(7):679, 1948.

[5] Malcolm H Levitt. *Spin dynamics: basics of nuclear magnetic resonance*. John Wiley & Sons, 2001.

[6] Lijing Xin, Benoît Schaller, Vladimir Mlynarik, Huanxiang Lu, and Rolf Gruetter. Proton T_1 relaxation times of metabolites in human occipital white and gray matter at 7T. *Magnetic resonance in medicine*, 69(4):931–936, 2013.

[7] Małgorzata Marjańska, Edward J Auerbach, Romain Valabrègue, Van de Moortele, Gregor Adriany, Michael Garwood, et al. Localized ^{1}H NMR spectroscopy in different regions of human brain in vivo at 7T: T_2 relaxation times and concentrations of cerebral metabolites. *NMR in Biomedicine*, 25(2):332–339, 2012.

Chapter 3

Fundamentals of magnetic resonance spectroscopy

In the previous chapter, the principles of the nuclear magnetic resonance (NMR) signal origin were explained. Here, we focus on the translation of this signal into a spectrum and the techniques applied for its detection with minimal artefact contamination, post-processing for improving spectral quality and ultimately for reliable quantification. The current *in vivo* applications of magnetic resonance spectroscopy (MRS) are also discussed, concentrating on ^{1}H and ^{13}C MRS, which are the nuclei of interest in this thesis.

3.1 The origin of the MRS signal

Following a radiofrequency (RF) pulse with a phase of 0° and a flip angle θ at the offset Ω, the spins will oscillate at a specific frequency about the B_0 field vector, yielding a measurable signal in the xy plane. Simultaneously, the transverse relaxation effects will reduce the amplitude of this signal. Considering once again the temporal changes in the magnetisation in the rotating reference frame, we can decompose the magnetisation vector into two components:

$$\begin{aligned} M_y(t) &= M_0 \sin(\theta) \cos(\Omega t) \exp\left(-\frac{t}{T_2^*}\right) \\ M_x(t) &= -M_0 \sin(\theta) \sin(\Omega t) \exp\left(-\frac{t}{T_2^*}\right). \end{aligned} \tag{3.1}$$

With quadrature detection, it is possible to measure these components individually and then combine them into a complex signal:

$$\begin{aligned} S(t) &= M_y(t) - iM_x(t) \\ S(t) &= M_0 \sin(\theta) \exp(i\Omega t) \exp\left(-\frac{t}{T_2^*}\right), \end{aligned} \tag{3.2}$$

which is what we define as the free induction decay (FID) (Figure 3.1a). This signal is detected without action of an external perturbation, e.g., RF pulse (**free**), and is measured through the **induction** of a voltage (electromotive force) in the coil with its amplitude decaying over time (**decay**). To convert this time domain function into the frequency domain, and thus generate a spectrum, a Fourier Transform is applied to Eq. 3.2:

$$S(\omega) = \int_0^\infty S(t) \exp(-i\omega t)\, dt = M_0 \sin(\theta) \frac{1}{\frac{1}{T_2^*} - i(\Omega - \omega)}, \tag{3.3}$$

from which we can retrieve the real and imaginary parts:

$$\begin{aligned} Re[S(\omega)] &= M_0 \sin(\theta) \frac{\frac{1}{T_2^*}}{\left(\frac{1}{T_2^*}\right)^2 + (\Omega - \omega)^2} \\ Im[S(\omega)] &= M_0 \sin(\theta) \frac{\Omega - \omega}{\left(\frac{1}{T_2^*}\right)^2 + (\Omega - \omega)^2}. \end{aligned} \tag{3.4}$$

The real part of the spectrum is known as the Lorentz-shaped absorption signal (Figure 3.1b). This lineshape has a maximum at $\omega = \Omega$ and a full width at half maximum (linewidth) of $2/T_2^*$. This means that the faster the FID decay is (shorter T_2^*), the broader the linewidth becomes. However, the integral of the peak remains the same, as the amplitude decreases proportionally. The area under the curve provides essential information in MRS, since it is indicative of the number of nuclei in the sample. This will be further explained in subsection 3.3.3.

Conversely, the imaginary part of the spectrum corresponds to the dispersion signal (Figure 3.1b). In MRS, it is common to use the purely absorptive part of the signal to represent the spectrum. This is because the absorption lines fall off

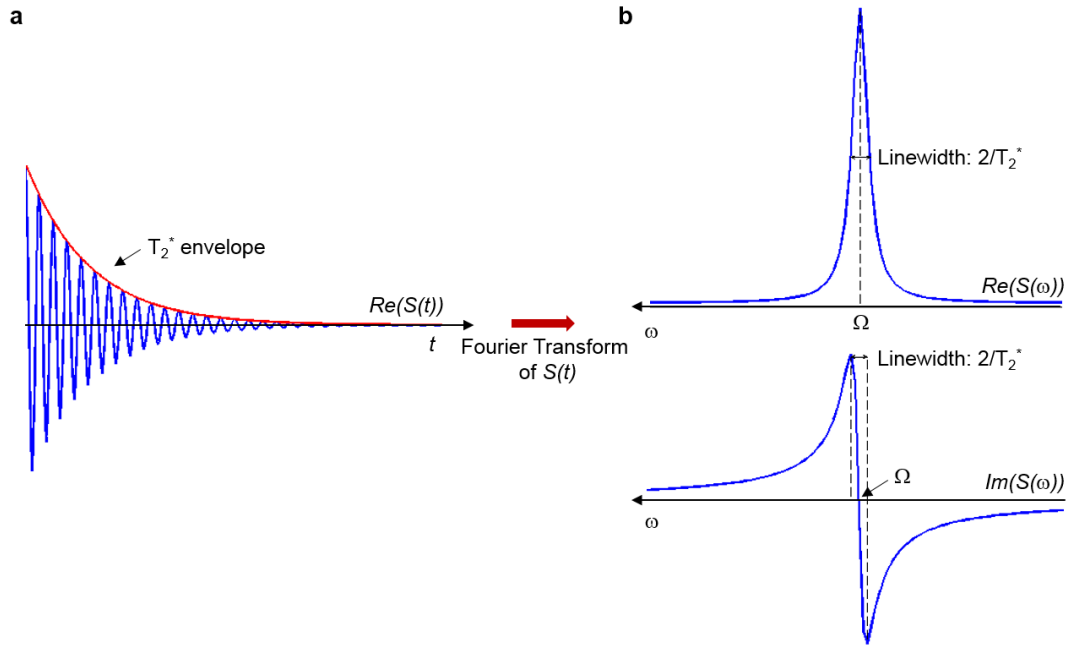


Figure 3.1: Illustration of the real part of the free induction decay (a) and the real and imaginary components of the Fourier Transformed complex free induction decay signal (b). The exponential curve in a) is referred to as T_2^* envelope.

with $1/(\Omega-\omega)^2$, instead of $1/(\Omega-\omega)$ for the dispersion lines, making the latter broader, and thus compromising the spectral resolution.

So far it has been assumed that the real part of *S(t)* is maximum at the start of the acquisition (t=0), while the imaginary part is zero (Eq. 3.2). However, it is common for a phase shift in the signal to occur, which makes the previous assumption not valid. Therefore, the addition of a phase shift ϕ in the signal of Eq. 3.2 is expressed as:

$$S(t) = M_0 \sin(\theta) \exp(i\Omega t) \exp(i\phi) \exp\left(-\frac{t}{T_2^*}\right). \tag{3.5}$$

This phase shift can be reversed through a process termed phase correction, which will be explained in subsection 3.3.2.4.

As expected, the FID acquisition parameters are closely related to the spectral features. The detected FID is sampled at N complex points, with equal spacing t (dwell time) over a duration T. In the frequency domain, the spacing between the same N points corresponds to the inverse of the duration T and the spectral width (SW), range of frequencies covered in the spectrum, is equal to the inverse

of the dwell time.

Therefore, in order to improve the spectral resolution, one option is to increase the acquisition time T. However, prolonged acquisition times can lead to increased noise levels and data storage. On the other hand, when the acquisition time is not long enough, the exponential decay is truncated, giving rise to ringing artefacts in the spectrum [1].

To expand the range of measured frequencies, it is necessary to decrease the dwell time, i.e., sample faster. According to the Nyquist criterion, the sampling rate $1/t$ or, equivalently, SW should be twice the maximum or minimum frequency arising from the sample, in order to avoid signal aliasing in the spectrum.

3.1.1 Effect of spin interactions in MRS

Depending on the type of interaction of the spins with the surrounding environment, different features will be evident in the spectrum. In general, it is possible to distinguish five types of interaction:

- Chemical shift, resulting from the effect of magnetic field shielding of the electron cloud on the nuclear spins;
- Dipolar coupling, which results from the direct interaction between spins;
- Scalar coupling, referring to the indirect interactions of nuclear spins with each other through electrons in chemical bonds;
- Quadrupolar coupling, representing the electric interactions of spins with $I > 1/2$ with the surrounding electric fields;
- Spin-rotation, expressing the interactions of the spins with the magnetic fields created by the rotational motion of molecules.

Despite being responsible for spin-spin relaxation, the dipolar coupling effect averages out to zero, since the rotational motion of molecules in liquids is fast. For the same reason, the contribution of the spin-rotation interaction mechanism is cancelled. Since the quadrupolar coupling vanishes for $I = 1/2$ spins, this type of interaction will not be described in this section. In this setting, chemical shift

and scalar coupling are the phenomena that most affect the *in vivo* MRS signal and, thus, will be further explained below. The chemical shift is predominantly an intramolecular interaction, although the intermolecular interaction also provides a significant contribution. The scalar coupling interaction is solely intramolecular [2].

3.1.1.1 Chemical shift

When a molecule is placed in a magnetic field, its electronic energy states are slightly altered, generating small magnetic field contributions at the nucleus, which will oppose or add to the externally applied field B_0. Hence, the precession frequency of a given atomic nucleus Ω, which is proportional to the net magnetic field experienced by it, can be characterised in terms of the shielding constant σ, a parameter generally expressed in parts per million (ppm):

$$\Omega = \gamma B_0 \left(1 - \sigma\right). \tag{3.6}$$

The electron density around each nucleus depends on the type of nucleus and the bonds in the molecule it pertains to, and consequently nuclei in different chemical environments will resonate at slightly different frequencies. This phenomenon constitutes the basis of MRS, allowing nuclei of different functional groups to be distinguished, thus providing information about the structure of molecules. This spectral dispersion is referred to as chemical shift. As the chemical shift measured in frequency units (Hz) is field dependent, higher magnetic field strengths lead to a better discrimination of the signals, and thus greater spectral resolution. In practical applications, it is convenient to make the chemical shift dependent on only the sample, and not the hardware. By convention, the field independent expression, in ppm, for the chemical shift δ is:

$$\delta = \frac{\Omega - \Omega_{ref}}{\Omega_{ref}} \times 10^6, \tag{3.7}$$

where Ω and Ω_{ref} are the resonance frequencies of a particular compound and of a reference compound, respectively. The reference compound should be chemically inert, independent of external variables (e.g., temperature) and provide a

strong signal. Tetramethylsilane (TMS) is usually used as a reference for ^{1}H and ^{13}C, although it cannot be set as an internal reference, since it is not found *in vivo* and it is not water soluble. For brain ^{1}H MRS, N-acetylaspartate (NAA) at 2.01 ppm is commonly chosen as internal reference as it is the highest peak in the healthy brain spectrum. Total creatine is the second highest peak, and thus is also often considered as an internal reference. For *in vitro* studies, 4,4-dimethyl-4-silapentane-1-sulfonic acid (DSS) is typically used in aqueous solutions, and its chemical shift is temperature and pH independent [3].

One of the drawbacks of ^{1}H MRS is the limited chemical shift dispersion, arising from the narrow chemical shift range (approximately 10 ppm) of the main molecules' resonances observed in the brain. As a result, several metabolites might be overlapped with each other, making their detection and, consequently, quantification challenging. This overlap can be mitigated by the use of stronger magnetic fields, as mentioned previously. On the other hand, ^{13}C MRS is generally characterised by a high spectral dispersion, with a measured chemical shift range of about 200 ppm.

3.1.1.2 Scalar coupling

Scalar coupling (J-coupling) arises from the fact that nuclei with magnetic moments can influence each other through electrons in chemical bonds. In uncoupled spin 1/2 systems, there is only one allowed transition, and the resonance is a singlet (Figure 3.2). In contrast, in a coupled system, where, e.g., two spins are covalently bound (A and X), the magnetic field experienced by the spin depends on the state of the coupled spin. Therefore, instead of only a "spin-up" or "spin-down" state, each of them can be either "spin-up" or "spin-down", leading to a system with four energy levels and multiple possible transitions between the levels. These transitions can be zero-, single- and double-quantum, where the spin quantum number changes by 0, ± 1 and ± 2, respectively. Only single-quantum transitions can be observed and in the spectrum these will yield multiple peaks. Figure 3.2 shows the splitting of the two resonances Ω_A and Ω_X into doublets, in which its peaks are separated by the J-coupling constant (J). J is independent of B_0, and it is expressed in Hz.

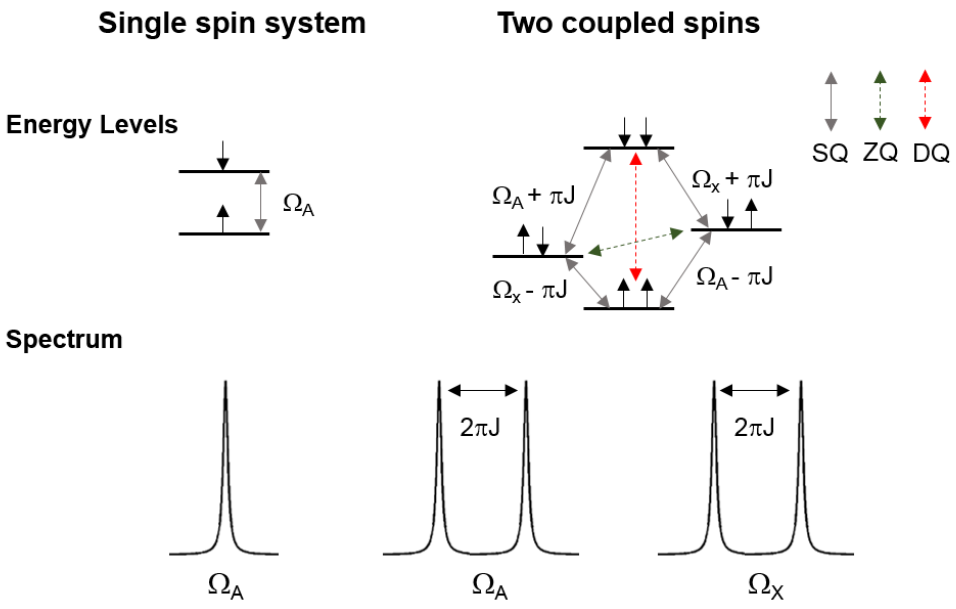


Figure 3.2: Representation of the scalar coupling effect on spins in uncoupled (single spin system - A) and coupled systems (A and X). Arrows indicate transitions between energy levels, which can be zero-(ZQ), single-(SQ) and double-quantum (DQ). Single-quantum transitions will result in peaks in the spectrum at the corresponding frequency. J refers to the spectral separation between both peaks of the split resonances (Ω_A and Ω_X).

Scalar coupling between magnetically equivalent nuclei, i.e., nuclei within the same chemical environment and thus possessing identical chemical shift and J-coupling constants relative to spins of other groups in the molecule, does not produce any splitting. In addition, the coupling strength rapidly decreases with increasing number of chemical bonds and can be ignored for four or more bonds.

The pattern of the splitting will depend on the magnitude of the coupling relative to the chemical shift difference of a spin system. Thus, a weakly-coupled spin system, denoted as AX, refers to the case when the condition $|2\pi J_{AX}| \ll |\Omega_A - \Omega_X|$ is valid, i.e., when the coupling is significantly smaller than the chemical shift difference. In contrast, the cases AB (strongly coupled two-spin system) and ABMX (four spin system, with two nuclei being strongly coupled to each other) apply when the referred condition does not hold.

In Figure 3.3, the line splitting pattern in an AX_n spin system is shown. In such a weakly-coupled spin system, the scalar coupling gives rise to $n+1$ lines, where n is the number of nuclei in the neighbouring group. As mentioned previously, the spin-spin coupling between magnetically equivalent nuclei does not appear in the

spectrum, hence the X spin spectrum will only contain two lines from the coupling with the single A spin. The relative intensity of the lines within a multiplet will follow the distribution described by Pascal's triangle.

Note that the J-coupling can be homonuclear (e.g.^{1}H-^{1}H) or heteronuclear (^{1}H-^{13}C). Typical values for ^{1}H-^{1}H are 280 Hz, when the protons are directly bound to each other and 0-12 Hz, when the protons are indirectly coupled across a common carbon atom (H-C-H) [4]. For ^{1}H-^{13}C, the J-coupling constant between these two nuclei, directly bound to each other, is 100-250 Hz, and 0-60 Hz for the H-C-^{13}C configuration [4].

The J-coupling pattern can provide useful information on the molecular structure. However, the line splitting can lead to overcrowded and complex spectra with lower signal-to-noise ratio (SNR), since the signal intensity is distributed over multiple peaks. To overcome this, a technique named decoupling can be used to remove the effect of homonuclear and heteronuclear couplings, which consists of the application of an RF field on-resonance with the coupled partner of the detected nuclear spin [5]. This technique leads to a simpler interpretation and increased sensitivity of the spectra, as the isolated lines in the multiplet are combined into a single line.

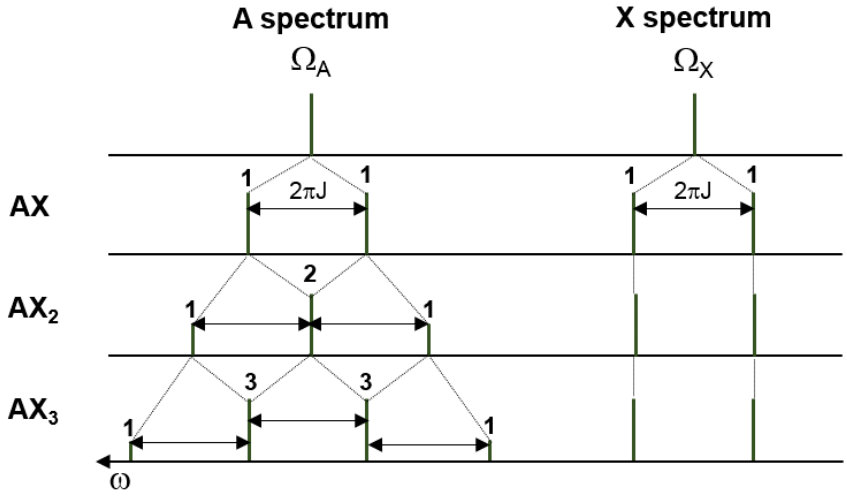


Figure 3.3: Example of line splitting in an AX$_n$ spin system with $n = 1$ to $n = 3$. In weakly-coupled spin systems spectra, J-coupling will give rise to $n+1$ lines, with the line intensities following the Pascal's triangle distribution. J corresponds to the frequency separation between the peaks of the split resonance.

3.2 *In vivo* applications of MRS

Ultra high-field MRS (e.g. 7 T) has improved the quantification of several metabolites due to the increase in SNR and spectral resolution. In the case of ^{1}H MRS, it made possible the simultaneous detection of 17 metabolites in the healthy brain with a short echo time (TE) acquisition [7]. The choice of pulse sequence for signal localisation and its implications for the spectrum will be discussed in subsection 3.3.1.1. An example of a typical short TE ^{1}H spectrum is depicted in Figure 3.4, where 11 of the 17 metabolites can be identified. These metabolites possess distinct functions, allowing us to study different biochemical processes in brain metabolism, which include brain energy metabolism - lactate, total creatine (composed of both creatine and phosphocreatine) and glucose, neuronal function - NAA, membrane metabolism - choline-containing compounds (total choline), neurotransmission - glutamate, glutamine, γ-aminobutyric acid (GABA) and aspartate or antioxidative/osmolyte processes - myo-inositol, glutathione and taurine.

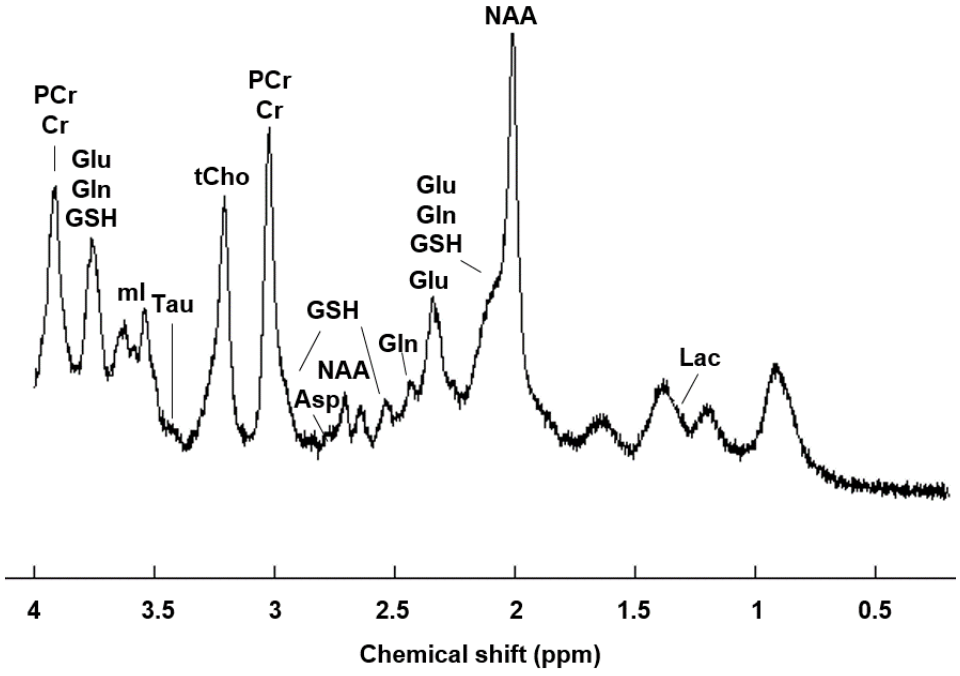


Figure 3.4: ^{1}H MRS spectrum acquired from the anterior cingulate cortex of a healthy volunteer with a short TE sequence at 7 T. 11 different metabolites can be identified in the spectrum. Note the significant overlap of some resonances even at ultra high-field. PCr - phosphocreatine, Cr - creatine, Glu - glutamate, Gln - glutamine, GSH - glutathione, mI - myo-inositol, Tau - taurine, tCho - total choline, Asp - aspartate, Lac - lactate.

Metabolite	**Spectral position (ppm)**	**Role**	**Concentration in normal brain (mM)**
Lactate	1.31, 4.10	Product of non-oxidative metabolism	0.2 - 1.0
Total Creatine	3.03, 3.91	Energy metabolism marker	Creatine (4.5 - 10.5) Phosphocreatine (3.0 - 5.5)
Glucose	3.23 - 3.88	Main source of energy in the brain	1.0 - 2.0
N-acetylaspartate	2.01, 2.49, 2.67, 4.38	Neuronal density and viability marker	7.5 - 17.0
Total choline	3.19, 3.50 - 4.05, 4.28	Phospholipid synthesis and degradation, reflecting membrane turnover, and thus cellular proliferation	0.5 - 2.5
Glutamate	2.04 - 2.35, 3.74	Major excitatory neurotransmitter	6.0 - 12.5
Glutamine	2.11 - 2.45, 3.75	Involved in neurotransmission processes	3.0 - 6.0
γ-aminobutyric acid	1.89, 2.28, 3.01	Major inhibitory neurotransmitter	1.0 - 2.0
Aspartate	2.65, 2.80, 3.89	Excitatory neurotransmitter	1.0 - 2.0
Myo-inositol	3.27 - 3.61, 4.05	Glial marker	4.0 - 9.0
Glutathione	2.15, 2.51, 2.93, 3.77	Important antioxidant, defence against oxidative stress	1.5 - 3.0
Taurine	3.25, 3.42	Osmoregulator and modulator of neurotransmitter action	2.0 - 6.0

Table 3.1: List of relevant metabolites detectable with ^{1}H MRS, their spectral positions [6], role in brain metabolism and concentration in normal adult human brain [1].

In Table 3.1, the spectral position of these metabolites in a ^{1}H spectrum is listed, as well as a description of their role in brain metabolism and their typical concentration in normal brain.

^{1}H MRS has been used in the clinical setting for diagnostic, prognostic and assessment of treatment response in several brain pathologies, as a complement of structural magnetic resonance imaging (MRI). Furthermore, it is a powerful research tool, specifically for probing biochemical mechanisms related to neuroenergetics and neurotransmission. The study of neuroenergetics and neurotransmission has contributed to our understanding of brain disease pathogenesis. For example, altered concentrations of metabolites involved in neurotransmission glutamate, glutamine and GABA have been observed in neurological and psychiatric diseases, such as major depressive disorder [8], schizophrenia [9], epilepsy [10], genetic disorders of metabolism [11] and neurodegenerative disorders [12]. In addition, the investigation of certain metabolic pathways involved in energy conversion and general neuronal activity is essential for the basic understanding of overall brain function.

In the next subsections, the value of brain MRS in the clinic and in research (in particular with respect to neuroenergetics and neurotransmission processes) environments, will be discussed.

3.2.1 Brain MRS in clinical practice

One of the medical areas in which ^{1}H MRS has been reported to have a clinical impact is oncology, where it has been shown to assist in differentiating tumour from other focal lesions, and also between metabolic changes induced by treatment and recurring tumour. In addition, it helps in the identification of optimal biopsy sites in heterogeneous gliomas. Typically, the metabolic feature observed in brain tumours is the combination of elevated total choline and decreased NAA. An increase in the lipid signal at 1.3 ppm has also been associated with higher grade tumours and poor survival prognostics [13, 14].

^{1}H MRS has also been part of the routine protocol in paediatric examinations. In the newborn infant, excess of lactate caused by hypoxia/ischemia can indicate brain injury, with consistently high lactate, being associated with poor outcome

[15]. Inherited metabolic disorders also significantly affect the paediatric population, in which the symptoms can arise due to the accumulation of metabolites that are neurotoxic or interfere with normal metabolism, or due to the decreased synthesis or transport of a compound. For example, a substantial increase in NAA levels has been consistently detected in patients with Canavan disease [16]. On the other hand, lower levels of total creatine are present in children with a creatine synthesis [17] or transporter defect [18].

In the case of demyelinating diseases, ^{1}H MRS provides important information on the biochemical composition of brain tissue to assist in the differential diagnosis of pathologies characterised by hypomyelination, white matter rarefaction and demyelination, each one associated with specific total choline/total creatine and NAA/total creatine ratios [19].

Despite not yet being included in routine protocols, ^{1}H MRS has the potential to contribute to patient management in a wide range of disorders, such as neurodegenerative diseases [20], epilepsy [21], and acute stroke and brain ischemia, with all of them characterised by a decrease in NAA in the affected region and the latter with concurrent increase of lactate in the core of the ischemic tissue [22].

Currently, clinical MRS is performed at 1.5 T or 3 T, and the most used localisation methods for single voxel spectroscopy are point-resolved spectroscopy (PRESS) [23] and stimulated echo acquisition mode (STEAM) [24, 25], which will be described in the next subsection.

Finally, ^{13}C MRS techniques have not evolved from a research tool into a clinical procedure, due to the complexity of the scanning pipeline and its high cost.

3.2.2 Study of neuroenergetics and neurotransmission

The brain is the organ of the human body with highest glucose consumption rate, relative to its weight, using up to 20% of the glucose supply [26]. Glucose metabolism constitutes the main mechanism for cellular energy generation, which ultimately results in the formation of adenosine triphosphate (ATP), the primary fuel for brain function, i.e., for the maintenance of cellular health and neurotransmission cycling.

In Figure 3.5, the neuronal and glial metabolic pathways are represented, as well as

the relationship between them, mediated via glutamate-glutamine cycling. Neuronal and glial cells play a distinct role in the brain. The neurons are mainly responsible for the neurotransmission processes, while the glial cells, amongst other functions, provide energy to neurons, regulate the interstitial space by removing toxic chemical compounds and recycle the neurotransmitters. Glucose is transported from the plasma to the brain tissue through the blood brain barrier via specific glucose transporters: GLUT1 mediates the transport into the glial cells, whereas GLUT3 promotes the transport to the neurons. GLUT3 is associated with a much higher transport rate than GLUT1, resulting in a larger uptake of glucose by the neurons [26]. In both cellular compartments, pyruvate is generated from the break down of glucose in the cytosol (glycolysis). Pyruvate is then converted into lactate non-oxidatively (without the use of oxygen) or into Acetyl-CoA, which is metabolised in the mitochondria and enters the tricarboxylic acid (TCA) cycle, whose processes consume oxygen. Both oxidative and non-oxidative pathways will ultimately produce ATP. In normal conditions, i.e., resting state, more than 90% of glucose consumption is oxidative [27]. Under different conditions, e.g., during brain activation, a mismatch between oxygen and glucose consumption occurs. A study carried out by Fox et al. [27] using positron emission tomography showed that during visual stimulation the cerebral blood flow and cerebral metabolic rate of glucose in the visual cortex increased approximately 50%, while the cerebral metabolic rate of oxygen only increased by 5%. Different theories have

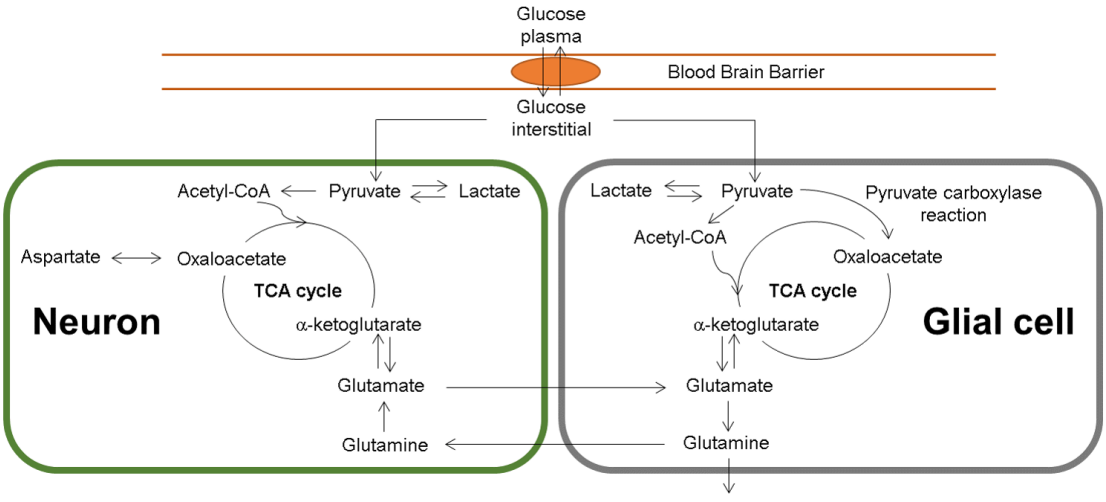


Figure 3.5: Diagram of the main metabolic pathways in the neurons and surrounding glial cells and interplay between both compartments. TCA cycle refers to the tricarboxylic acid cycle.

been proposed to describe the predominant pathways during brain activation, with no consensus being reached yet. To provide further insight into brain activation mechanisms, Chapter 5 will focus on the investigation of the metabolic changes during visual stimulation using functional MRS (fMRS).

As mentioned previously, part of the ATP generated will be used for neurotransmitter synthesis. Glutamate is the main excitatory neurotransmitter (Table 3.1) and is released by the pre-synaptic neurons. It then binds itself to the post-synaptic receptors to launch an action potential in the post-synaptic neuron, before being cleared from the synaptic cleft by the the surrounding glial cells to avoid excitotoxicity. In the glial cells, it is converted to glutamine, transported to the neurons and converted back to glutamate, replenishing the glutamate lost during neurotransmission. This series of steps, which begins with glutamate release in the synapse and ends in its resynthesis forms the glutamate-glutamine cycle. In resting state, approximately 80% of the ATP produced by oxidative glucose consumption is used by the glutamate-glutamine cycle [28]. Approximately 18% is used for the production of GABA [29], the main inhibitory neurotransmitter (Table 3.1).

Therefore, it is possible to obtain a quantitative description of the neuroenergetics and neurotransmission in the brain, through the measurement of the TCA and glutamate-glutamine cycle rates, respectively. To measure these rates, substrates labelled with ^{13}C (e.g. glucose) are infused into the bloodstream and the flux of this label into other metabolites in the neurons and glial cells can be quantified using ^{13}C MRS together with metabolic modelling. Chapter 6 will describe the development of an improved ^{13}C MRS acquisition strategy for deep-brain applications.

3.3 MRS techniques

Despite the increase in spectral resolution and SNR, several challenges arise at ultra high-field, especially with regards to data acquisition. These can be mitigated with the application of specific strategies, which will be discussed in this section, together with the essential methods required for signal detection in single voxel

MRS (localisation, water suppression and B_0 shimming). The most common sequences, and relevant to this thesis, used for voxel localisation - PRESS, STEAM, semiadiabatic localisation by adiabatic selective refocusing (sLASER) [30] and image selected *in vivo* spectroscopy (ISIS) [31] - will be explained. In addition, some of the techniques used at the post-processing level to improve spectral quality will be described below, as well as the criteria to take into account for a robust metabolite quantification.

3.3.1 Data acquisition

3.3.1.1 Spatial localisation

Spatial localisation allows the acquisition of spectra from a well-defined region and avoids contamination by non-cerebral tissue, such as extra-cerebral fat. Moreover, B_0 and B_1 inhomogeneities have less impact on signal arising from a limited volume.

Voxel localisation is achieved through application of three slice-selective RF pulses concurrent with linear field gradients in orthogonal directions, thus resulting in the selection of a volume, which corresponds to the intersection of the three slices (Figure 3.6). Each RF pulse excites a particular range of frequencies, which will affect a certain region in the presence of a gradient. Therefore, a proportional relation is formed between the spatial position x and the frequency of the excited spins ω:

$$\omega(x) = \gamma B_0 + \gamma G_X x, \tag{3.8}$$

where γ is the gyromagnetic ratio. The first term is related to the static magnetic field and corresponds to the Larmor frequency, and the second to the spatially varying magnetic field, determined by G_X, the strength of linear field gradient applied in the x axis direction.

Rearranging Eq. 3.8, we retrieve the voxel dimension V_X in the gradient direction:

$$V_X = \frac{BW}{\gamma G_X}, \tag{3.9}$$

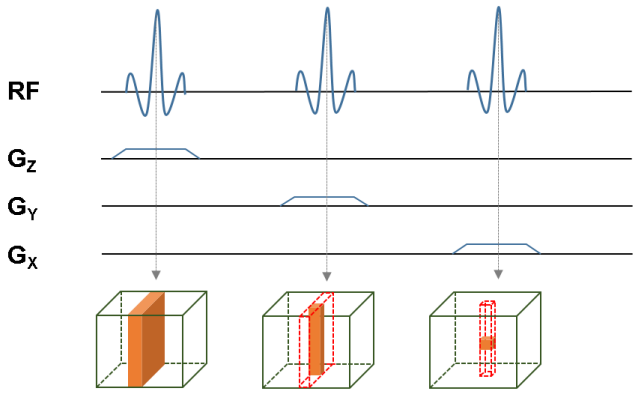


Figure 3.6: Schematic diagram of the procedure for voxel localisation based on the application of RF pulses with linear field gradients ($G_{Z,Y,X}$) in orthogonal directions.

where BW is the RF pulse bandwidth, defined by $\Delta\omega$ (see Figure 3.7 for a graphic description of the volume localisation process).

The bandwidth and excitation profile of an RF pulse depend on its waveform and duration. The longer the RF pulse, the narrower the range of frequencies it can

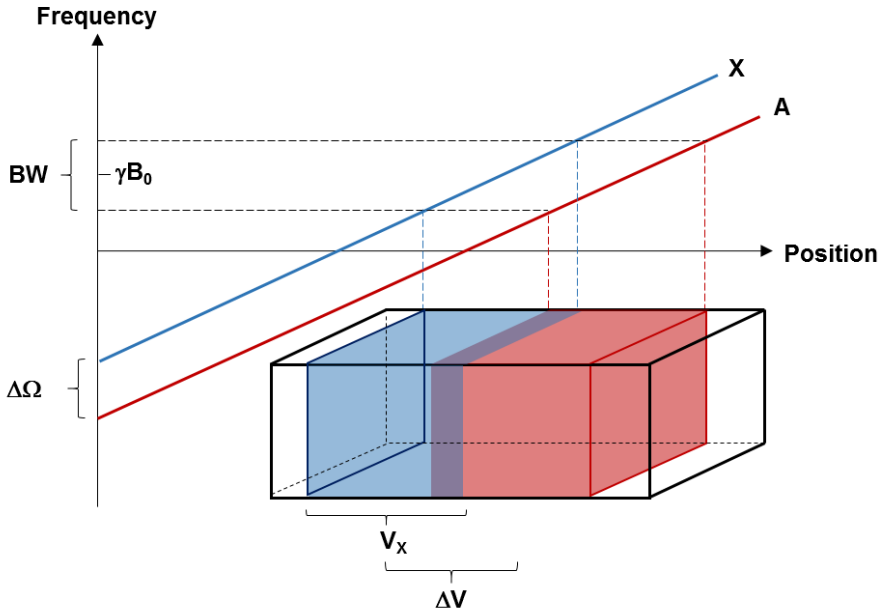


Figure 3.7: Representation of the volume localisation process and the resulting chemical shift displacement artefact due to the limited RF pulse bandwidth (BW). An RF pulse centred at the Larmor frequency (γB_0) and with a certain bandwidth is applied in combination with a linear field gradient on a sample with two chemical groups, A and X, with a frequency separation of $\Delta\Omega$. The voxels, with dimension V, where each of the signals will be acquired from will be spatially displaced by ΔV. The overlapped region corresponds to the fraction of the volume-of-interest common to both chemical groups.

excite. The choice of waveform depends on the desired slice profile. Sinc pulses are the most widely used, as they are associated with an approximately rectangular excitation profile. An infinite sinc pulse should result in a perfect excitation profile (small flip angle approximation). However, reducing the number of sinc lobes will lead to a less ideal profile. Additionally, ringing artefacts start to appear on the edges of the frequency domain profile, which can lead to the excitation of non-desired regions. In Figure 3.8 is shown an example of a pulse waveform in the time domain and its excitation profile in the frequency domain.

Another commonly observed artefact in localised MRS is the chemical shift displacement artefact (CSDA), caused by the finite bandwidth of an RF pulse. The origin and consequences of this artefact will be discussed in the next subsection.

Spatial localisation in direct ^{13}C MRS is a challenge due to the need for an extremely large bandwidth pulse for the localised broadband detection of the entire ^{13}C spectrum. To circumvent this, voxel localisation can be performed indirectly using the ^{1}H channel, thus minimising the bandwidth requirements, as shown in Chapter 6.

Chemical shift displacement artefacts

All spatial localisation techniques suffer from the CSDA, which leads to a shifted volume-of-interest (VOI) for off-resonance nuclei (Figure 3.7). The displacement ΔV_X of the voxel for a given chemical shift difference $\Delta\Omega$, in the direction of a linear field gradient (for example x axis) is given by:

$$\Delta V_X = \frac{\Delta\Omega}{\gamma G_X}. \tag{3.10}$$

Combining Eqs. 3.9 and 3.10, the spatial displacement can be written as:

$$\Delta V_X = \frac{\Delta\Omega}{BW} V_X = kV_X, \tag{3.11}$$

where k is the ratio between the chemical shift difference and the bandwidth of the localisation pulse (in this case both converted to Hz). At stronger magnetic fields, for the CSDA to be minimised, the range of frequencies that are contained in the selected VOI (bandwidth) has to increase with B_0 to counteract the lin-

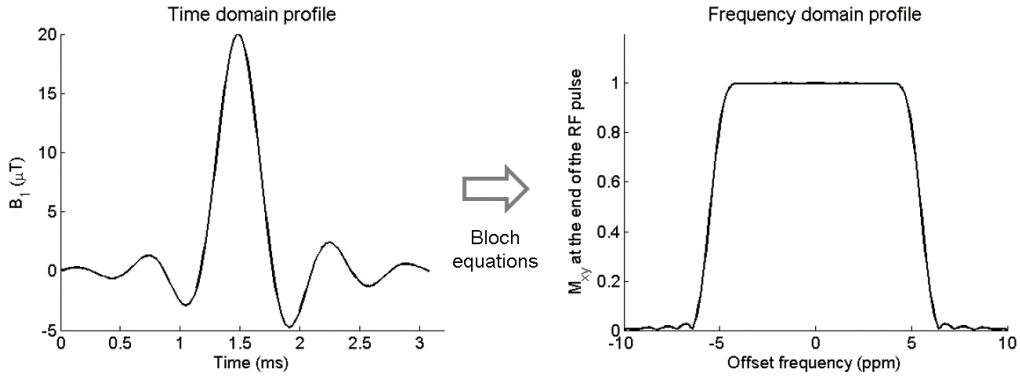


Figure 3.8: Simulation of an RF pulse with finite duration and its slice profile, obtained by solving the Bloch equations. The transition bands are no longer sharp, as compared to an infinite sinc pulse, and ringing artefacts start to appear on the edges of the slice profile.

ear effect of the increasing magnetic field strength on the frequency separation between two resonances due to their chemical environment (chemical shift). To attain that, keeping the same voxel dimensions, the linear field gradient strength would have to increase proportionately. Considering a typical bandwidth for a 90° amplitude-modulated pulse (Figure 3.8) of 3000 Hz and a voxel size of 30 mm, the equivalent gradient strength would be 2.3 mT/m. Comparing this with the maximum gradient strength that the Philips 7 T MR system allows, 40 mT/m, it is possible to conclude that the bandwidth restriction does not originate from the gradient system capabilities, but instead from the RF system.

Rearranging Eq. 2.32, it is possible to express the inverse of the RF pulse duration τ, given by the pulse bandwidth, as a function of the flip angle β and RF field B_1 amplitude:

$$BW = f\frac{B_1\gamma}{\beta}, \tag{3.12}$$

where f is a conversion factor, which depends on the pulse waveform. A linear relationship between the bandwidth of an RF pulse and the amplitude of the RF field B_1 is obtained. However, the amplitude of the RF field that a coil is able to generate decreases with the frequency it is designed to operate at, or equivalently with the static magnetic field strength it is built for. It is known that the RF power required to scan an object with radius r and length l scales with the square

of the resonant frequency [32]:

$$Power = \pi r^4 l \omega^2 \sigma B_1^2, \tag{3.13}$$

where σ is the conductivity of the object. The validity of this expression only holds when the dimensions of the imaged object are small relative to the RF wavelength, which is not the case for ultra high-field human MR. Experimental observations demonstrated that at higher operating frequencies, the power required to obtain a certain B_1 will be more than that predicted for the quasistatic regime [32]. Therefore, for a constant output power from the RF amplifiers to coils used at different magnetic field strengths, their B_1, and hence the bandwidth will decrease to a greater proportion than the relative increase in ω. From the calculations above, we can conclude that at ultra high-field, the voxel displacement, and thus the CSDA is worse as the B_1 requirements cannot be met to counterbalance the larger chemical shift dispersion. Also note from Eq. 3.12 that a larger flip angle will result in a narrower bandwidth. This is because the amplitude of the pulses is set to reach the maximum B_1 and its length is adjusted accordingly. Thus, 180° pulses are associated with larger CSDAs, when compared to 90° pulses for the same frequency difference between two resonances.

The case of the CSDA in scalar-coupled spins is more complex. Let us consider the response of an AX spin system to a PRESS sequence (refer to Figure 3.10 for the diagram of this sequence). Due to this artefact, the voxel for A spins is shifted from the voxel for X spins and, as a result, not all A nuclei within the X voxel will be refocused by both 180° pulses of the sequence. This will lead to an effect termed "anomalous J-modulation", which results in the superposition of signal from different regions with distinct modulation patterns.

Note the schematic diagram in Figure 3.9a. In compartments 1-4, X spins experience both 180° pulses. In compartments 2 and 3, the A spins only experience the first and the second 180° pulses, respectively. In compartment 1, both RF pulses affect A spins, whereas in compartment 4, they are not refocused by any of the pulses.

After the application of an excitation pulse (90°) along the x direction, which rotates the magnetisation to $-y$, the spins are under the effect of chemical shift and

J-coupling evolution over a defined period of time. In this case, the chemical shift evolution is refocused by the two 180° pulses, thus only the J-coupling evolution has to be calculated (see [2] for the description of the product operator formalism). The signal will depend on which refocusing pulses are experienced by the A spins, when observing the X spins. Considering that only in-phase terms at the X spins resonance oriented along the -y axis are detected, the signal arising from each compartment is as follows:

$$\begin{aligned} &\text{Compartment } 1 \Rightarrow S_X = X_y cos\,(\pi JTE) \\ &\text{Compartment } 2 \Rightarrow S_X = X_y cos\,(\pi JTE_1) \\ &\text{Compartment } 3 \Rightarrow S_X = X_y cos\,(\pi JTE_2) \\ &\text{Compartment } 4 \Rightarrow S_X = X_y. \end{aligned} \tag{3.14}$$

The signal modulation in each compartment as a function of TE is depicted in Figure 3.9b, for the case where J was set to the coupling constant of lactate (6.933 Hz), TE_1 was assumed to have a fixed value of 27.2 ms and TE_2 was the remaining time until acquisition, varying with TE.

The signal arising from the entire excited volume is calculated based on the individual volumes of each compartment ($V_{1,2,3,4}$), which depend on the fraction of voxel displacement, expressed by the factor k of Eq. 3.11. Therefore, the partial

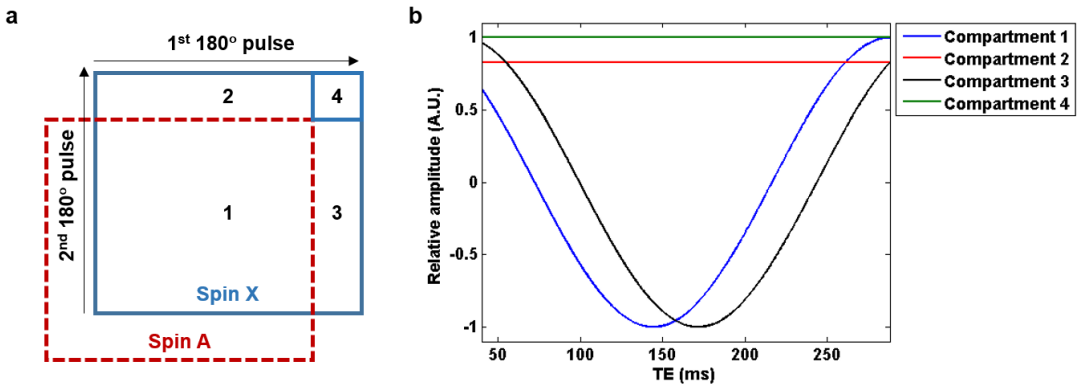


Figure 3.9: Effect of chemical shift displacement artefact on coupled spins during the PRESS sequence. The dotted square in a) represents the spatial shift of A spins relative to X spins (solid line). The 90° pulse is applied in the third direction (not shown here), whereas the first and second 180° pulses are applied in orthogonal directions. The spatial displacement of one spin relative to the other leads to the formation of 4 compartments with different signal modulation patterns shown in b). The signal arising from each compartment as a function of TE was simulated with J set to the coupling constant of lactate and TE_1 = 27.2 ms.

volumes will result from the product of terms combining k or $1-k$ factors, where k applies when only one of the pulses affects the A spins and $1-k$ when both do, as defined in [33, 34]:

$$V_1 = (1-k)^2; V_2 = V_3 = k(1-k); V_4 = k^2. \tag{3.15}$$

The overall signal is determined by the weighted sum of the signals arising from each compartment. Depending on interpulse timings and the severity of the CSDA, the combination of different modulation patterns can lead to the cancellation of the signal [33].

PRESS and STEAM

PRESS and STEAM are localisation techniques capable of achieving 3D localisation in one acquisition. The PRESS sequence (Figure 3.10) is a spin-echo-based technique, in which a slice-selective 90° excitation pulse is combined with two slice-selective 180° refocusing pulses. The echo that contains the signal from the intersection of the three planes, selected by the three gradients, is formed at TE, which equals $TE_1 + TE_2$, where TE_1 is the time between the 90° pulse and the first spin-echo and TE_2 the time between both echoes. The excitation profile of the 90° pulse can be altered due to the dephasing of the magnetisation through

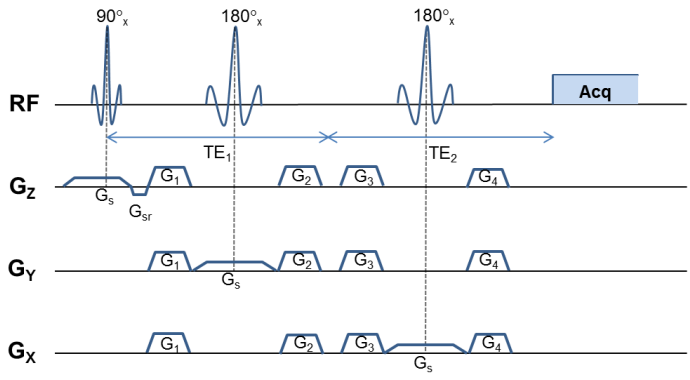


Figure 3.10: Schematic diagram for the PRESS sequence. One excitation and two refocusing pulses are applied to generate a spin-echo at $TE = TE_1 + TE_2$. G_s represent the gradients for slice selection and G_{sr} is the slice refocusing gradient used to compensate the phase dispersion introduced by the first slice selection gradient. G_1 to G_4 are crusher gradients, which spoil unwanted coherences.

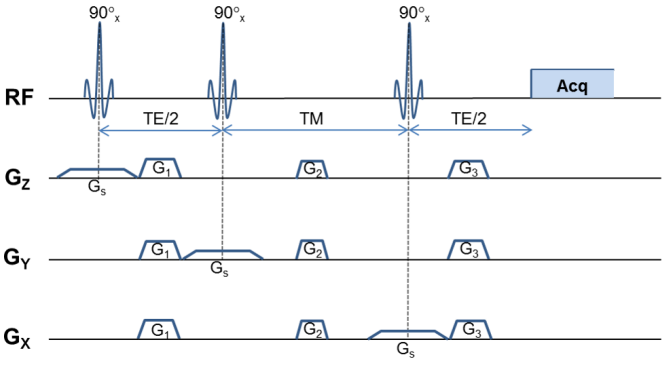


Figure 3.11: Schematic diagram of a standard STEAM sequence. Three 90° pulses are applied in conjunction to generate a stimulated echo. Each of the RF pulses is applied concurrently with slice selection gradients mutually orthogonal to each other (G_s). Dephasing/rephasing gradients G_1 and G_3 are introduced during $TE/2$ intervals, while G_2 gradients, which crush unwanted coherences, are added during the TM interval.

the slice profile. This phase dispersion can be compensated by the use of a refocusing gradient, typically with half the duration of the gradient applied during the RF pulse and opposite polarity. In addition, crusher gradients are introduced in between the RF pulses to dephase unwanted signal arising from outside the VOI. On the other hand, the STEAM sequence (Figure 3.11) consists of three slice-selective RF pulses, each one with a flip angle of 90°. The two first pulses are separated by a delay of $TE/2$ and the mixing time (TM) represents the delay between the second and the third pulses. The stimulated echo is formed at $TE+TM$. In this sequence, the second RF pulse only rotates half the transverse magnetisation to the longitudinal axis, while the other half is dephased by crusher gradients, which results in a reduction of the signal by half when compared to the PRESS sequence.

Despite being associated with a higher SNR, PRESS cannot be performed with a very short TE, as the duration of 180° pulses is longer than that of 90° pulses. This might constitute a problem in the detection of metabolites with very short T_2 relaxation times, whose signal decays more rapidly, and also for additional correction of different T_2 decays of the metabolites of interest. Additionally, the PRESS sequence leads to larger CSDAs, because of the use of 180° pulses, as discussed in the previous subsection. The effect of the CSDA on the STEAM sequence at ultra high-field will be discussed in Chapter 4.

sLASER

sLASER is a single-shot 3D localisation technique, consisting of an excitation and a series of adiabatic refocusing pulses, making this sequence less susceptible to RF inhomogeneities, while reducing the CDSA with the use of high bandwidth pulses. A diagram of a basic sLASER sequence is depicted in Figure 3.12. The selective refocusing is achieved by the use of two pairs of adiabatic full passage (AFP) pulses. The presence of a second AFP pulse aims to refocus the nonlinear B_1 and position dependent phase across the slice, generated by the first pulse of the pair. A spin-echo is then generated at TE $= 2(\tau_2 + \tau_4)$, in which τ_2 and τ_4 are the delays between the pulses of the first and second pair of AFP pulses, respectively.

At ultra high-field, sLASER is preferred over the PRESS sequence due to the better spatial selection properties of AFP pulses. In contrast to the STEAM sequence, short TE acquisitions are not available, with TEs under 20 ms not being typically achievable [35]. However, sLASER constitutes an attractive option for the detection of certain coupled metabolites, whose J-coupling constants lead to optimal TEs longer than the minimum sLASER TE. This sequence was employed for the detection of the weakly-coupled spin system lactate, described in Chapter 5.

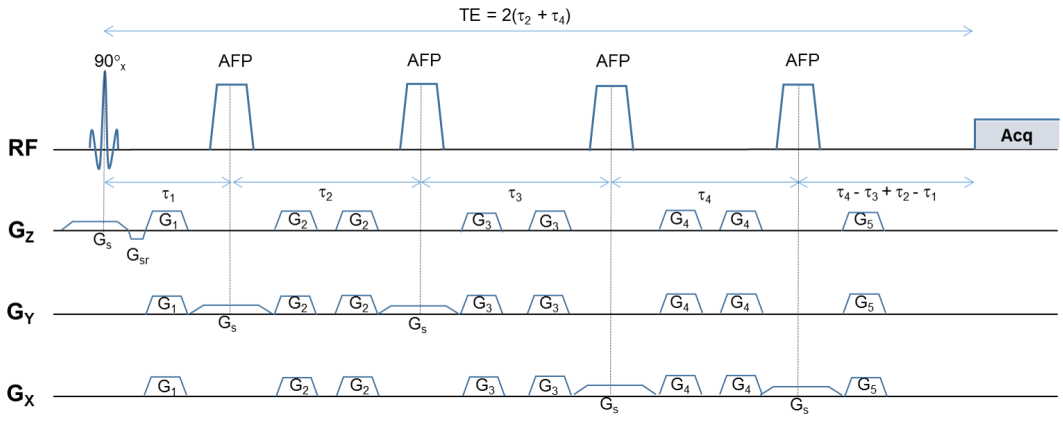


Figure 3.12: Schematic diagram for the sLASER sequence. The sLASER sequence is based on the PRESS sequence, except the 180° pulses are substituted by a pair of adiabatic full passage (AFP) pulses. Each pulse of the pair is applied with the slice selection gradients G_s, with the first G_s being followed by the slice refocusing gradient G_{sr}. Crusher gradients $G_{1,2,3,4,5}$ are introduced in between the pulses.

ISIS

ISIS uses multiple-acquisitions combined with an add/subtract scheme for the localisation of a VOI. Figure 3.13a shows a schematic diagram with a description of the acquisition steps involved in this sequence. In each acquisition, a set of slice-selective inversion pulses applied concurrently with orthogonal field gradients prepares the longitudinal magnetisation, which is then rotated to the transverse plane by a 90° pulse. The inversion pulses are turned on or off following a specific scheme and the number of required acquisitions is determined by the number of desired spatial encoding directions. The addition/subtraction of the individual scans will result in the nulling of the signal outside the region of interest, while accumulating the signal in the desired location. 1D and 2D ISIS are performed with the first two and four acquisitions, respectively. In Figure 3.13b is depicted an example of the selection of a region of interest using 2D ISIS. When zero or an

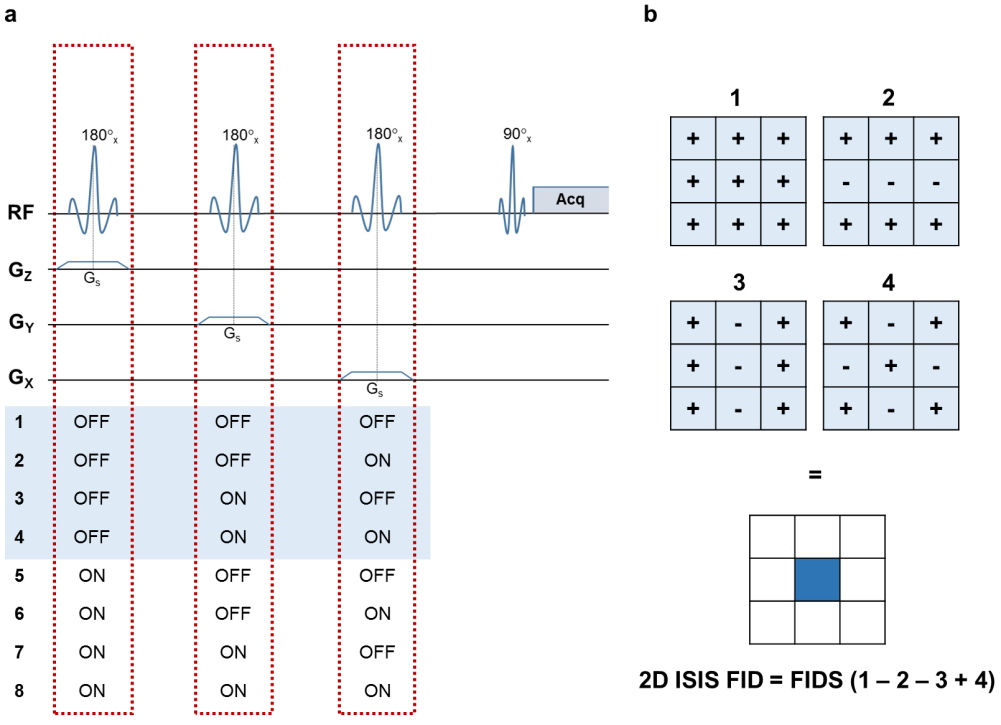


Figure 3.13: Schematic diagram for the ISIS sequence. a) Different acquisitions are run with the presence or the absence of the 180° pulses applied in conjunction with slice selection gradients (G_s). The number of acquisitions depends on the number of spatial encoding directions. The magnetisation is then rotated to the transverse plane with a 90° pulse. b) Example of the 2D ISIS scheme. Four acquisitions are necessary to localise the area in dark blue, which are followed by the application of the appropriate add/subtract scheme.

even number of pulses are applied, the final magnetisation in the selected cross-section is positive, whereas an odd number of pulses results in a magnetisation with negative sign. The combination of the resulting FIDs acquired according to the scheme shown in the figure localises the area in dark blue. To extend to a complete 3D localisation, eight consecutive individual acquisitions (Figure 3.13a) are required to select a VOI with the following adding/subtraction scheme:

$$\begin{aligned} \text{3D ISIS } FID = FID_1 - FID_2 - FID_3 - FID_4 \\ + FID_5 + FID_6 + FID_7 - FID_8. \end{aligned} \tag{3.16}$$

ISIS is rarely used in ^{1}H MRS since the localisation accuracy can be compromised by a number of factors. For detection of metabolites with long T_1, whose T_1 relaxation is incomplete within the sequence repetition time (TR), an effect termed T_1 smearing arises, leading to the incomplete cancellation of unwanted signals. Additionally, when the VOI is small relative to the whole excited volume, subtraction errors can lead to large contamination artefacts, making this sequence particularly sensitive to physiological and patient motion. On the other hand, ISIS is suitable for the detection of metabolites with short T_2 relaxation times, as the short delay between excitation and the start of acquisition minimises signal loss. This sequence was used for the ^{1}H signal localisation in the ^{13}C MRS experiments described in Chapter 6.

3.3.1.2 Water suppression

The water peak is a dominating resonance in the ^{1}H spectrum arising at 4.7 ppm, due to the abundance of water in all tissues. As the concentration of metabolites is about four orders of magnitude lower than the water concentration, suppression of this peak is required to make the molecules of interest visible in the spectrum. Most commonly employed water suppression techniques are based on the chemical shift selective (CHESS) method [36], which employs a narrow band RF pulse centred on the water frequency to transpose this resonance onto the transverse plane, followed by crusher gradients to dephase the signal. This module precedes the acquisition of the metabolite spectrum and the delay between them should be as short as possible to avoid water signal recovery by T_1 relaxation.

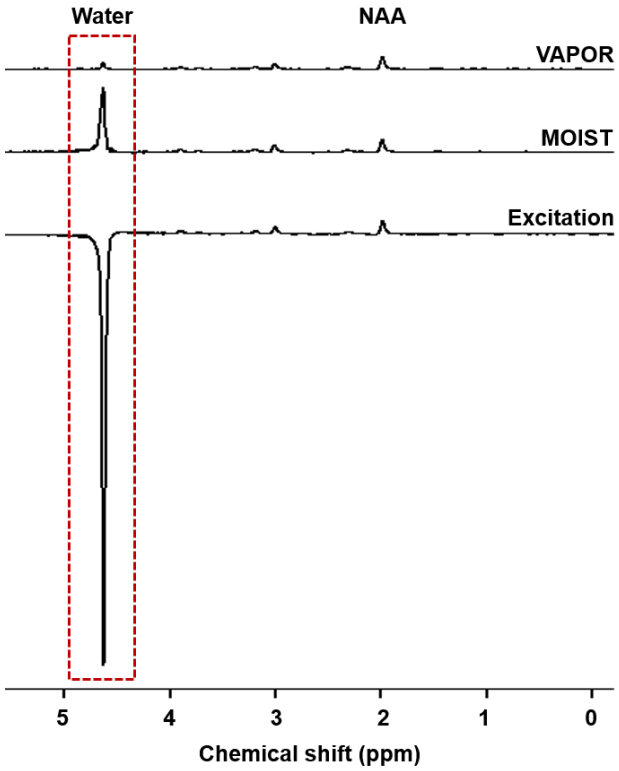


Figure 3.14: ^{1}H spectra acquired with different water suppression techniques: VAPOR, MOIST and excitation. The spectra were acquired with the sLASER sequence (TR/TE = 5000/144 ms, 64 averages) from a 15x30x20 mm^3 voxel placed in a volunteer's occipital cortex.

In Figure 3.14, ^{1}H brain spectra acquired with three distinct water suppression methods are shown. The excitation method is the simpler of the three and uses only two excitation pulses, therefore proving to be the least effective method. On the other hand, techniques as multiply optimised insensitive suppression train (MOIST) [37, 38] and variable pulse powers and optimised relaxation delays (VAPOR) [39] employ a train of pulses, being more robust to flip angle variations. Due to its efficient water signal suppression (Figure 3.14), VAPOR was the preferred method in the studies of this thesis and was used whenever available and compatible with the subsequent MRS sequence.

An effective water suppression minimises baseline distortions and spurious signals due to vibration-induced signal modulation, which leads to a more reliable quantification. Water signal suppression is not necessary in direct ^{13}C MRS, due to the absence of ^{1}H signal.

3.3.1.3 Techniques to reduce outer volume contamination

An RF pulse with imperfect excitation or inversion profile can at times lead to the excitation of regions outside the VOI. This can be the case in brain MRS, in which the spectra might be contaminated by extra-cerebral fat, especially when the VOI is placed near the scalp. To suppress these signals, an outer volume suppression (OVS) module, preceding the metabolite spectrum acquisition, can be added. The principle of OVS is based on the application of a slice-selective pulse and crusher gradients to suppress the signal within bands. On the Philips 7T MR system, these bands are termed regional suppression technique (REST) slabs [40] and their power, thickness, central frequency (water or fat) and position can be adjusted.

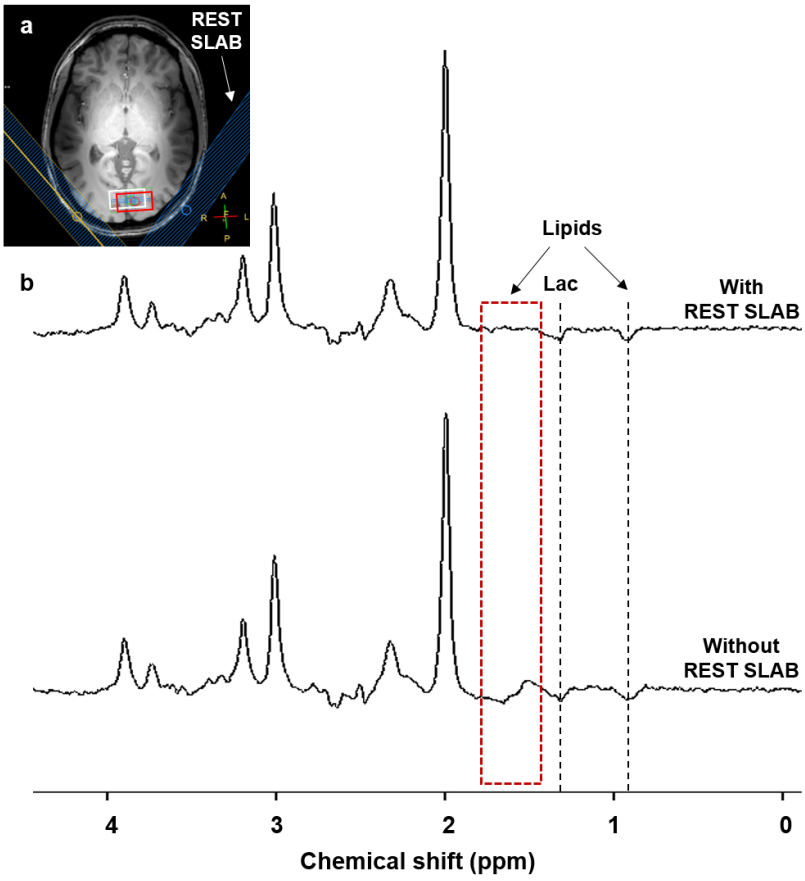


Figure 3.15: ^{1}H spectra (b) acquired with the sLASER sequence (TR/TE = 5000/144 ms, 64 averages) from a 15x30x20 mm^3 voxel placed in a volunteer's occipital cortex, with and without regional suppression technique (REST) slabs (two slabs, power = 4, thickness = 30 mm, centred on fat). Voxel and REST slabs position on the anatomical image shown in a). Lac refers to lactate.

In Figure 3.15, an example of the application of this technique for suppression of the lipid signal is shown. ^{1}H spectra were acquired with the sLASER sequence from a voxel located in the occipital region. Note that when the spectrum is acquired with REST slabs, the contamination in the spectral region of 1.8 to 1.45 ppm vanishes, while the amplitude of the negative lipid peak at 0.9 ppm is reduced, in comparison with the spectrum obtained without REST slabs. This shows that these signals originated largely from outside the VOI.

A spectrum free of lipid contamination is particularly important for lactate quantification. For example, the artefact from 1.8 to 1.45 ppm causes baseline distortion near the lactate peak, which can lead to unreliable spectral quantification. Another strategy that can be used to minimise outer volume contamination is to change the chemical shift direction by inverting the linear field gradient direction. For example, the lactate VOI represented by the white box in Figure 3.15a was chosen to be shifted to the anterior direction. Thus, resonances with lower chemical shift than the water peak are acquired from a volume further away from the scalp.

3.3.1.4 Techniques to improve B_1 and B_0 homogeneity

The effect of the static and RF field inhomogeneities can directly be observed in the spectrum and the application of techniques to attenuate them is crucial to guarantee a good spectral quality in MRS.

In a perfectly homogeneous static magnetic field, all the Lorentzian lines acquired within a volume are centred at the same frequency. They will add coherently generating a single Lorentzian line with a linewidth solely dependent on the T_2 relaxation properties of the object. However, in the presence of B_0 field inhomogeneities, each Lorentzian line will have a distinct frequency that when added together will give rise to a broadened line. This distribution of frequencies can also lead to a loss of phase coherence, resulting in a faster decay of the transverse magnetisation, now dictated by T_2^*, and thus broadening the peak (see section 3.1).

B_0 inhomogeneities can arise from the hardware or be intrinsic to the sample. With regards to the first, these inhomogeneities can be corrected with the addi-

tion of shim coils when the magnet is built. Inhomogeneities caused by the sample are object-specific and depend on several factors, such as the geometry and susceptibility interfaces between different materials, which yield field perturbations. The field perturbations caused by the susceptibility effect are exacerbated with increasing magnetic field strength. This type of B_0 inhomogeneity can be corrected by a method termed shimming.

Preceding the acquisition of MR spectra, an appropriate sequence is run to provide a measure of these field inhomogeneities (B_0 mapping). Shimming methods are subsequently applied to minimise the perturbations, which generally involve decomposing the field inhomogeneities into a linear combination of spherical harmonics. These are then generated by shim coils to correct the magnetic field for the perturbations. In spectroscopy, the smaller the volume to be shimmed, the more efficient the correction of the field perturbations is.

The shimming technique used for all of the MRS acquisitions described in this thesis is termed pencil-beam volume shimming, a Philips routine based on the fast, automatic shimming technique by mapping along projections (FASTMAP) [41].

On the other hand, the major cause for B_1 inhomogeneities at ultra high-field is the shorter RF wavelength, further shortened by the dielectric properties of the tissue. As the magnetic field strength increases, the wavelength becomes the same size or smaller than the imaged anatomic regions, which gives rise to standing waves that constructively or destructively interfere. Severe B_1 inhomogeneity leads to substantial variations in the flip angle and receive sensitivity (principle of reciprocity) across the VOI, which result in variable SNR in images (dark and bright areas) and low SNR in spectra with improper signal modulation.

Similarly, B_1 shimming can be performed using multiple transmit coils [42]. B_1 homogeneity can be achieved by manipulating the magnitude and phase of each transmitter channel until an uniform excitation is obtained over a target region (active B_1 shimming). A more readily available option involves the use of dielectric pads [43] (passive B_1 shimming). Dielectric pads are composed of high-permittivity materials and are able to alter the spatial distribution of the electromagnetic fields, shifting the B_1 constructive interference pattern to regions with

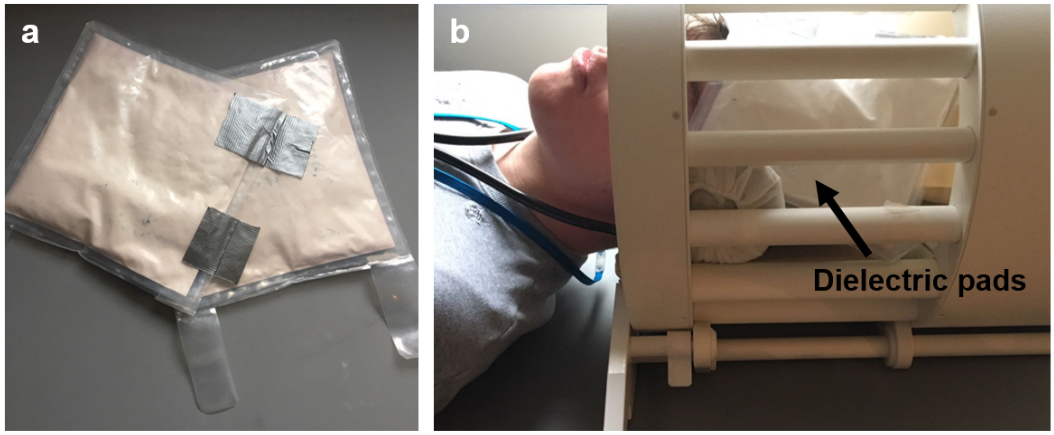


Figure 3.16: Calcium titanate dielectric pads (a), placed on top of a volunteer's head inside a $^{13}C/^{1}H$ volume coil (b).

low sensitivity due to the geometry of the sample. Dielectric pads with calcium titanate were used in the experiment described in Chapter 6 (see Figure 3.16). Note the increase in relative flip angle values observed in the B_1 transmit field maps with the presence of dielectric pads (Figure 3.17).

Finally, in order to obtain the correct flip angle, careful pre-scan calibration sequences should be run to adjust the RF voltage appropriately for each experiment.

3.3.1.5 Sensitivity

In the previous chapter, it was shown that the equilibrium magnetisation M_0 increases with $\gamma^2 B_0$. The signal measured by the receiver coils is proportional to

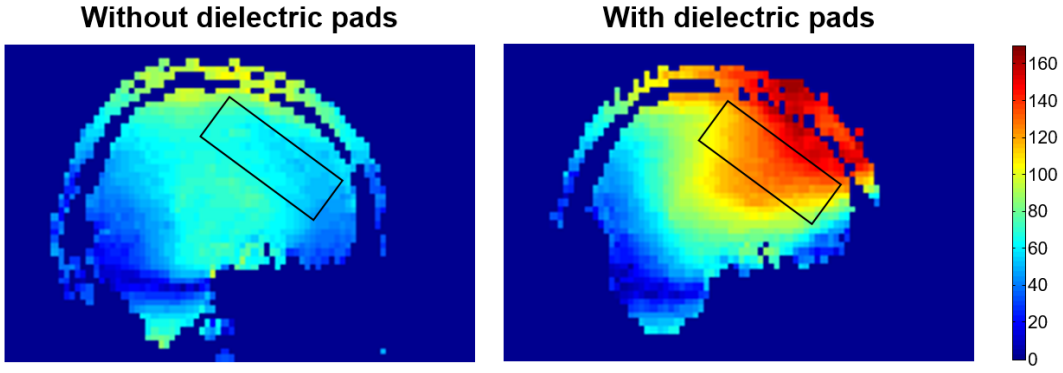


Figure 3.17: B_1 transmit field maps obtained with and without calcium titanate dielectric pads positioned on top of the frontal region of a volunteer's scalp. The black boxes show the VOI in a ^{13}C experiment. Colourbar represents percentage change in flip angle values.

$\omega_0 M_0$, or equivalently, $\gamma^3 B_0^2$. However, in high-field human MR the noise contribution from conducting samples also increases linearly with the frequency, which makes the sensitivity, defined in this case as SNR, proportional to $\gamma^2 B_0$ [1]. This expression provides the mathematical derivation of the observed linear increase in SNR with increasing magnetic field strength. It also allows the comparison between the relative sensitivities of ^{1}H and ^{13}C experiments. As the gyromagnetic ratio of ^{13}C is four times smaller than the one of ^{1}H, the overall SNR of a ^{13}C scan (considering a 100% ^{13}C-labelled molecule and a single nucleus detection) is 1/16 times less than a ^{1}H scan. In this case, polarisation transfer techniques can be used to enhance the sensitivity in multinuclear MRS, by transferring the polarisation of the ^{1}H to the ^{13}C nuclei. Under optimal conditions, the initial magnetisation of ^{13}C can be increased by a factor of four (γ_H/γ_C). The distortionless enhancement by polarisation transfer (DEPT) sequence [44] is one of the available polarisation transfer techniques and has been used in the ^{13}C MRS experiment described in Chapter 6.

The sensitivity of an experiment is also proportional to square root of the total acquisition time divided by TR. Hence, longer experiments combined with a shorter TR provide an increased SNR. However, it is important to consider that the choice of TR should also take into account the T_1 relaxation times of the sample, as a short TR can result in an incomplete longitudinal magnetisation recovery. One way to circumvent this temporal dependence is to express the sensitivity as a function of the square root of the number of acquisitions. From this, it is clear that averaging more spectra together will result in a higher SNR.

Finally, in single voxel MRS, the sensitivity is also scaled with the voxel dimensions. Thus, larger voxels will be associated with increased SNR, but the specificity of the measurement (tissue type/location) decreases.

3.3.2 Data post-processing

3.3.2.1 Truncation

Signal and noise are simultaneously recorded during the acquisition of an FID. Noise reduction can be performed after signal detection in order to improve spec-

tral quality.

The FID signal is maximum at the beginning of the acquisition and decays over time, until only noise is measurable. The acquisition time can be artificially truncated by removing the last set of points of an FID corresponding to noise, thus increasing the sensitivity (Figure 3.18). However, severe truncation at the post-processing level, similarly to a shorter acquisition time, can lead to the emergence of ringing artefacts.

3.3.2.2 Apodisation

Apodisation is another post-processing method used to increase the sensitivity of the spectrum and consists of multiplying the FID by a filter function, which leaves the early part of the FID unaffected and attenuates the later parts. A common choice for a filter function is an exponential with an adjustable decay rate. However, the use of a filter function will not only attenuate noise, but will also broaden the linewidth of the peaks in the spectrum. This effect is shown by combining Eq. 3.2 with the one of an exponential decaying filter:

$$S(t) = M_0 \sin(\theta) \exp(i\Omega t) \exp\left(-\frac{t}{T_2^*}\right) \exp\left(-\frac{t}{R_{LB}}\right), \tag{3.17}$$

from which we conclude that the final linewidth of the spectrum will be a result of the sum of its original linewidth with the artificial line broadening. As discussed previously, line broadening will cause a reduction in the peak height, thus compromising SNR (Figure 3.18). An optimal SNR is achieved by choosing a decay rate that matches the original peak linewidth [1].

3.3.2.3 Zero filling

As mentioned in subsection 3.1, the FID is composed of a certain number of data points which will remain the same after the Fourier Transform. Increasing the number of sampled points will result in a better spectral resolution, but also in the increase of the acquisition time and thus in the noise contribution. A common solution is to add a determined number of zeros to the FID, at the post-processing level. Zero filling will not add new information, but rather improves the spectral

appearance by interpolation of the data points (Figure 3.18).

3.3.2.4 Phase and frequency correction

As shown in Eq. 3.5, it is common for a shift in the phase of the signal at the reception stage to occur, which can arise from a miscalibration of the phase detectors. In this case, the real part of the Fourier transform of the signal would not correspond to the purely absorptive signal, but rather contain a mixture of the absorption and dispersion modes. In order to recover the purely absorption mode, phase correction can be applied to the FID simply by including a phase correction term, as described in the following expression, for a single magnetisation at frequency Ω:

$$S(t)_{corrected} = M_0 \sin(\theta) \exp(i\Omega t) \exp\left[i(\phi + \phi_{corr})\right] \exp\left(-\frac{t}{T_2^*}\right), \tag{3.18}$$

where ϕ_{corr} would be chosen to be $-\phi$, thus removing the phase offset term. If the correction is applied in the frequency domain, $S(\omega)_{corrected}$ will be:

$$\begin{aligned} Re[S(\omega)]_{corrected} &= Re[S(\omega)]cos(\phi_{corr}) + Im[S(\omega)]sin(\phi_{corr}) \\ Im[S(\omega)]_{corrected} &= Im[S(\omega)]cos(\phi_{corr}) - Re[S(\omega)]sin(\phi_{corr}), \end{aligned} \tag{3.19}$$

where the phase corrected signal is composed of a combination of the phase corrected real and imaginary components. Here, the phase shift is the same for all frequency offsets ω, such that the phase correction is independent of the frequency and is called zero-order phase correction (Figure 3.18). On the other hand, a pre-sampling delay, a gap between the RF pulse and the start of the acquisition of the FID may also introduce a phase shift in the data, so that the maximum of the FID does not correspond to $t = 0$. This phase shift will vary linearly with the frequency, and requires a first-order phase correction:

$$\phi_{corr}(\omega) = \phi_{zero-order} + \phi_{first-order} \times \frac{\omega}{SW}. \tag{3.20}$$

Another option is to use the power spectrum, which is not phase-dependent. However, the resulting peaks are broader, therefore compromising the spectral

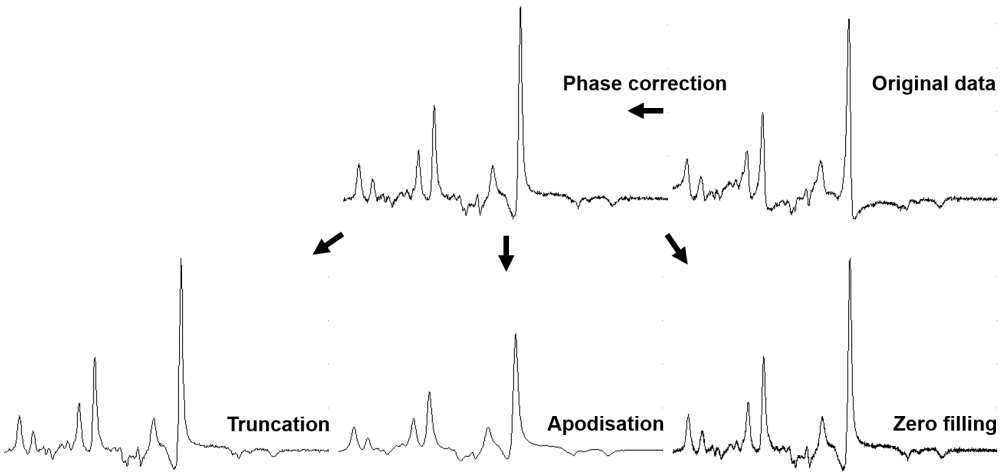


Figure 3.18: Example of post-processing techniques applied to the FID (before Fourier Transform) - truncation, apodisation and zero filling - and to the spectrum - phase correction. The original FID with 4096 data points was truncated to 2048 points, apodised with a 8 Hz exponential filter and zero filled with 4096 points. The phase of the spectrum was corrected by 45°.

resolution.

Occasionally, it might also be necessary to correct for small B_0 drifts in the spectrum. These shifts can be caused by magnetic fluctuations, in particular the fluctuations of the shim coils with temperature over time. The fluctuations of the sample temperature can also be a source of frequency shift. The position of the water peak, used for frequency reference in ^{1}H MRS, is also dependent on the local pH. When spectra are added or subtracted, it is convenient to correct these frequency drifts by alignment of a reference peak (e.g.creatine) [45], in order to avoid the emergence of additional/residual peaks.

In ^{13}C MRS, where no internal reference is available pre-infusion, calibrations for frequency adjustment might be insufficient and generate a frequency offset in the measured spectrum.

3.3.3 Spectral quantification

The final step in the MRS pipeline involves the estimation of the metabolite concentration levels based on the relative resonance areas, which are proportional to the amount of spins in the sample. The area under the peak can be calculated in the FID (signal amplitude in the time domain) or in the spectrum (signal integra-

tion in the frequency domain).

Several packages are available for automatic fitting of spectra using prior knowledge information, which allows biophysically relevant information to be included in the spectral fitting procedure. Two packages are used in the experiments described in this thesis: LCModel [46] and advanced method for accurate, robust, and efficient spectral fitting (AMARES) [47] from the jMRUI software [48].

LCModel is based on the fact that the total NMR signal can be decomposed into a linear combination of signals from isolated compounds. Therefore, this program uses linear combination (LC) modelling algorithms to estimate metabolite concentrations. This type of algorithm relies on the creation of an accurate metabolite basis set, which contains all the individual resonances which are expected to be present in the spectrum. The basis set can be obtained experimentally or it can be simulated. The advantage of the *in vitro* approach is that the acquisition parameters will be very similar between both *in vitro* and *in vivo* measurements. However, it can be an intensive and costly task to obtain several individual spectra, especially when it has to be repeated for each MR sequence. Alternatively, the metabolite spectra can be simulated through the use of density matrix calculations. Despite rapidly providing a complete basis set, a clear disadvantage of this method is that the simulations are noiseless and artefact-free, thus not giving an accurate description of the experiment. Various programs are available for simulation of MR spectra such as Versatile Simulation, Pulses, and Analysis (VESPA) [49], which is used in the data analysis pipeline described in Chapter 5. In essence, LC modelling algorithms adjust the amplitudes, frequencies, linewidths and phases of the metabolite basis set to match the *in vivo* spectrum. The user can also impose soft constraints on the fitting parameters in order to achieve a more meaningful spectral fitting. Some of the most crucial parameters for an accurate metabolite quantification are involved in the determination of the macromolecular (MM) profile. At short TE, the spectra are characterised by a significant oscillating background arising from high molecular weight compounds (macromolecules). In LCModel, the MM profile is simulated for some typical MM resonances. However, artefacts, metabolites which might not be included in the basis set or even changes in the metabolite levels can be erroneously modelled as part of the MM profile,

thus resulting in a biased quantification. In this case, a more robust method is to measure the MM profile and include it in the basis set. Details on how to handle the MM profile depending on the specific features of the spectrum are discussed in Chapter 5. In Figure 3.19 is shown an example of spectral fitting performed with LCModel, with the fitted data and its decomposition into some individual metabolite signals depicted.

In this thesis, the non-linear-least-squares algorithm AMARES from jMRUI was used for the quantification of ^{13}C MRS data (Chapter 6). The user can add some prior knowledge, regarding amplitudes, frequencies, phases, linewidth, and shape of the peaks, which can improve the precision of the quantification. The analysis of the spectra is performed in the time domain, in contrast to LCModel, which uses the frequency domain.

Quantitative results should always be given with error estimates. The stochastic uncertainty for a single measurement is reflected in the Cramér–Rao lower bound (CRLB). They represent the variance of the estimated parameters, with respect to a certain model, a set of parameters, and a noise level. Given that the CRLBs include the effects of SNR and that they are calculated under the assumption the

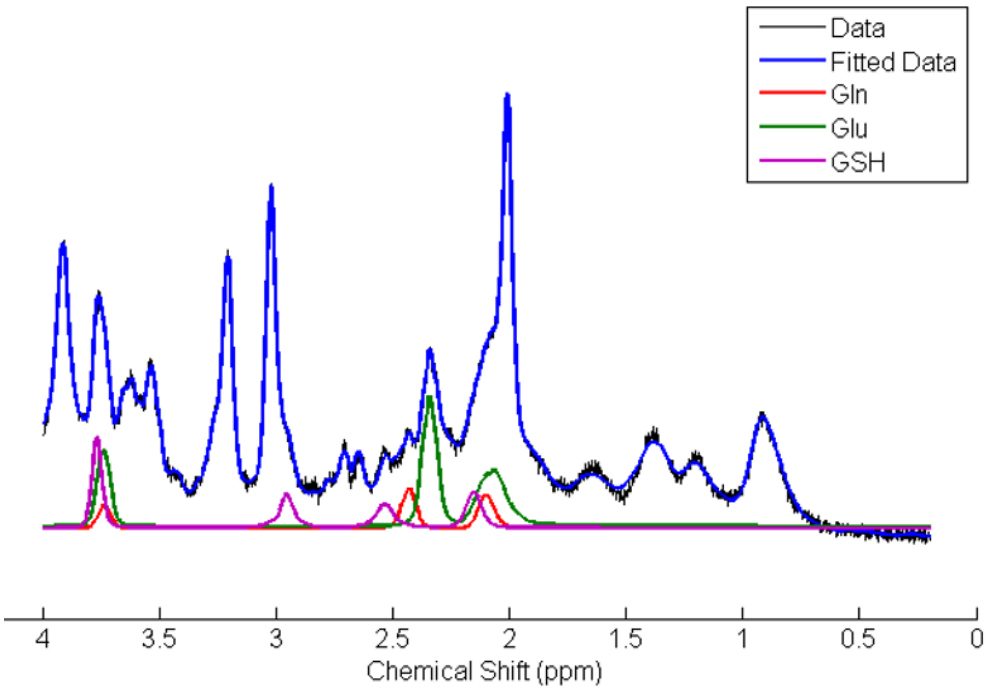


Figure 3.19: Example of spectral fitting performed with LCModel. The fitted data and the corresponding fits for glutamine (Gln), glutamate (Glu) and glutathione (GSH) are shown. The ^{1}H MRS spectrum was acquired from the anterior cingulate cortex of a healthy volunteer with a short TE STEAM sequence at 7 T.

fitting model is correct, systematic errors can be neglected, leading to an under- or over-estimation of the confidence limits. Typically, metabolite levels determined with CRLBs below 20% are considered sufficiently reliable [50].

The next step in the spectral quantification pipeline is to convert the relative resonance areas to absolute concentrations, expressed in molar ($molL^{-1}$) or molal ($molg^{-1}$) concentration. The reference for absolute quantification can be provided with an internal compound naturally occurring in the tissue or with a reference signal from an external source. Only internal referencing will be discussed here. For ^{1}H MRS, water, total creatine and NAA have been proposed as internal concentration references. However, care must be taken when referencing to metabolites, whose concentration might change with disease progression. For example, a substantial decrease in NAA levels is observed in a wide range of pathologies (see subsection 3.2.1). Water [51] and total creatine [52] are relatively stable molecules. Nevertheless, both molecular concentrations are known to vary with the tissue type (gray matter, white matter and cerebrospinal fluid). To correct for partial volume effects, i.e., mixture of different tissue types within the MRS voxel, a method described by Gasparovic et al. [53] can be applied, which also takes into account the differences in relaxation times between distinct metabolites. The water signal, acquired from an unsuppressed water scan, is also used to correct distorted metabolite lineshapes caused by eddy currents [54].

Finally, visual inspection is advisable before and after metabolite quantification, independently of the metabolite concentrations given by the fitting packages. Before quantification, inspection for potential artefacts, poor water suppression, lipid contamination and baseline distortions is recommended. SNR is often used to discard unsatisfactory spectra. However, since SNR is directly linked to the calculation of CRLBs, a rejection criterion based on the CRLB of each metabolite seems more reasonable [55]. Rejection based on the overall spectral linewidth has also been proved to be very useful [56]. After quantification, visualisation of the fitted spectrum, as well as of the residuals are used to verify the accuracy of the analysis.

Bibliography

[1] Robin A De Graaf. *In vivo NMR spectroscopy: principles and techniques*. John Wiley & Sons, 2013.

[2] Malcolm H Levitt. *Spin dynamics: basics of nuclear magnetic resonance*. John Wiley & Sons, 2001.

[3] David S Wishart, Colin G Bigam, Jian Yao, Frits Abildgaard, H Jane Dyson, Eric Oldfield, John L Markley, and Brian D Sykes. ^{1}H, ^{13}C and ^{15}N chemical shift referencing in biomolecular NMR. *Journal of biomolecular NMR*, 6(2):135–140, 1995.

[4] Prabhat KK Pandey and P Chandra. Calculation of nuclear spin-spin coupling constants by SCF perturbation theory with MINDO/3 approximation. *Theoretica chimica acta*, 50(3):211–221, 1978.

[5] Malcolm H Levitt and Ray Freeman. Composite pulse decoupling. *Journal of Magnetic Resonance (1969)*, 43(3):502–507, 1981.

[6] Varanavasi Govindaraju, Karl Young, and Andrew A Maudsley. Proton NMR chemical shifts and coupling constants for brain metabolites. *NMR in Biomedicine*, 13(3):129–153, 2000.

[7] Ralf Mekle, Vladimír Mlynárik, Giulio Gambarota, Martin Hergt, Gunnar Krueger, and Rolf Gruetter. MR spectroscopy of the human brain with enhanced signal intensity at ultrashort echo times on a clinical platform at 3T and 7T. *Magnetic Resonance in Medicine*, 61(6):1279–1285, 2009.

[8] Gregor Hasler, Jan Willem van der Veen, Toni Tumonis, Noah Meyers, Jun Shen, and Wayne C Drevets. Reduced prefrontal glutamate/glutamine and γ-aminobutyric acid levels in major depression determined using proton magnetic resonance spectroscopy. *Archives of general psychiatry*, 64(2):193–200, 2007.

[9] Katharine N Thakkar, Lara Rösler, Jannie P Wijnen, Vincent O Boer, Dennis WJ Klomp, Wiepke Cahn, René S Kahn, and Sebastiaan FW Neggers. 7T proton magnetic resonance spectroscopy of gamma-aminobutyric acid, glutamate, and glutamine reveals altered concentrations in patients with schizophrenia and healthy siblings. *Biological psychiatry*, 81(6):525–535, 2017.

[10] Edward J Novotny, Fahmeed Hyder, Michael Shevell, and Douglas L Rothman. Gaba changes with vigabatrin in the developing human brain. *Epilepsia*, 40(4):462–466, 1999.

[11] Edward J Novotny, Robert K Fulbright, Phillip L Pearl, K Michael Gibson, and Douglas L Rothman. Magnetic resonance spectroscopy of neurotransmitters in human brain. *Annals of neurology*, 54(S6):S25–S31, 2003.

[12] WR Wayne Martin. MR spectroscopy in neurodegenerative disease. *Molecular Imaging and Biology*, 9(4):196–203, 2007.

[13] FA Howe, SJ Barton, SA Cudlip, M Stubbs, DE Saunders, M Murphy, P Wilkins, KS Opstad, VL Doyle, MA McLean, et al. Metabolic profiles of human brain tumors using quantitative in vivo ^{1}H magnetic resonance spectroscopy. *Magnetic Resonance in Medicine*, 49(2):223–232, 2003.

[14] PS Murphy, IJ Rowland, L Viviers, M Brada, MO Leach, and ASK Dzik-Jurasz. Could assessment of glioma methylene lipid resonance by in vivo ^{1}H-MRS be of clinical value? *The British journal of radiology*, 2014.

[15] J Donacha Hanrahan, I Jane Cox, A David Edwards, Francis M Cowan, Janet Sargentoni, Jimmy D Bell, David J Bryant, Mary A Rutherford, and Dennis Azzopardi. Persistent increases in cerebral lactate concentration after birth asphyxia. *Pediatric research*, 44(3):304–311, 1998.

[16] SJ Austin, A Connelly, DG Gadian, JS Benton, and EM Brett. Localized ^{1}H NMR spectroscopy in Canavan's disease: a report of two cases. *Magnetic resonance in medicine*, 19(2):439–445, 1991.

[17] Sylvia Stöckler, Folker Hanefeld, and Jens Frahm. Creatine replacement therapy in guanidineoacetate methyltransferase deficiency, a novel inborn error of metabolism. *The Lancet*, 348(9030):789–790, 1996.

[18] Jiddeke M van de Kamp, Petra JW Pouwels, Femke K Aarsen, W Leontine, Dirk L Knol, Johannes B de Klerk, F Ireneus, Jan GM Huijmans, Cornelis Jakobs, Marjo S van der Knaap, et al. Long-term follow-up and treatment in nine boys with X-linked creatine transporter defect. *Journal of inherited metabolic disease*, 35(1):141–149, 2012.

[19] A Bizzi, G Castelli, M Bugiani, PB Barker, EH Herskovits, U Danesi, A Erbetta, I Moroni, L Farina, and G Uziel. Classification of childhood white matter disorders using proton MR spectroscopic imaging. *American Journal of Neuroradiology*, 29(7):1270–1275, 2008.

[20] A Sturrock, C Laule, J Decolongon, R Dar Santos, AJ Coleman, S Creighton, N Bechtel, R Reilmann, MR Hayden, SJ Tabrizi, et al. Magnetic resonance spectroscopy biomarkers in premanifest and early Huntington disease. *Neurology*, 75(19):1702–1710, 2010.

[21] Jullie W Pan, Anne Williamson, Idil Cavus, Hoby P Hetherington, Hitten Zaveri, Ognen AC Petroff, and Dennis D Spencer. Neurometabolism in human epilepsy. *Epilepsia*, 49(s3):31–41, 2008.

[22] Dawn E Saunders. MR spectroscopy in stroke. *British medical bulletin*, 56(2):334–345, 2000.

[23] Paul A Bottomley. Spatial localization in NMR spectroscopy in vivo. *Annals of the New York Academy of Sciences*, 508(1):333–348, 1987.

[24] Jens Frahm, Klaus-Dietmar Merboldt, and Wolfgang Hänicke. Localized proton spectroscopy using stimulated echoes. *Journal of Magnetic Resonance (1969)*, 72(3):502–508, 1987.

[25] J Frahm, H Bruhn, ML Gyngell, KD Merboldt, W Hänicke, and R Sauter. Localized high-resolution proton NMR spectroscopy using stimulated echoes: Initial applications to human brain in vivo. *Magnetic resonance in medicine*, 9(1):79–93, 1989.

[26] Philipp Mergenthaler, Ute Lindauer, Gerald A Dienel, and Andreas Meisel. Sugar for the brain: the role of glucose in physiological and pathological brain function. *Trends in neurosciences*, 36(10):587–597, 2013.

[27] Peter T Fox, Marcus E Raichle, Mark A Mintun, and Carmen Dence. Nonoxidative glucose consumption during focal physiologic neural activity. *Science*, 241(4864):462, 1988.

[28] Jun Shen, Kitt F Petersen, Kevin L Behar, Peter Brown, Terrence W Nixon, Graeme F Mason, Ognen AC Petroff, Gerald I Shulman, Robert G Shulman, and Douglas L Rothman. Determination of the rate of the glutamate/glutamine cycle in the human brain by in vivo ^{13}C NMR. *Proceedings of the National Academy of Sciences*, 96(14):8235–8240, 1999.

[29] João Duarte and Rolf Gruetter. Glutamatergic and gabaergic energy metabolism measured in the rat brain by ^{13}C NMR spectroscopy at 14.1T. *Journal of neurochemistry*, 126(5):579–590, 2013.

[30] Tom WJ Scheenen, Dennis WJ Klomp, Jannie P Wijnen, and Arend Heerschap. Short echo time ^{1}H-MRSI of the human brain at 3T with minimal chemical shift displacement errors using adiabatic refocusing pulses. *Magnetic resonance in medicine*, 59(1):1–6, 2008.

[31] Roger J Ordidge, Alan Connelly, and Joost AB Lohman. Image-selected in vivo spectroscopy (ISIS). A new technique for spatially selective NMR spectroscopy. *Journal of Magnetic Resonance (1969)*, 66(2):283–294, 1986.

[32] Tamer S Ibrahim and Lin Tang. Insight into RF power requirements and B_1 field homogeneity for human MRI via rigorous FDTD approach. *Journal of magnetic resonance imaging*, 25(6):1235–1247, 2007.

[33] Thomas Lange, Ulrike Dydak, TPL Roberts, HA Rowley, M Bjeljac, and P Boesiger. Pitfalls in lactate measurements at 3T. *American journal of neuroradiology*, 27(4):895–901, 2006.

[34] Dmitriy A Yablonskiy, Jeffrey J Neil, Marcus E Raichle, and Joseph JH Ackerman. Homonuclear J coupling effects in volume localized NMR spectroscopy: pitfalls and solutions. *Magnetic resonance in medicine*, 39(2):169–178, 1998.

[35] Petr Bednařík, Ivan Tkáč, Federico Giove, Mauro DiNuzzo, Dinesh K Deelchand, Uzay E Emir, Lynn E Eberly, and Silvia Mangia. Neurochemical and BOLD responses during neuronal activation measured in the human visual cortex at 7 Tesla. *Journal of Cerebral Blood Flow & Metabolism*, 35(4):601–610, 2015.

[36] Axel Haase, Jens Frahm, Wolfgang Hanicke, and Dietmar Matthaei. ^{1}H NMR chemical shift selective (CHESS) imaging. *Physics in medicine and biology*, 30(4):341, 1985.

[37] JB Murdoch and DA Lampman. Beyond WET and DRY: optimized pulses for water suppression. In *Proceedings of the Society of Magnetic Resonance in Medicine, 12th Meeting*, page 1191, 1993.

[38] K Kaminska, Jerzy Walecki, Paweł Grieb, and Piotr Bogorodzki. Magnetic resonance spectroscopy - state of art and future. *Polish Journal of Radiology*, 72(1):71–75, 2007.

[39] I Tkáč, Z Starčuk, I-Y Choi, and R Gruetter. In vivo ^{1}H NMR spectroscopy of rat brain at 1ms echo time. *Magnetic resonance in medicine*, 41:649–656, 1999.

[40] Axel Haase. Localization of unaffected spins in NMR imaging and spectroscopy (LOCUS spectroscopy). *Magnetic resonance in medicine*, 3(6):963–969, 1986.

[41] Rolf Gruetter. Automatic, localized in vivo adjustment of all first-and second-order shim coils. *Magnetic resonance in medicine*, 29(6):804–811, 1993.

[42] Tamer S Ibrahim, Robert Lee, Brian A Baertlein, Amir M Abduljalil, Hui Zhu, and Pierre-Marie L Robitaille. Effect of RF coil excitation on field inhomogeneity at ultra high fields: a field optimized tem resonator. *Magnetic resonance imaging*, 19(10):1339–1347, 2001.

[43] Wouter M Teeuwisse, Wyger M Brink, and Andrew G Webb. Quantitative assessment of the effects of high-permittivity pads in 7 Tesla MRI of the brain. *Magnetic resonance in medicine*, 67(5):1285–1293, 2012.

[44] DM Doddrell, DT Pegg, and M Ro Bendall. Distortionless enhancement of NMR signals by polarization transfer. *Journal of Magnetic Resonance (1969)*, 48(2):323–327, 1982.

[45] I Tkáć and R Gruetter. Methodology of ^{1}H NMR spectroscopy of the human brain at very high magnetic fields. *Applied magnetic resonance*, 29(1):139, 2005.

[46] Stephen W Provencher. Estimation of metabolite concentrations from localized in vivo proton NMR spectra. *Magnetic resonance in medicine*, 30(6):672–679, 1993.

[47] Leentje Vanhamme, Aad van den Boogaart, and Sabine Van Huffel. Improved method for accurate and efficient quantification of MRS data with use of prior knowledge. *Journal of Magnetic Resonance*, 129(1):35–43, 1997.

[48] A Naressi, C Couturier, JM Devos, M Janssen, C Mangeat, R De Beer, and D Graveron-Demilly. Java-based graphical user interface for the MRUI quantitation package. *Magnetic resonance materials in physics, biology and medicine*, 12(2-3):141–152, 2001.

[49] BJ Soher, P Semanchuk, D Todd, J Steinberg, and K Young. VESPA: Integrated applications for RF pulse design, spectral simulation and MRS data analysis. In *Proceedings of the International Society for Magnetic Resonance in Medicine, 19th Scientific Meeting and Exhibition*, page 1410, 2011.

[50] Ivan Tkáč, Raghavendra Rao, Michael K Georgieff, and Rolf Gruetter. Developmental and regional changes in the neurochemical profile of the rat brain determined by in vivo ^{1}H NMR spectroscopy. *Magnetic Resonance in Medicine*, 50(1):24–32, 2003.

[51] Heiko Neeb, V Ermer, T Stocker, and N Jon Shah. Fast quantitative mapping of absolute water content with full brain coverage. *Neuroimage*, 42(3):1094–1109, 2008.

[52] Thao Tran, Brian Ross, and Alexander Lin. Magnetic resonance spectroscopy in neurological diagnosis. *Neurologic clinics*, 27(1):21–60, 2009.

[53] Charles Gasparovic, Tao Song, Deidre Devier, H Jeremy Bockholt, Arvind Caprihan, Paul G Mullins, Stefan Posse, Rex E Jung, and Leslie A Morrison. Use of tissue water as a concentration reference for proton spectroscopic imaging. *Magnetic resonance in medicine*, 55(6):1219–1226, 2006.

[54] AA De Graaf, JE Van Dijk, and WMMJ BoéE. QUALITY: quantification improvement by converting lineshapes to the Lorentzian type. *Magnetic resonance in medicine*, 13(3):343–357, 1990.

[55] Roland Kreis. Issues of spectral quality in clinical ^{1}H-magnetic resonance spectroscopy and a gallery of artifacts. *NMR in Biomedicine*, 17(6):361–381, 2004.

[56] Roland Kreis, Lucie Hofmann, Beatrice Kuhlmann, C Boesch, Emilio Bossi, and Petra S Hüppi. Brain metabolite composition during early human brain development as measured by quantitative in vivo ^{1}H magnetic resonance spectroscopy. *Magnetic resonance in medicine*, 48(6):949–958, 2002.

Chapter 4

The effect of the chemical shift displacement artefact on the ^{1}H lactate signal

4.1 Introduction

The measurement of lactate concentration has generated great interest over the years due to its role as a potential indicator for several conditions associated with abnormal anaerobic metabolism. Elevated concentrations of lactate, which can exceed 10 mM, are observed in situations where blood flow, hence also oxygen supply, might be restricted, such as in ischemic stroke [1] and tumours [2]. Transient increases in lactate levels have also been observed in human brain following neuronal activation [3, 4, 5] and hyperventilation [6].

lactate detection with ^{1}H magnetic resonance spectroscopy (MRS) is challenging due to its low concentration in normal brain tissue ($\sim$1 mM) and overlap with signals of higher concentration compounds, namely macromolecules (MM) and lipids. To resolve the lactate methyl signal at 1.31 ppm from its overlapping resonances, some MRS methods exploit J-modulation effects in combination with the use of a long echo time (TE) to reduce the intensity of the MM and lipid signal. The point-resolved spectroscopy (PRESS) [7] sequence has been widely used for lactate detection in a clinical setting (field strengths of 3 T and lower). In this spin-echo based experiment, J-evolution operates on the methyl group, which is refocused by the 180° pulses, to obtain an inverted doublet peak at a TE of 144 ms (1/J, J = 6.933 Hz).

On the other hand, ultra high-field, which offers increased signal-to-noise ratio

(SNR) and spectral resolution, imposes some constraints on the use of the PRESS sequence. Due to the limited bandwidth of the slice-selective refocusing pulses, this sequence is associated with a large chemical shift displacement artefact (CSDA), which is worsened with increasing magnetic field strength. Due to the larger bandwidth of the 90° pulses relative to the 180° pulses, the stimulated echo acquisition mode (STEAM) [8, 9] sequence minimises the CSDA effects compared to the PRESS sequence, which makes the former a popular sequence for use at higher field strengths. The modulation in the STEAM sequence arising from scalar coupling is governed by both TE and mixing time (TM).

The optimisation of the STEAM sequence timing parameters has been investigated for the improved acquisition of scalar-coupled metabolites at ultra high-field, such as glutamate [10, 11, 12]. For lactate measurement, previous work reported an analytical expression derived for the STEAM signal modulation in a weakly-coupled spin system of the lactate form [13], AX_3, where A corresponds to the proton in the methine group and X to those in the methyl group. However, the effects of the CSDA were not included in the latter, it being assumed that both chemical groups experience all 90° pulses.

Although STEAM simulations performed at 4 T with a TE of 70 ms have not shown substantial localisation artefacts for weakly-coupled spin systems [14], the effects of the CSDA should be taken into account when using longer TEs (144 ms) at higher field strengths. Analytical solutions for the response of the STEAM signal have been obtained considering the effect of the CSDA in two dimensions [15]. Numerical solutions incorporating two [16] and three-dimensional [14] localisation have also been implemented.

However, there is no complete three-dimensional analytical model with the consideration of the CSDA for assisting the optimisation of the STEAM sequence in the detection of weakly-coupled spin systems (AX_n). The model derived in this work will enable the accurate determination of the signal as a function of TE, TM and pulse bandwidth for any AX_n metabolite, including lactate (n=3), as well as the localisation of the signal throughout the excited region. This model was validated with a phantom experiment and was also applied to the optimisation of the STEAM sequence timing parameters for lactate detection in the human brain.

4.2 Theory

The STEAM sequence (Figure 3.11) is composed of three slice-selective 90° pulses, each of which is subject to a CSDA. The excited volume, defined as the region in which at least one of the A or X spins is excited by at least one of the radiofrequency (RF) pulses, can be segmented into partial volumes, according to the excitation pattern. For each direction there are three possible patterns of excitation, two in which only one of the spins experiences the pulse (A or X spins) and one in which both spins experience the pulse. Therefore, the excited volume comprises a total of 3x3x3 = 27 compartments (Figure 4.1).

The product operator formalism was used to derive expressions for the X spin signal from each compartment as a function of TE and TM, following the convention defined in [17]. Signal modulation in the central compartment (number 14 in Figure 4.1c and shown in darker blue in Figure 4.1b) has been previously described in [13]. It is referred to as the 'ideal condition', in which both chemical groups experience all three RF pulses. This work extends the analysis to include the remaining compartments, which is required to fully describe the three-dimensional model. A similar approach to [13] was adopted here: all 90° pulses were assumed to be hard, applied with a phase of 0°.

After the application of the first pulse (see Figure 3.11), which transforms longitudinal (L) into transverse magnetisation (single-quantum coherence, SQ), each of the spins will undergo chemical shift and J-coupling evolution during TE/2. The objective is to determine the X spin signal: some of this arises directly from excitation of X spins, some is transferred to the X spins from the excited A spins. Thus, A spins terms that do not contribute to the transfer of transverse magnetisation to the X spins or will generate higher-order coherences in the next interval are excluded. After the second pulse, the transverse magnetisation is converted to longitudinal, single- and multiple-quantum coherences terms. Only those terms insensitive to the gradient G_2 applied in the TM period will survive, i.e., zero-quantum coherences (ZQ) and longitudinal magnetisation; transverse and higher-order coherences are dephased by the gradient. The final pulse is used to convert the longitudinal and zero-quantum coherences back to single-quantum

terms, which can be detected in the acquisition period. The dephasing created by the gradient G_1 in the first TE/2 interval is recovered by the gradient G_3 present in the last TE/2 interval. In addition, only in-phase signal at the X spins resonance and detected in the y axis was considered. The possible coherence pathways contributing to the X spin resonance (top) and the respective signals (bottom) are:

$$SQ^A \xrightarrow{90^\circ} ZQ^{AX} \xrightarrow{90^\circ} SQ^X$$
$$S_{A1} = \frac{1}{4} sin^2\left(\frac{\pi JTE}{2}\right) cos^{n-1}\left(\frac{\pi JTE}{2}\right) cos^{n-1}(\pi JTM)\, cos\,(2\pi\Delta\Omega TM)\, cos\,(\pi\Delta\Omega TE)$$

$$SQ^A \xrightarrow{90^\circ} ZQ^{AX} \xrightarrow{90^\circ} SQ^X$$
$$S_{A2} = \frac{1}{4} sin^2\left(\frac{\pi JTE}{2}\right) cos^{n-1}\left(\frac{\pi JTE}{2}\right) cos^{n-1}(\pi JTM)\, sin\,(2\pi\Delta\Omega TM)\, sin\,(\pi\Delta\Omega TE)$$

$$SQ^A \xrightarrow{90^\circ} L^{AX} \xrightarrow{90^\circ} SQ^X$$
$$S_{A3} = \frac{1}{2} sin^2\left(\frac{\pi JTE}{2}\right) cos^{n-1}\left(\frac{\pi JTE}{2}\right) cos\,(\pi\Delta\Omega TE)$$

$$SQ^X \xrightarrow{90^\circ} L^X \xrightarrow{90^\circ} SQ^X$$
$$S_{X1} = \frac{1}{2} cos^2\left(\frac{\pi JTE}{2}\right)$$

$$SQ^X \xrightarrow{90^\circ} ZQ^{AX} \xrightarrow{90^\circ} SQ^X$$
$$S_{X2} = \frac{1}{4} sin^2\left(\frac{\pi JTE}{2}\right) cos^{n-1}(\pi JTM)\, cos\,(2\pi\Delta\Omega TM)$$

$$SQ^X \xrightarrow{90^\circ} L^{AX} \xrightarrow{90^\circ} SQ^X$$
$$S_{X3} = \frac{1}{2} sin^2\left(\frac{\pi JTE}{2}\right), \tag{4.1}$$

where $\Delta\Omega$ is the chemical shift difference (in Hz) between A and X spins. S_{A1}, S_{A2} and S_{A3} represent the signal contribution arising from A spins, while S_{X1}, S_{X2} and S_{X3} arise from X spins. The derivation of S_{A1} is shown in the appendix, as an example of the application of the product operator formalism in this work. For the plane in which both spins experience the first 90° pulse, nine compartments (3x3) can be identified (compartments 10 to 18, as depicted in Figure 4.1c). The

first 9 compartments represent the plane in which only A spins experience the first pulse (Figure 4.1a) and in compartments 19 to 27 only X spins experience the pulse (Figure 4.1d). The signal in these two planes is equivalent to that in the central plane, excluding the contributions related to the spin that is not affected by the first pulse. Thus, if the X spins are not affected by the first pulse, the chemical shift dephasing in the last interval is not refocused. With respect to the A spins, their magnetisation would remain oriented along the longitudinal axis after the first pulse and, it would not therefore be possible to transfer any magnetisation to the X spins.

Expressions for the signal from each compartment are given in Figure 4.1 (see Eqs. 4.1). Their relative contribution to the overall signal depends on the volume of the individual compartments. As defined in subsection 3.3.1.1, k, the ratio between the chemical shift difference and the bandwidth determines the volume of each compartment. The expressions for the partial volumes contain the products of k or $1-k$ factors, in which k applies when only one of the spins experiences a given pulse and $1-k$ when both do. The weightings are shown in Figures 4.1a-d for each compartment. In the central slice, at least one factor of $(1-k)$ is present as all spins are affected by the first pulse. The remaining factors for each compartment are selected according to the spins excited by the second and third pulses. For example, in compartment 16 only A spins are affected by those pulses, which results in an additional k^2 contribution.

Provided the metabolite of interest is uniformly distributed throughout the excited region (homogeneous case), the net signal S is given by:

$$S = S_{X1} - S_{X2}\left(1-k^2\right) + S_{X3}k^2 + S_{A1}\left(1+k^2\right) - 2S_{A2}k\,(1-k) + S_{A3}k^2. \quad (4.2)$$

Note that the net signal is the same as would be obtained from a model that just considers the central plane (two dimensional model), and thus the resulting modulation pattern is also equivalent. However, this simplified approach does not fully reflect the spatial origin of the signal contributions.

Note also that when TE is very short (TE$\sim$ 0) or is set to a multiple of 2/J, e.g., TE = 288 ms, for the methyl group of lactate, all terms vanish due to the $sin^2\left(\pi JTE/2\right)$ term, except one and Eq. 4.2 simplifies to $S = S_{X1}$. This indicates

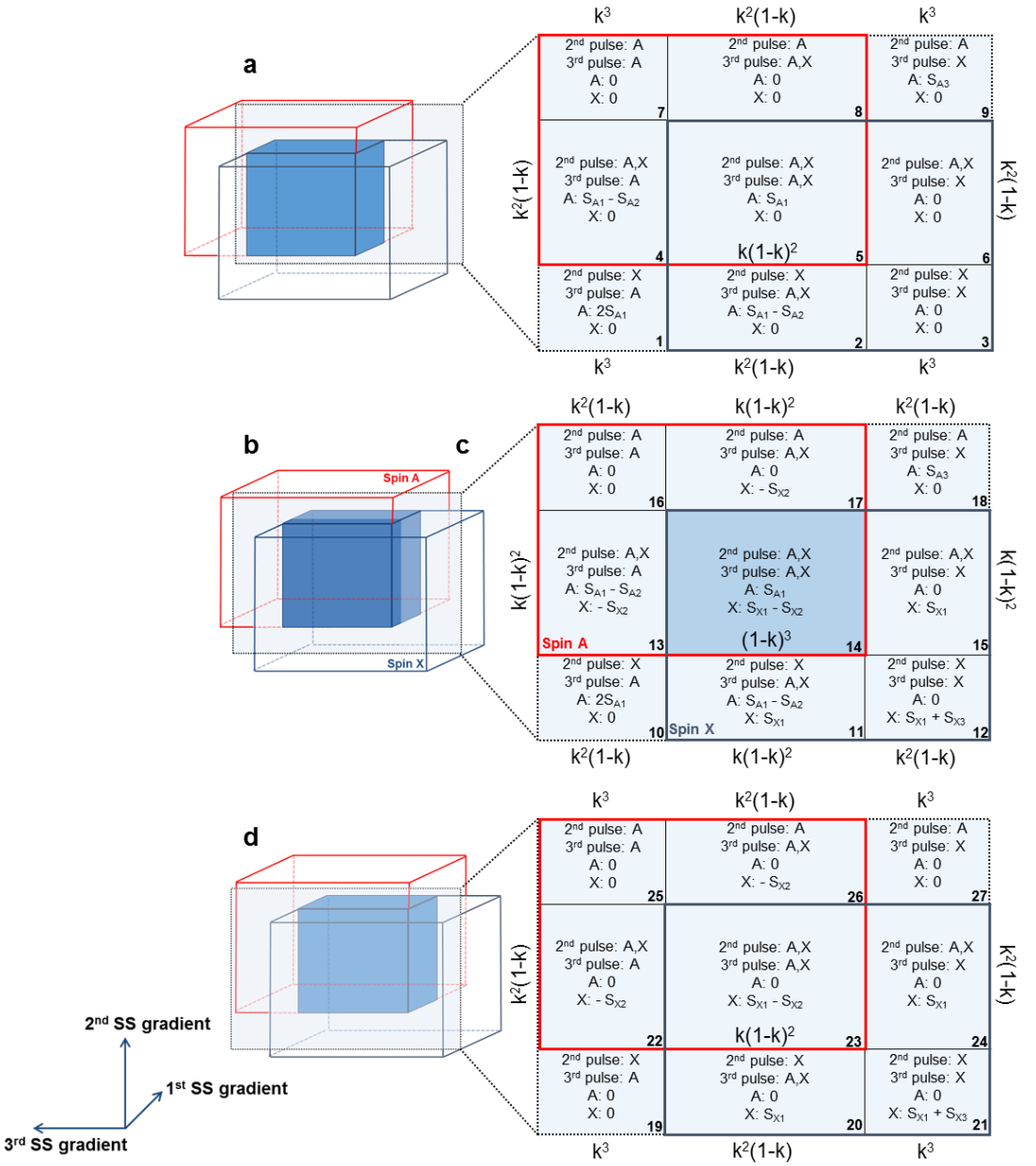


Figure 4.1: Representation of the CSDA effects in three dimensions on the weakly-coupled spin system signal during a STEAM sequence. The excited volume can be decomposed into 3 regions in each slice selection (SS) direction, two where only one of the spins experiences the pulse and one in which both do. The central plane depicted in b) and in more detail in c) represents the set of compartments, in which A and X spins are affected by the first pulse. The planes in which only the A or X spins experience the first pulse are also represented in a) and d), respectively. The signal yielding from each chemical group is shown for each compartment, as well as the weightings for the calculation of the partial volumes, where k is the ratio between the chemical shift difference and RF bandwidth.

that the signal is independent of the CSDA effects (not dependent on k). For uncoupled spins ($J = 0$), Eq. 4.2 reduces to $S = 1/2$, validating the well-known fact that the STEAM signal is half the original magnetisation. The analytic expressions of Eqs. 4.1 were implemented in MATLAB (Mathworks, Natick, Massachusetts,

USA), with $n = 3$, making it possible to express the amplitude of the lactate doublet as a function of sequence parameters, TE and TM, pulse bandwidth and field strength. The effects of T_2 relaxation were not taken into account in this model. lactate chemical shifts and J-coupling constant were taken from [18].

4.3 Methods

Magnetic resonance (MR) measurements were performed on a 7 T Philips Achieva MR system (Philips Healthcare, Best, Netherlands) with a 32-channel receive head coil (Nova Medical, Wilmington, Massachusetts, USA) and a volume transmit coil (Nova Medical) with a maximum transmit B_1 field of 20 μT. *In vitro* acquisitions were performed to validate the simulations using a spherical phantom (85 mm diameter) that contained metabolites with similar concentrations to those found in normal brain: 10 mM of N-acetylaspartate (NAA), 8 mM of creatine, 3 mM of choline, 1 mM of lactate, 6 mM of myo-inositol, 10 mM of glutamate, 5 mM of glutamine and 2 mM of 4,4-dimethyl-4-silapentane-1-sulfonic acid (DSS) as a reference. To illustrate a whole cycle of TM modulation, ^{1}H MRS data were acquired from a 30x30x30 mm^3 voxel positioned in the centre of this phantom using a STEAM sequence (repetition time - TR/TE = 2400/144 ms, number of averages = 128) with a series of TM values (from 16.1 to 17.4 ms and a step size of 0.1 ms). The three 90° pulses used in the STEAM sequence had a bandwidth of 3110 Hz ($k = 0.27$). Water suppression was performed with the variable pulse powers and optimised relaxation delays (VAPOR) [19] scheme and unsuppressed water spectra were also acquired before each scan. A second-order pencil-beam volume shimming, a Philips routine based on fast, automatic shimming technique by mapping along projections (FASTMAP) [20], was applied across the volume-of-interest (VOI) that corresponded to the water frequency and the shifted VOI that corresponded to lactate.

Area integration was used to quantify the lactate doublet (X resonance, 1.31 ppm) in the TM series of proton spectra using a home-built script in MATLAB. All the area values were normalised to the maximum value of the TM series for comparison with the theoretical values.

To demonstrate the applicability of this analytical model of the STEAM sequence *in vivo*, ^{1}H MRS data were collected from a voxel ($40\times30\times25\,mm^3$) positioned, as depicted in Figure 4.5, within a healthy human brain (27 years old, female). The subject gave informed consent to the protocol approved by the local ethics committee. Based on the findings from the simulations and *in vitro* experiment, the minimum TM value (16.9 ms), limited by the dephasing gradient duration, that resulted in a maximal inversion of the lactate doublet for a TE = 144 ms, was used. For comparison, a second acquisition with a longer TE, multiple of 2/J (TE = 288ms) and the same TM was performed. As shown above, the CSDA effects should not contribute to signal cancellation in this case. Both spectra were acquired over a period of approximately 11 minutes (number of averages = 264, TR = 2500 ms). The spectra were phase corrected and visualised using MATLAB with 2 Hz of line broadening.

4.4 Results

Expressions for the signal from each compartment are given in Figure 4.1. Eqs. 4.1 reveal their dependence on TE and TM. The expression derived for the central compartment, where all ^{1}H resonances experience the entire pulse sequence, is in agreement with the one published in [13, 21]. Figures 4.2a-c show the location of the compartments and their contributions to the total signal for TE values of 72, 144 and 288 ms, respectively. This is illustrative for the methyl group of lactate at 7 T. The amplitudes have been scaled according to their partial volumes given in Figure 4.1, using a k factor of 0.27, as defined by the bandwidth of 3110 Hz, used for the experimental work.

Note that for a TE value of 288 ms, $sin^2\left(\pi JTE/2\right) = 0$, so all signal components in Eqs. 4.1 vanish apart from S_{X1} and there is no dependency on TM. For a TE of 144 ms, $cos\left(\pi JTE/2\right) = 0$, and so S_{A1}, S_{A2}, S_{A3} and S_{X1} terms all vanish, leaving just S_{X2} and S_{X3} terms non-zero. Of these, only S_{X2} has a dependence on TM. For TE = 72 ms (Figure 4.2a), most compartments contribute to the total signal. The total signal is given by Eq. 4.2. It is plotted in Figure 4.3 as a function of TM for the same three TE values. Note again the lack of dependence on

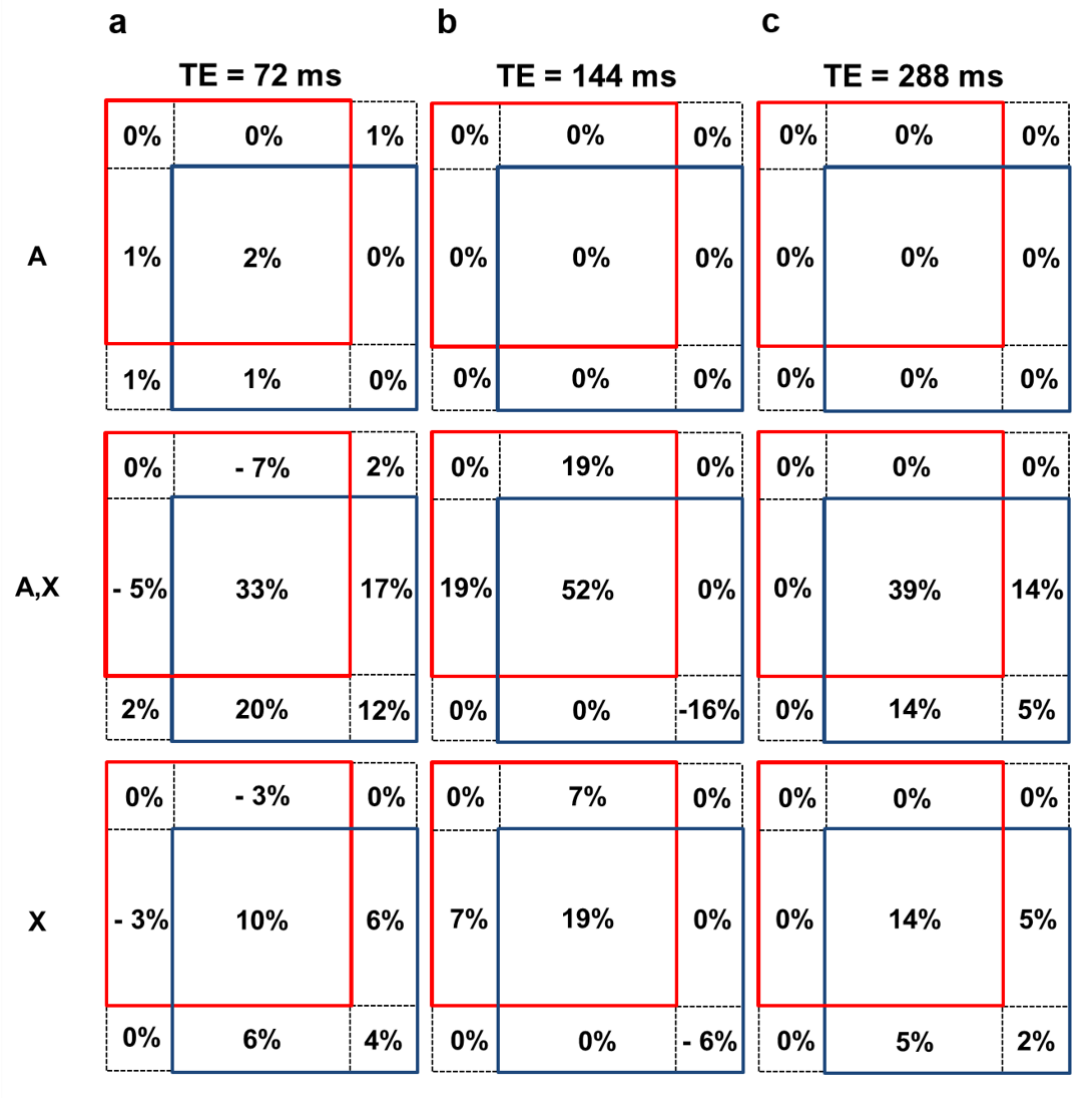


Figure 4.2: Simulation of the relative contributions for the resulting lactate methyl group signal from each compartment of the three-dimensional model for TE values of 72, 144 and 288 ms in a STEAM sequence. The first row represents the plane where only A spins experience the first pulse, the middle row indicates the central plane, where both chemical groups experience the same pulse and the last row represents the plane where only X spins experience the first pulse. Simulation parameters are TM = 16.9 ms, magnetic field strength of 7 T and pulse bandwidth of 3110 Hz.

TM and the CSDA for TE = 288 ms, and that thus yields the maximum signal (ignoring relaxation effects). When TE = 144 ms, an inversion of the lactate peak is obtained, reaching its maximum at TM = 16.9 ms. The efficiency of the inversion is reduced when the CSDA is taken into account in the simulations, when compared to the 'ideal condition', which would invert half of the initial magnetisation (-0.5). For TE = 72 ms, the signal is never maximised nor inverted, thus diminishing the suitability for *in vivo* applications.

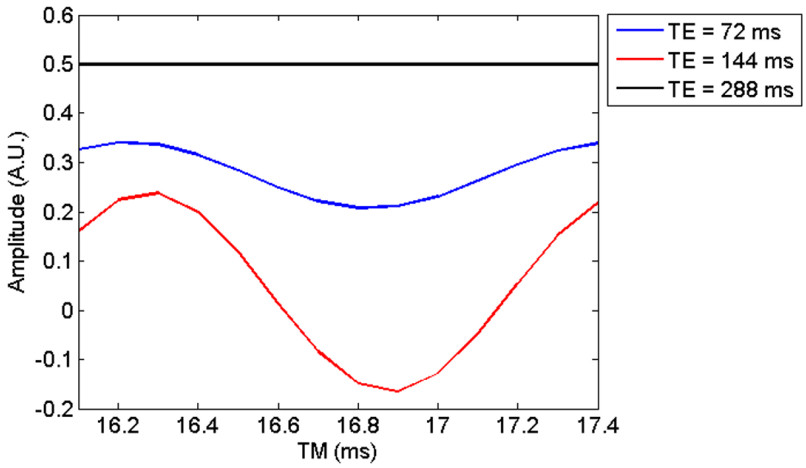


Figure 4.3: Simulation of the lactate methyl group net signal in the excited volume as a function of TM for TE values of 72, 144 and 288 ms in a STEAM sequence. Simulation parameters are magnetic field strength of 7 T and pulse bandwidth of 3110 Hz.

The experimental TM dependence of the total signal for TE = 144 ms is shown in Figure 4.4 (individual points) and compared to the theoretical curve (solid line). Spectra recorded from the phantom at TM values of 16.3 (magenta arrow), 16.6 (red arrow) and 16.9 ms (black arrow) are shown in the inset of the figure.

Figure 4.5 shows the ^{1}H brain spectra obtained from the human volunteer using a TE of 144 (upper trace) and 288 ms (lower trace) and a TM of 16.9 ms, chosen to give the maximum inverted signal for the lactate doublet at TE = 144 ms (see Figure 4.4). Clear signals from the methyl group of lactate are seen in both cases (inverted in the case of TE = 144 ms).

4.5 Discussion

The quantum mechanical formulation of the coherence pathways in PRESS is relatively straightforward, as the two selective 180° pulses can be treated independently of each other, in contrast with the selective 90° pulses in the STEAM sequence which act in combination to induce a stimulated echo [16]. In this work, simulations based on the derived analytical expressions in the product operator formalism allowed a better understanding of the spatial distribution of a weakly-coupled spin system signal, as a function of the STEAM sequence parameters. The simulations revealed that for a homogeneous volume, the spatial sum of the signal

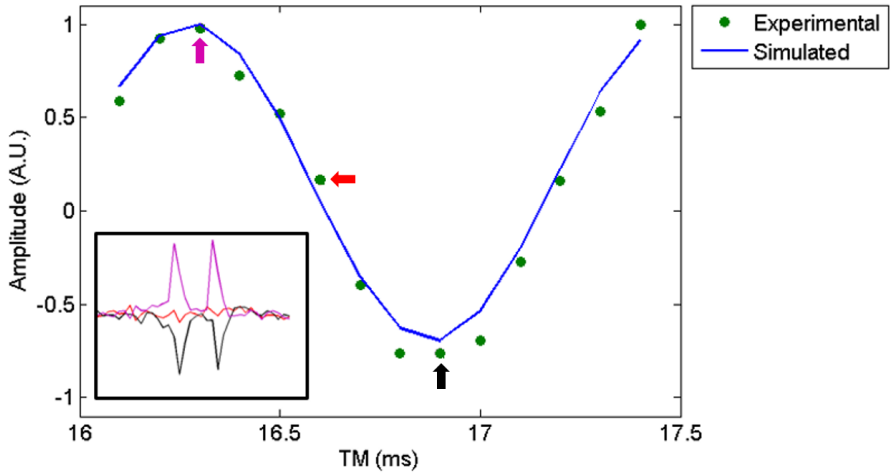


Figure 4.4: Experimental and predicted TM modulation pattern for the methyl group of lactate (Lac). Experimental data were acquired from a phantom with approximate brain metabolite concentrations ([Lac] = 1 mM) at 7 T using a STEAM sequence (voxel size = 30x30x30 mm^3, TR/TE = 2400/144 ms, number of averages = 128 for TM values from 16.1 to 17.4 ms). The 90° pulse bandwidth was 3110 Hz. Representative spectra zoomed in the lactate doublet are also shown for key TM values (16.3, 16.6 and 16.9 ms).

from all the compartments in a two- and three-dimensional analysis will generate equivalent modulation patterns. Nevertheless, additional three-dimensional information illustrates an accurate spatially-discriminated signal generation, which can be useful in the case of an inhomogeneously distributed metabolite.

Considering the case of lactate (AX_3), it was found that for a TE value of 72 ms, the methyl group of lactate signal is not confined to a specific plane or set of compartments, while with a TE = 144 ms, there is no signal contribution from the plane where only A spins experience the first pulse; however the signal is still distributed throughout the excited volume. On the other hand, with TE = 288 ms, the net signal is restricted to the VOI of the methyl group of lactate, which demonstrates the signal independence of k and therefore of the CSDA. The fact that, with this TE value, the signal arises from a region with defined boundaries can be exploited to optimise the positioning of the spectroscopy voxel; if the focus of the measurement is the methyl group of lactate, the VOI for this chemical group should coincide with the region of interest one desires to acquire signal from.

The information on the lactate signal distribution within the excited volume was also used in the work of Edden et al. [22], which suggested the combined use of inner volume saturation bands and the PRESS sequence with a TE = 144 ms at 3 T, to remove the contribution of compartments that lead to signal cancellation.

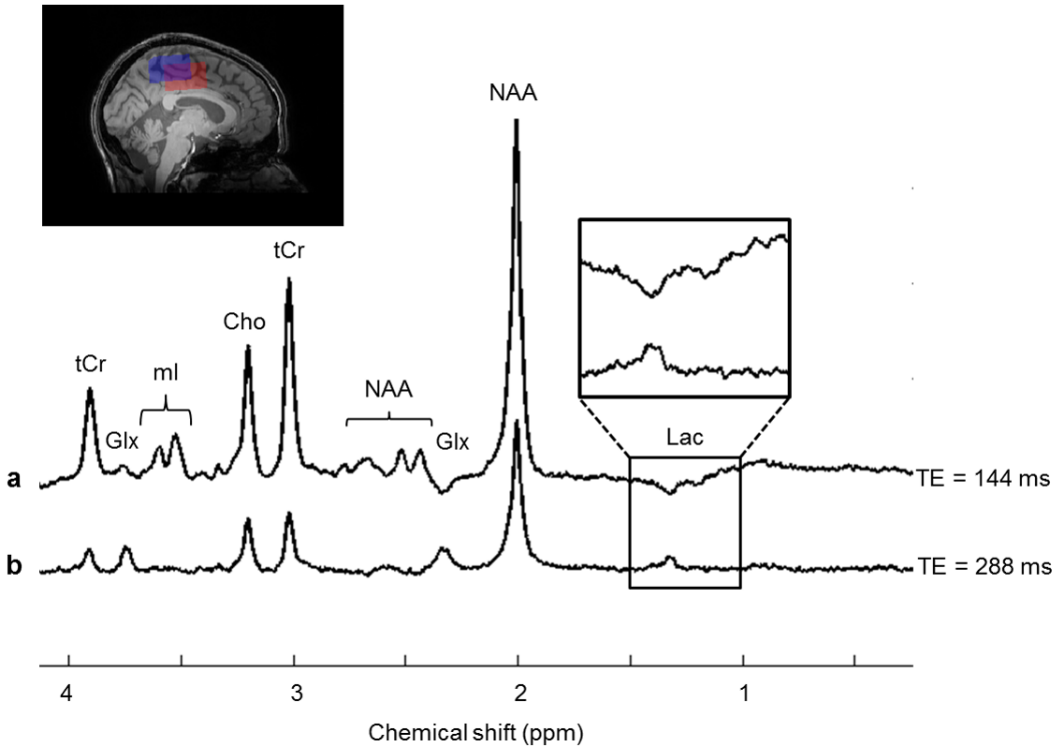


Figure 4.5: Spectra acquired with the STEAM sequence using a) the optimised TM for the inversion of the lactate (Lac) peak (TR/TE/TM = 2500/144/16.9 ms) and b) the optimised TE for attenuation of the CSDA (TR/TE/TM = 2500/288/16.9 ms). A $40\times30\times25\,\mathrm{mm}^3$ voxel was placed in the brain of a healthy volunteer and 264 averages were used to obtain the spectra. The red box represents the voxel at the lactate frequency and blue box the voxel at the water frequency (pulse bandwidth = 2799 Hz). The spectra were phase corrected and displayed in MATLAB with 2 Hz of line broadening. Glx represents the combined peaks of glutamate and glutamine. PCr - total creatine, mI - myo-inositol, Cho - choline.

In this work, it was shown that with the STEAM sequence some compartments also contribute negatively to the net signal in the cases of TE = 72 and 144 ms. However, a similar strategy as used by Edden et al. cannot be easily applied with the STEAM sequence, as the position of the compartments which lead to unwanted signal is not as favourable as in the PRESS sequence. Moreover, the addition of saturation slabs to only retain the signal from the central compartment, which corresponds to the 'ideal situation', would result in a further signal reduction of approximately 50%. Nonetheless, it is possible to observe that at TE = 288 ms, all the compartments contribute positively to the overall signal, resulting in a maximal signal (neglecting the relaxation effects).

The simulations carried out with the proposed model also allowed the investigation of the signal modulation as a function of TM. It was possible to verify that with a TE = 288 ms, there is no TM modulation, while for a TE = 144 ms, the

TM modulation can be used to obtain an inverted lactate doublet. The TM that led to maximal inversion of the lactate peak for this TE, which matched in both theoretical and experimental data, was 16.9 ms. However, for a non-negligible pulse length, it is not possible to achieve a complete inversion, and the inversion efficiency depends on the RF bandwidth.

The performance of the STEAM sequence at TE = 144 ms with the optimal TM and at TE = 288 ms was assessed with an *in vivo* acquisition. Despite not being able to achieve 100% inversion efficiency, due to the limited bandwidth and the RF field inhomogeneities at 7 T, an inverted lactate peak was easily detectable in a healthy human brain (TE = 144 ms). By visual inspection of the spectrum acquired with TE = 288 ms, a positive lactate peak could be detected, comparable in magnitude with the one obtained with TE = 144 ms.

Additionally, in the acquisition with TE = 288 ms, the lactate signal was less affected by lipid and MM contamination, making this measurement less dependent on the individual lipid/MM content. Although it has been suggested that a general MM profile is sufficient for an accurate metabolite quantification at 7 T [23], individual variability in any of these superimposed signals could contribute to an over- or under-estimation of the lactate concentration.

As first proposed by Lange et al. [24] for 3 T acquisitions with the PRESS sequence, the use of TE = 288 ms can be a strategy to overcome the CSDA. Here, the non-dependence of the signal on the CSDA at TE = 288 ms and the non-significant relaxation losses allowed the detection of a clear lactate peak. Therefore, in acquisitions with the STEAM sequence at 7 T, it is recommended to use TE = 288 ms, with as short a TM as possible to minimise longitudinal relaxation. However, at higher-field strengths than 7 T, the use of TE = 144 ms might be more advantageous for lactate determination, due to the shorter transverse relaxation times. In this case, strategies to further increase the pulse bandwidth are required, which should focus on RF pulse design or the use of multi-channel RF transmission approaches.

Finally, it is also worth to reference the cases of AX and AX_2. With a TE = 144 ms, S_{X2} contains the expression $cos^{n-1}(\pi JTM)$, which is dependent on the number of X spins, n. Considering a different value for n will change the optimal

TM for inversion. With regards to TE = 288 ms, the only term that contributes to the signal is S_{X1}, which does not contain any dependence on n.

The effect of the CSDA on J-coupled spins at ultra high-field has raised the motivation for studies to provide a quantitative description of the signal loss using a quantum mechanical approach, while proposing several methods to mitigate its influence. This work demonstrated the feasibility of detecting lactate at 7 T with sufficient SNR and minimal contamination from lipids/MM by using a standard STEAM sequence with optimised timing parameters. This optimisation was carried out through the implementation of an analytical model that takes into account the CSDA in the three applied directions of field gradients for a correct determination of the weakly-coupled spin system signal.

Bibliography

[1] Dawn E Saunders. MR spectroscopy in stroke. *British medical bulletin*, 56(2):334–345, 2000.

[2] Martin Bulik, Radim Jancalek, Jiri Vanicek, Antonin Skoch, and Marek Mechl. Potential of MR spectroscopy for assessment of glioma grading. *Clinical neurology and neurosurgery*, 115(2):146–153, 2013.

[3] Benoît Schaller, Ralf Mekle, Lijing Xin, Nicolas Kunz, and Rolf Gruetter. Net increase of lactate and glutamate concentration in activated human visual cortex detected with magnetic resonance spectroscopy at 7 Tesla. *Journal of neuroscience research*, 91(8):1076–1083, 2013.

[4] Petr Bednařík, Ivan Tkáč, Federico Giove, Mauro DiNuzzo, Dinesh K Deelchand, Uzay E Emir, Lynn E Eberly, and Silvia Mangia. Neurochemical and BOLD responses during neuronal activation measured in the human visual cortex at 7 Tesla. *Journal of Cerebral Blood Flow & Metabolism*, 35(4):601–610, 2015.

[5] Ralf Mekle, Simone Kühn, Harald Pfeiffer, Semiha Aydin, Florian Schubert, and Bernd Ittermann. Detection of metabolite changes in response to a varying visual stimulation paradigm using short-TE ^{1}H MRS at 7T. *NMR in Biomedicine*, 30(2):e3672, 2017.

[6] Richard AE Edden, Ashley D Harris, Kevin Murphy, C John Evans, Neeraj Saxena, Judith E Hall, Damian M Bailey, and Richard G Wise. Edited MRS is sensitive to changes in lactate concentration during inspiratory hypoxia. *Journal of Magnetic Resonance Imaging*, 32(2):320–325, 2010.

[7] Paul A Bottomley. Spatial localization in NMR spectroscopy in vivo. *Annals of the New York Academy of Sciences*, 508(1):333–348, 1987.

[8] Jens Frahm, Klaus-Dietmar Merboldt, and Wolfgang Hänicke. Localized proton spectroscopy using stimulated echoes. *Journal of Magnetic Resonance (1969)*, 72(3):502–508, 1987.

[9] J Frahm, H Bruhn, ML Gyngell, KD Merboldt, W Hänicke, and R Sauter. Localized high-resolution proton NMR spectroscopy using stimulated echoes: Initial applications to human brain in vivo. *Magnetic resonance in medicine*, 9(1):79–93, 1989.

[10] Alessandra Toncelli, Ralph Noeske, Mirco Cosottini, Mauro Costagli, Valentina Domenici, Gianluigi Tiberi, and Michela Tosetti. STEAM-MiTiS:

An MR spectroscopy method for the detection of scalar-coupled metabolites and its application to glutamate at 7T. *Magnetic resonance in medicine*, 74(6):1515–1522, 2015.

[11] Weiqiang Dou, Jörn Kaufmann, Meng Li, Kai Zhong, Martin Walter, and Oliver Speck. The separation of Gln and Glu in STEAM: a comparison study using short and long TEs/TMs at 3 and 7T. *Magnetic Resonance Materials in Physics, Biology and Medicine*, 28(4):395–405, 2015.

[12] Shaolin Yang, Jiani Hu, Zhifeng Kou, and Yihong Yang. Spectral simplification for resolved glutamate and glutamine measurement using a standard steam sequence with optimized timing parameters at 3, 4, 4.7, 7, and 9.4T. *Magnetic resonance in medicine*, 59(2):236–244, 2008.

[13] Alan H Wilman and Peter S Allen. An analytical and experimental evaluation of STEAM versus PRESS for the observation of the lactate doublet. *Journal of Magnetic Resonance, Series B*, 101(1):102–105, 1993.

[14] Lana G Kaiser, Karl Young, and Gerald B Matson. Numerical simulations of localized high field ^{1}H MR spectroscopy. *Journal of magnetic resonance*, 195(1):67–75, 2008.

[15] E Wrenn Wooten, Dmitriy A Yablonskiy, and Joseph J H Ackerman. Spatial interference effects due to scalar coupling interactions in STEAM. In *Proceedings of the International Society for Magnetic Resonance in Medicine, 9^{th} Scientific Meeting and Exhibition*, page 1687, 2001.

[16] Richard B Thompson and Peter S Allen. Response of metabolites with coupled spins to the STEAM sequence. *Magnetic resonance in medicine*, 45(6):955–965, 2001.

[17] Malcolm H Levitt. *Spin dynamics: basics of nuclear magnetic resonance*. John Wiley & Sons, 2001.

[18] Varanavasi Govindaraju, Karl Young, and Andrew A Maudsley. Proton NMR chemical shifts and coupling constants for brain metabolites. *NMR in Biomedicine*, 13(3):129–153, 2000.

[19] I Tkáč, Z Starčuk, I-Y Choi, and R Gruetter. In vivo ^{1}H NMR spectroscopy of rat brain at 1ms echo time. *Magnetic resonance in medicine*, 41:649–656, 1999.

[20] Rolf Gruetter. Automatic, localized in vivo adjustment of all first-and second-order shim coils. *Magnetic resonance in medicine*, 29(6):804–811, 1993.

[21] Karl Young, Gerald B Matson, Varanavasi Govindaraju, and Andrew A Maudsley. Spectral simulations incorporating gradient coherence selection. *Journal of Magnetic Resonance*, 140(1):146–152, 1999.

[22] Richard AE Edden, Michael Schär, Argye E Hillis, and Peter B Barker. Optimized detection of lactate at high fields using inner volume saturation. *Magnetic resonance in medicine*, 56(4):912–917, 2006.

[23] Benoît Schaller, Lijing Xin, and Rolf Gruetter. Is the macromolecule signal tissue-specific in healthy human brain? A ^{1}H MRS study at 7 Tesla in the occipital lobe. *Magnetic resonance in medicine*, 72(4):934–940, 2014.

[24] Thomas Lange, Ulrike Dydak, TPL Roberts, HA Rowley, M Bjeljac, and P Boesiger. Pitfalls in lactate measurements at 3T. *American journal of neuroradiology*, 27(4):895–901, 2006.

Chapter 5

Investigation of cerebral metabolic changes during a prolonged visual stimulus using ^{1}H MRS

5.1 Introduction

The study of the metabolic fluctuations during neuronal stimulation has been a topic of interest since Fox and colleagues [1] evidenced the uncoupling between glucose consumption and the cerebral metabolic rate of oxygen ($CMRO_2$). Previous works have attributed this mismatch to a rise in non-oxidative metabolism during brain activation, as a means to respond to the energy demand. Despite being a less energetically efficient process, the temporarily increased non-oxidative reactions can potentially generate adenosine triphosphate (ATP) faster than through glucose oxidation, in particular using the fast conversion of pyruvate, the end-product of glycolysis, into lactate. This hypothesis was supported by an observed increase in the concentration of lactate during neuronal activation. [2]. Alternatively, these transient increases in lactate levels have been suggested to be linked to the astrocyte-neuron lactate shuttle model [3]. This model associates the rise in lactate concentration to a global increase in glucose consumption, which is higher in the astrocytes, where the process is considered to be predominantly non-oxidative, than in neurons.

The first measurements performed with *in vivo* magnetic resonance spectroscopy (MRS) to determine lactate concentration changes during visual stimulation de-

tected a rise in lactate levels of 57% [2], 170% [4] and 250% [5], while a study by Merboldt et al. [6] reported an absence of lactate accumulation. Although the results of the initial studies were contradictory, consistent response patterns of lactate concentration upon visual stimulation have been reported at 7 T, benefiting from the increase in signal-to-noise ratio (SNR) and spectral resolution at ultra high-field. The average rises in lactate levels during visual stimulation were in the range of 7% to 37% [7, 8, 9, 10, 11, 12], reaching steady-state during stimulation, which was maintained until the end of the stimulus in most studies. On the contrary, Lin et al. [8] observed a transient increase in lactate levels with a subsequent return toward baseline during neuronal activation. This discrepancy was proposed to be related to the choice of stimulus (moving wedges), which excited distinct neuronal populations from the remaining studies that used a flashing checkerboard.

Due to the low concentration of lactate in normal brain tissue, the majority of functional MRS (fMRS) studies used short echo time (TE) sequences, reducing signal loss by transverse relaxation mechanisms. However, with this method the accurate determination of lactate, whose resonances overlap with higher amplitude signals, in particular macromolecules (MM), can be challenging. In this case, the dissociation of the MM/lipid and lactate contributions is accomplished by linear fitting of the model spectra. Nonetheless, even in brain tissue, where lipid contamination is less intense than in the muscle, the robustness of the fitting might depend on the a priori knowledge set into the degrees of freedom of the MM profile.

In addition, the spectral quantification with a general measured MM profile may not be sufficiently robust to account for inter-subject variability in the different MM components. A previous study investigating whether tissue-specific MM signal affects metabolite quantification showed that a general MM profile provides an accurate determination of most metabolites [13]. However, significant differences in lactate levels were found between spectral quantification with a MM profile acquired from a predominantly white or gray matter rich tissue.

To resolve the lactate signal from overlapping resonances, several methods that make use of J-modulation effects have been proposed. Despite limiting the num-

ber of measured metabolites, the use of a longer TE acquisition is an attractive approach to dissociate lactate from other signals and has been shown to be feasible for fMRS studies [11]. With TE = 144 ms, the lactate doublet at 1.31 ppm is inverted, while the intensity of the lipid and MM signals is substantially reduced. The use of multiple-quantum filters has been shown at 7 T [14]. These require the application of pulses centred on lactate resonances and the use of crusher gradients to dephase non-coupled resonances. However, selective excitation with quantum filters is challenging, because the performance of such filters degrades rapidly in inhomogeneous magnetic fields. Furthermore, an additional measurement is also required to obtain the non-coupled resonances.

Another common technique to eliminate co-resonant signals is J-difference editing. This technique is employed in Mescher-Garwood (MEGA) sequences, such as the MEGA-semiadiabatic localisation by adiabatic selective refocusing (sLASER) sequence [15, 16, 17]. At least two measurements are required: in the first one the J-modulation is allowed to evolve, resulting in an inverted doublet signal for the selected TE, while the other non-coupled resonances remain unchanged; in the second one, the J-coupling evolution is nulled by selective refocusing of the coupled partner at 4.10 ppm, leaving the lactate doublet in-phase with the other resonances. Subtraction of these spectra results in an upright lactate peak without overlapping resonances. This technique was further refined to reduce the contamination by the co-edited MM through addition of an inversion recovery (IR) sequence (MM nulling) before the J-difference editing [17]. The use of a highly selective editing pulse in the MEGA-sLASER sequence was shown to be more effective for the detection of lactate than the combination of MEGA-sLASER with MM nulling. Nevertheless, subtraction-based methods are prone to motion-induced artefacts that can result in an incorrect determination of the lactate concentration. Moreover, the efficiency of the MEGA editing is also prone to miscalibration. Given that the metabolic changes during neuronal stimulation are relatively small, a proper determination of the resonances of interest is imperative to ensure a correct characterisation of the metabolic time courses. Therefore, the aim of this work was to accurately determine the changes in lactate during visual stimulation, with an optimised J-modulation selection using the sLASER [18] sequence, which is

commonly employed in ultra high-field studies and less susceptible to magnetic resonance (MR) system instabilities and subject motion. No previous fMRS studies have investigated the metabolic fluctuations using a prolonged visual stimulus. Potentially, this could lead to a deeper understanding of the transient/sustained changes in the concentration of key metabolites and their role during neuronal activation. Besides lactate, the analysis of the temporal changes in glutamate concentration is also of interest, since it is an indirect product of oxidative metabolism. Therefore, in this work, lactate and glutamate response patterns were explored during a 15-minute visual stimulus.

5.2 Methods

5.2.1 MR measurements

Six healthy volunteers (3 males; age range: 25 - 30 years old) participated in this study and gave informed consent to a protocol approved by the local ethics committee. MR measurements were performed on a 7 T Philips Achieva MR system (Philips Healthcare, Best, Netherlands) with a 32-channel receive head coil (Nova Medical, Wilmington, Massachusetts, USA) and a volume transmit coil (Nova Medical) with a maximum transmit B_1 field of 20 μT.

Prior to the fMRS measurements, a functional MR imaging (fMRI) localiser (multi-slice echo-planar imaging - EPI, repetition time - TR/TE = 2000/25 ms, spatial resolution = 2x2x3 mm^3, 30 slices) was acquired for assessment of the neuronal activity, through measurement of the blood oxygenation level–dependent (BOLD) effect. The activation paradigm consisted of 8 seconds of a radial checkerboard that reversed its contrast between white and black at 8 Hz, followed by 24 seconds of rest with a total of 6 repeats. Real-time analysis of the fMRI data was performed using IViewBOLD package (Philips Healthcare) integrated in the scanner console to assist the positioning of the spectroscopic volume-of-interest (VOI) within the activated visual cortex. High-resolution anatomical images (magnetisation-prepared rapid gradient-echo - MPRAGE, TR/TE = 7/3 ms, 1 mm^3 of isotropic resolution) were acquired to confirm the voxel position, ensuring that the VOI (20x30x20 mm^3) of water and lactate (1.31 ppm) resonances were

entirely within the visual cortex.

The fMRS measurements were performed with the same visual stimulus as mentioned previously for fMRI, with a paradigm which involved 15 minutes of stimulation (ON period), preceded and followed by 5 minutes of rest with gray background (OFF periods). The ON period consisted of 8 Hz flashing checkerboard stimulation blocks (50 seconds) interleaved with short resting blocks (10 seconds), in order to minimise adaptation and decrease inattention of the subjects. In addition, the subjects were asked to participate in an activity, which consisted of evaluating the colour of the fixation cross in the centre of the field of view and responding through a button press according to previous instructions, to further increase engagement to the task.

^{1}H spectra were acquired during the application of the paradigm for a total of 25 minutes with a sLASER sequence (TR/TE = 5000/144 ms). This sequence consisted of an adiabatic pulse with a bandwidth of 5372 Hz for excitation and two pairs of adiabatic full passage pulses (AFP) with bandwidths of 5424 Hz for refocusing. Water suppression was performed with the variable pulse powers and optimised relaxation delays (VAPOR) [19] scheme and unsuppressed water spectra were also acquired before each scan. A second-order pencil-beam volume shimming, a Philips routine based on fast, automatic shimming technique by mapping along projections (FASTMAP) [20], was applied to cover both water and lactate VOIs. To minimise contamination from extra-cerebral lipid signals, a regional suppression technique was applied, by placing two saturation slabs onto the subjects' scalp (see subsection 3.3.1.3 for more information).

To evaluate the contribution of the MM to the spectra at TE = 144 ms, metabolite-nulled spectra were acquired from a voxel with the same dimensions as previously described placed in the visual cortex of one of the subjects with the sLASER sequence (TR/TE = 5000/144 ms, 64 scans) using an IR technique. To determine the inversion time (TI) that corresponds to the most effective metabolite-nulling, the recovery of the longitudinal magnetisation during the IR experiment, consisting of a sLASER sequence preceded by an inversion pulse (Figure 5.1a), was simulated. The simulated curve has the form of Eq. 2.34, where the inversion factor α is calculated based on the evolution of the longitudinal magnetisation

between the acquisition step of the sLASER sequence and the following inversion pulse:

$$1 - \alpha \; = - \left[1 - \exp\left(- \frac{TR - TI}{T_1} \right) \right]. \tag{5.1}$$

Solving for α, we obtain:

$$\alpha = 2 - \exp\left(- \frac{TR - TI}{T_1} \right). \tag{5.2}$$

Substituting Eq. 5.2 onto Eq. 2.34, the recovery of the longitudinal magnetisation following the inversion pulse is given as:

$$M_z = \left\{ 1 - \left[2 - \exp\left(- \frac{TR - TI}{T_1} \right) \right] \exp\left(- \frac{TI}{T_1} \right) \right\} \exp\left(- \frac{TE}{T_2} \right), \tag{5.3}$$

where the T_2 relaxation effects were also included. The simulation was performed for the creatine signal at 3.02 ppm. Considering TR = 5000 ms, T_1 = 1760 ms [21] and T_2 = 107 ms [22], the optimum TI for the cancellation of the creatine peak is 1120 ms (blue trace in Figure 5.1b). Since the T_1s of metabolites are longer than the T_1s of MM [23], spectra obtained with TIs close to the optimal TI for creatine nulling will show a progressive change in the amplitude of the metabolites'

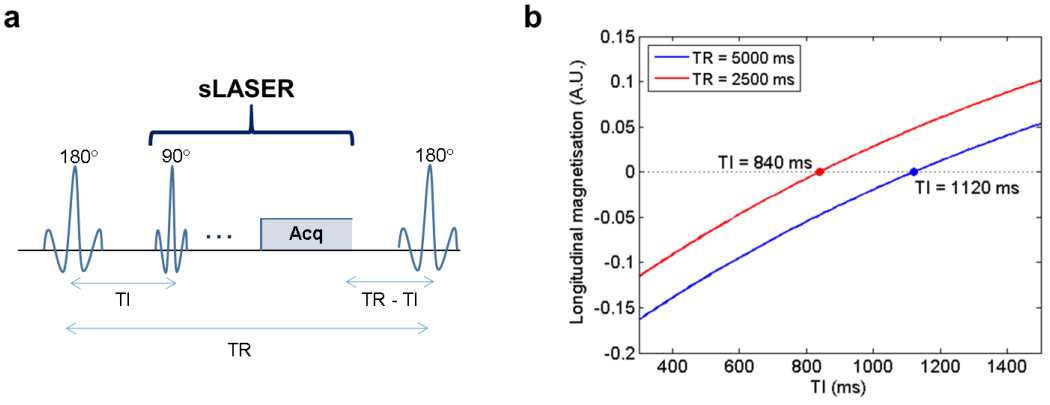


Figure 5.1: Calculation of the optimum TI for the cancellation of the creatine signal at 3.02 ppm in an IR experiment, consisting of a sLASER sequence preceded by an inversion pulse (a). The curves in b) show the recovery of the longitudinal magnetisation as a function of TI (Eq. 5.3). The creatine signal is nulled at TI = 1120 ms for a TR = 5000 ms (blue trace). Shorter TRs result in a reduced amount of inverted magnetisation, and thus shorter TIs for the nulling of the same metabolite (red trace). The curves were simulated considering a T_1 and T_2 of creatine of 1760 and 107 ms, respectively.

peaks with a phase inversion, while the MM will remain almost unchanged. This will allow the MM to be distinguished from the metabolites. Therefore, four IR spectra were acquired with TIs of 800, 900, 1000 and 1100 ms. Water suppression was achieved using the multiply optimised insensitive suppression train (MOIST) [24, 25] technique, as the VAPOR option was not compatible with the pre-existing IR module in the Philips pulse programming environment. One additional scan without IR was also performed.

5.2.2 Data processing

The fMRS data acquired independently from the 32 channels were reconstructed based on an optimised coil combination method [26] and frequency aligned using the creatine peak at 3.02 ppm in MATLAB (Mathworks, Natick, Massachusetts, USA). Then for each subject, spectra were averaged into blocks of 20 scans, followed by a moving average with a kernel of 3 blocks, resulting in nine spectra for further quantification (60 averages each). Only averages fully composed of blocks from either the ON or OFF period were kept, to avoid a mixture of signals acquired in different conditions.

All spectra were checked for potential artefacts, lipid contamination or poor shimming. The water linewidth was obtained by calculating the full width at half maximum of the Lorentzian-fitted water peak from the unsuppressed water spectra of each subject. The SNR of the creatine peak at 3.02 ppm was calculated as the ratio of the amplitude of the Lorentzian-fitted creatine peak to the standard deviation of noise (spectral region without resonances) for each individual subject time point.

For group analysis, spectra were averaged across subjects after frequency alignment using the creatine peak, resulting in a time series with the same temporal resolution as previously, with each time point corresponding to a total of 360 averages (6 subjects x 60 averages).

All spectra were quantified using LCModel [27], with a basis set composed of 19 metabolites, simulated using Versatile Simulation, Pulses, and Analysis (VESPA) [28] software: aspartate, choline, creatine, gamma-aminobutyric acid (GABA), glucose, glutamate, glutamine, glutathione, glycerophosphocholine, glycine, lac-

tate, myo-inositol, N-acetylaspartate (NAA), N-acetylaspartylglutamate, phosphocholine, phosphocreatine, phosphorylethanolamine, scyllo-inositol and taurine. The methyl group of NAA, creatine and phosphocreatine was added to the basis set separately from the methylene group, to take into account their different transverse relaxation times [22]. All pulses in the sLASER sequence were simulated as block pulses with interpulse timings of 6, 8, 8, and 64 ms.

By visual inspection of the measured IR spectra (Figure 5.2), the residual MM resonances were identified, which consist of MM1 (0.89 ppm), MM2 (1.20 ppm) and MM3 (1.37 ppm). These MM resonances were simulated in MATLAB as Lorentzian peaks of 3 Hz linewidth, to match the linewidth of the simulated metabolic peaks, and then included in the basis set.

LCModel analysis was performed over the spectral range from 0.2 to 4.2 ppm, with the node spacing of the spline function for baseline fitting (parameter dkntmn) set to 4 ppm, to ensure a flat baseline, as the majority of the MM and lipid signals are fully relaxed at TE = 144 ms, which can be confirmed in Figure 5.2. Allowing multiple degrees of freedom in the baseline spline fit of LCModel may cause these MM resonances to be erroneously considered as part of a wild baseline. This can lead to a readjusting of the baseline fitting in other parts of the spectrum, and consequently to the under/overestimation of the resonances of interest. No additional MM or lipids resonances simulated by LCModel were added to the analysis.

Statistical analysis was performed using a two-tailed t-test on the percentage change relative to the first OFF period (baseline) in the individual subject metabolite time courses.

Off-line analysis of the multi-slice EPI data was performed with the statistical parametric mapping (SPM8) software package (University College London, London, United Kingdom). The data were motion-corrected using the first image as a reference and resliced after alignment, such that the following images matched the first. No spatial smoothing was applied to the data. Statistical parametric maps (p-value < 0.05) of activation versus baseline were generated by means of a general linear model [29]. The spatial coordinates of the MRS voxel were used to determined the shifted VOIs for the lactate resonance at 1.31 ppm and glutamate resonances at 2.08, 2.35, 3.74 ppm, allowing the generation of four distinct VOI

masks. These masks were superimposed onto the parametric maps to obtain the overall BOLD signal within the spectroscopic voxels. Finally, the mean BOLD signal across each voxel, obtained by dividing the BOLD signal by the number of signal-contributing pixels, was tested for significant correlation with the maximum percentage change of lactate and glutamate concentrations during visual stimulation, obtained through analysis of the fMRS data. The BOLD signals obtained for each glutamate resonance shifted MRS voxel were averaged to yield a single BOLD value for the glutamate detection volume.

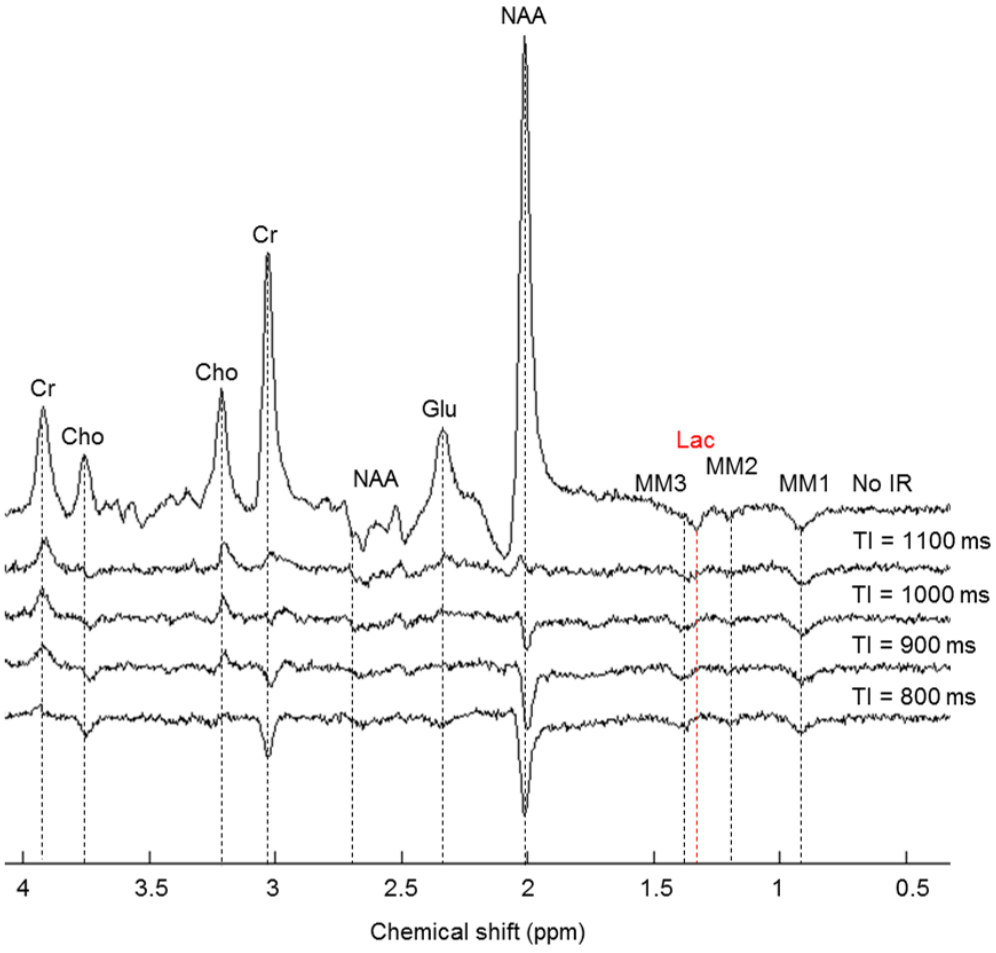


Figure 5.2: Spectra measured with the IR technique, with TIs of 800, 900, 1000 and 1100 ms. An additional spectrum without IR was also acquired. Spectra were measured with a sLASER sequence (TR/TE = 5000/144 ms, 64 scans) from a 20x30x20 mm^3 voxel placed in the visual cortex. Residuals from the metabolite-nulling technique are visible in the IR spectra, as well as non-nulled MM resonances, MM1, MM2 and MM3. The phase of the creatine (Cr) peak at 3.02 ppm changes from negative to positive between TI = 1000 ms and TI = 1100 ms, thus placing the optimal TI for creatine cancellation close to the one obtained through simulation (1120 ms). Cho - choline, Glu - glutamate, Lac - lactate.

5.3 Results

The mean water linewidth in the VOI was 11.4±1.0 Hz and the SNR of the creatine peak during the paradigm was 52.2±5.7, for all individual subject time points (9 time points x 6 subjects). Figure 5.3 shows the individual subject spectra summed over the paradigm time course. There is a good agreement between all subjects' spectra with no indication of lipid contamination. Additionally, glutamate and lactate levels were estimated in LCModel with Cramér–Rao lower bounds (CRLBs) of $\sim$ 2% and $\sim$ 8%, respectively (based on 6 subjects' data - individual subject spectra with 60 averages). This demonstrates the efficacy of the data acquisition and post-processing methods, with no spectrum having to be discarded. The simulated basis set with the addition of the relevant MM resonances exhibited a good agreement with the individual spectra, resulting in a well-fitted inverted lactate peak (Figure 5.4).

Glutamate, lactate, NAA and total creatine time courses for individual subjects

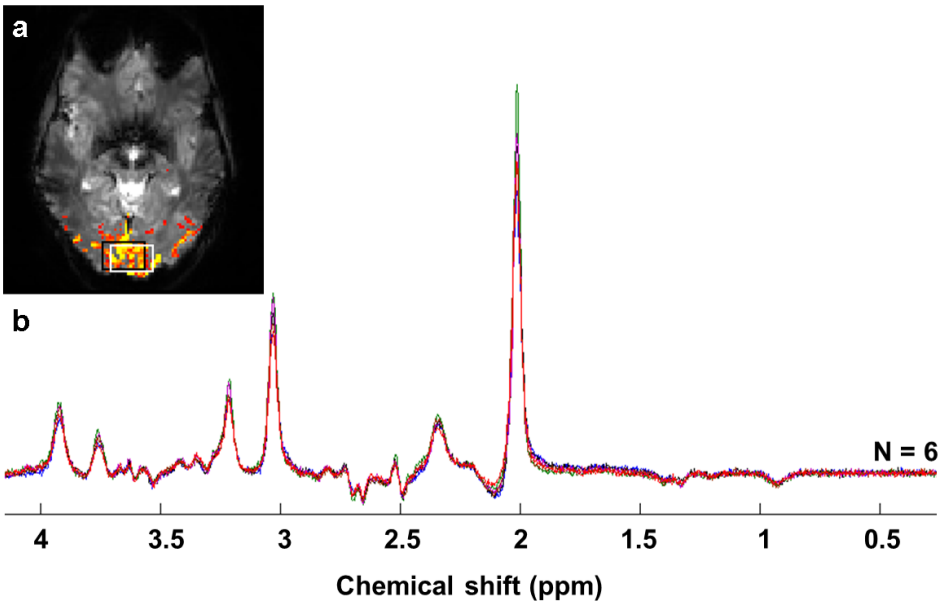


Figure 5.3: Individual subject spectra (N = 6) acquired during the applied paradigm and summed over the entirety of the time course (540 averages for each spectrum). Spectra (b) were measured with a sLASER sequence (TR/TE = 5000/144 ms) from a region of strong activation assessed through an fMRI acquisition. The representative BOLD response (a) shows the voxel position (20x30x20 mm^3) in the activated visual cortex - lactate VOI (black box) is chemically shifted from the water VOI (white box).

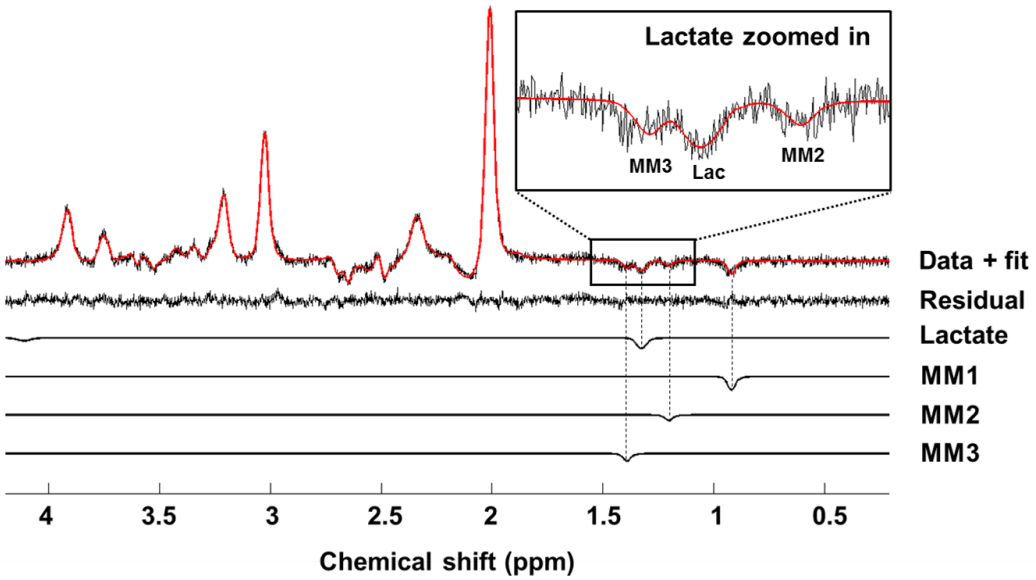


Figure 5.4: Example of an individual subject spectrum (sLASER, TR/TE = 5000/144 ms, voxel size = 20x30x20 mm^3, averages = 60), related to one time point of the time course analysis, and corresponding LCModel fits for lactate and macromolecules MM1, MM2 and MM3. A flat residual between the data and LCModel fit was consistently obtained.

are shown in Figure 5.5. Detection of a trend in the metabolic temporal changes is challenging, due to the wide range of amplitudes amongst different subjects' data. Therefore, the quantitative changes in metabolic levels were measured based on the percentage change relative to the baseline. In Figure 5.6, mean changes based on the concentration during the first OFF period of the paradigm are depicted. Significant increases (p-value < 0.05) in glutamate levels of 2.6±0.7% and 2.5±0.9% were observed as an immediate response to the stimulus, as well as a rise in lactate levels of 10.4±4.4% reached halfway through the stimulation. However, no statistically significant changes in NAA and total creatine levels were observed during the stimulation, as expected for these molecules. The analysis of the group spectra confirmed lactate and glutamate response pattern obtained with the individual subject analysis (Figure 5.7).

No significant correlation was found between lactate and glutamate changes during visual stimulation and the BOLD signal from the respective VOIs (data not shown).

5.4 Discussion

The role of lactate in brain activation, and thus the relevance of the oxidative and non-oxidative metabolic pathways in that condition, still remains unclear. Therefore, a proper quantification of the key metabolites involved in these processes is fundamental, in order to elucidate the main mechanisms underlying neuronal stimulation. This has previously proved challenging, especially for lactate, whose signal is strongly contaminated by MM and lipids; this contamination is particularly worsened when the selected VOI is in a region adjacent to pericranial fat, as in the case of the occipital cortex in fMRS studies with visual stimulation. In this work, we minimised the overlapping signals of MM and lipids by using a long TE sLASER sequence in combination with saturation slabs. The remaining MM signals were identified through visual inspection of metabolite-nulled spectra, and

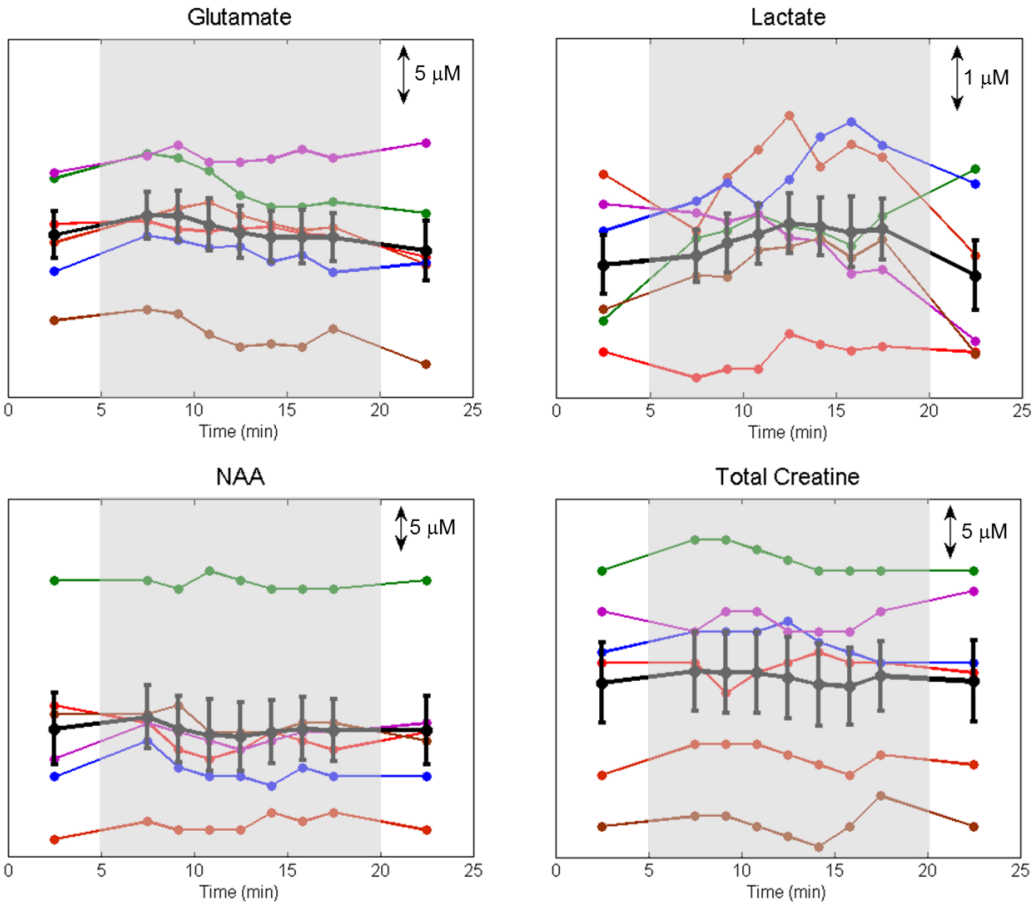


Figure 5.5: Individual subject time courses for glutamate, lactate, NAA and total creatine and respective mean (black trace). Error bars represent standard error of the mean. Shaded areas correspond to the ON period of the paradigm.

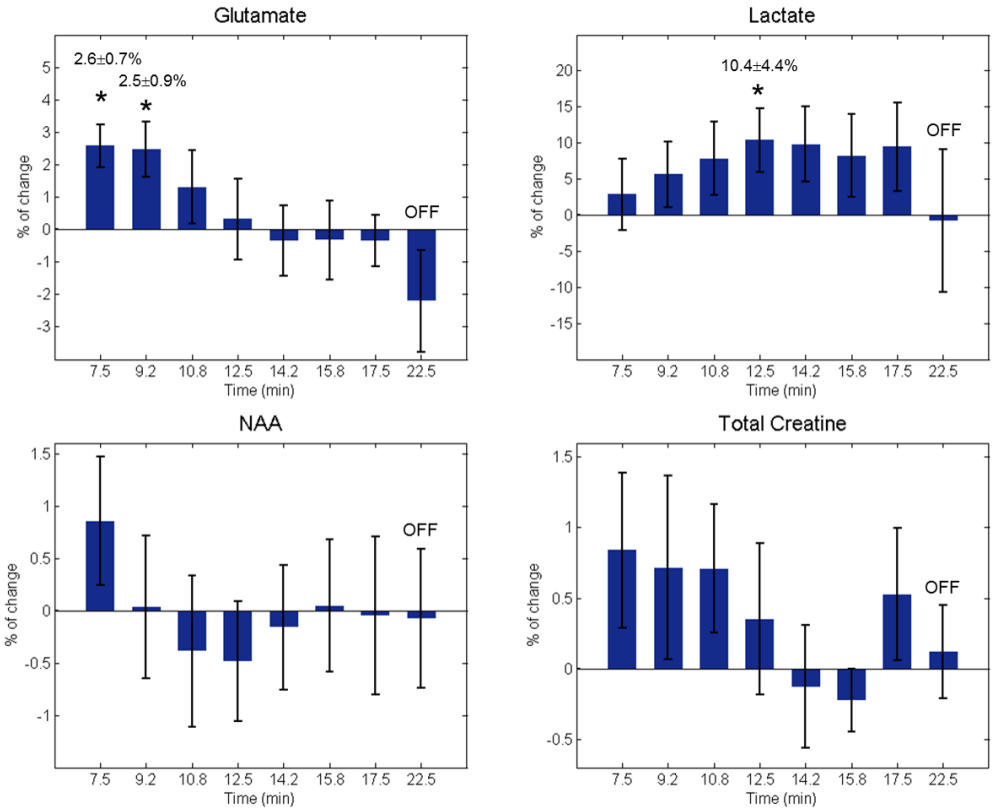


Figure 5.6: Mean percentage change relative to the metabolite concentration in the first OFF period calculated from the individual subject spectra for glutamate, lactate, NAA and total creatine. * indicates a significant difference (p-value < 0.05). Error bars represent standard error of the mean.

were then individually fitted with simulated Lorentzian peaks.

A long TE sLASER sequence has been used for lactate detection in a previous fMRS study [11]. However, at TE = 144 ms, a non-negligible amount of MM signal is still present in the spectral regions adjacent to lactate and needs to be carefully characterised. The study described here differed from the preceding one by not including a general measured MM profile into the basis set. Since the remaining MM could be clearly identified in the metabolite-nulled spectra, it was possible to simulate their contribution. The addition of individual simulated components allows the variability in each component to be adequately accounted for.

The results from this study showed highly reproducible spectra obtained from different subjects (N = 6), with no manifestation of artefacts or lipid contamination. The CRLBs of glutamate and lactate were lower than the ones reported in the previous fMRS study which also used a long TE sLASER sequence; lactate in par-

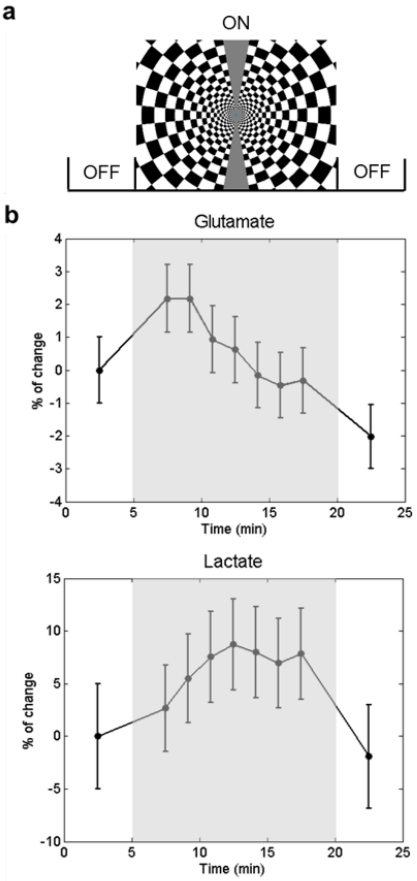


Figure 5.7: glutamate and lactate time courses (b) during a paradigm, which consisted of 15 minutes of visual stimulation, preceded and followed by 5 minutes of rest (a). The time courses were calculated on the group-averaged spectra (N = 6) quantified using LCModel. The percentage change was determined based on the concentration during the first OFF period of the paradigm. Error bars represent CRLBs of the spectral fitting.

ticular was more precisely quantified in this study with a CRLB of 8% on average (based on spectra with 60 averages), when compared to 16% (based on spectra with 64 averages). This indicated a good fit of the basis set with the addition of the simulated MM components to the acquired lactate signal, which could be also confirmed by visual inspection of the individual subject spectra.

The analysis of the metabolite time courses based on either individual subject spectra or the group-averaged spectra led to identical trends. The glutamate time course showed an increase in glutamate levels within the first minutes of stimulation, followed by a return to baseline. In contrast, lactate levels gradually increased during the ON period, reaching its maximum in the middle of this period, and maintaining a steady-state until the end of the stimulation. The changes in glutamate and lactate levels proved to be significant when compared to the first OFF

period of each individual subject time course. These changes agree with previous observations performed at 7 T; the percentage change for glutamate was within the reported range (2% to 5%), as well as for lactate (7% to 37%). However, the application of a prolonged visual stimulus led to additional information about the metabolic response pattern. Glutamate was shown to have an initial transient concentration increase, whereas lactate showed a delayed response to the stimulus, with a rise to a higher concentration plateau sustained until the end of the stimulation.

Results from the previous 7 T fMRS studies have shown significant changes in other metabolites' levels during neuronal activation, such as aspartate [7, 8, 10], glucose [9, 10], glutamine [8], glutathione [8], glycine [8], GABA [12] and phosphorylethanolamine [10]. In this work, the acquisition and analysis methods were optimised for the detection of lactate. NAA, total creatine and glutamate possess a high amplitude signal, and thus could also be accurately quantified. Since the aim of this work was to provide a robust metabolic quantification, only changes in molecules, whose fitting with LCModel had shown to be visibly plausible (regardless of their CRLB) were tested for statistical significance, to avoid the emergence of false positives.

No significant changes in NAA and total creatine levels were detected during visual stimulation, even without linewidth correction, to account for the BOLD effect. Short TE fMRS studies that measure the metabolic changes by means of a difference spectrum (ON - OFF period) require the application of a line broadening filter to the spectra, in order to compensate for the small line narrowing effect caused by the BOLD-related T_2^* changes during neuronal activation [30]. In this study, the lactate peak was shown to be easily identifiable, hence eliminating the need of employing difference or linewidth matching methods.

Finally, no correlation was found between the BOLD response and the concentration changes of lactate and glutamate during stimulation. Bednařík at al. [10] reported that the BOLD-fMRI amplitudes significantly and positively correlate with the relative glutamate and lactate levels changes. The lack of correlation in this study might be due to a reduced sample size.

In conclusion, the presented acquisition and analysis strategies focused on lac-

tate quantification were shown to provide a reliable way to detect changes in the concentration of this metabolite, as well as glutamate, during visual stimulation. The use of a longer stimulation period showed a different behaviour of lactate and glutamate, respectively downstream products of non-oxidative and oxidative metabolism of glucose, achieving statistical significance even with a small sample size. It is expected that the application of this protocol to a larger sample size will enable further interpretation of the dynamics of brain metabolism, by modelling of the metabolic time courses.

Bibliography

[1] Peter T Fox, Marcus E Raichle, Mark A Mintun, and Carmen Dence. Nonoxidative glucose consumption during focal physiologic neural activity. *Science*, 241(4864):462, 1988.

[2] James Prichard, Douglas Rothman, Edward Novotny, Ognen Petroff, Takeo Kuwabara, Malcolm Avison, Alistair Howseman, Christopher Hanstock, and Robert Shulman. Lactate rise detected by ^{1}H NMR in human visual cortex during physiologic stimulation. *Proceedings of the National Academy of Sciences*, 88(13):5829–5831, 1991.

[3] Luc Pellerin and Pierre J Magistretti. Glutamate uptake into astrocytes stimulates aerobic glycolysis: a mechanism coupling neuronal activity to glucose utilization. *Proceedings of the National Academy of Sciences*, 91(22):10625–10629, 1994.

[4] Jens Frahm, Gunnar Krüger, Klaus-Dietmar Merboldt, and Andreas Kleinschmidt. Dynamic uncoupling and recoupling of perfusion and oxidative metabolism during focal brain activation in man. *Magnetic resonance in medicine*, 35(2):143–148, 1996.

[5] D Sappey-Marinier, G Calabrese, G Fein, JW Hugg, C Biggins, and MW Weiner. Effect of photic stimulation on human visual cortex lactate and phosphates using ^{1}H and ^{31}P magnetic resonance spectroscopy. *Journal of Cerebral Blood Flow & Metabolism*, 12(4):584–592, 1992.

[6] Klaus-Dietmar Merboldt, Harald Bruhn, Wolfgang Hanicke, Thomas Michaelis, and Jens Frahm. Decrease of glucose in the human visual cortex during photic stimulation. *Magnetic resonance in medicine*, 25(1):187–194, 1992.

[7] Silvia Mangia, Ivan Tkáč, Rolf Gruetter, Pierre-Francois Van de Moortele, Bruno Maraviglia, and Kâmil Uğurbil. Sustained neuronal activation raises oxidative metabolism to a new steady-state level: evidence from ^{1}H NMR spectroscopy in the human visual cortex. *Journal of Cerebral Blood Flow & Metabolism*, 27(5):1055–1063, 2007.

[8] Yan Lin, Mary C Stephenson, Lijing Xin, Antonio Napolitano, and Peter G Morris. Investigating the metabolic changes due to visual stimulation using functional proton magnetic resonance spectroscopy at 7T. *Journal of cerebral blood flow & metabolism*, 32(8):1484–1495, 2012.

[9] Benoît Schaller, Ralf Mekle, Lijing Xin, Nicolas Kunz, and Rolf Gruetter. Net increase of lactate and glutamate concentration in activated human visual cortex detected with magnetic resonance spectroscopy at 7 Tesla. *Journal of neuroscience research*, 91(8):1076–1083, 2013.

[10] Petr Bednařík, Ivan Tkáč, Federico Giove, Mauro DiNuzzo, Dinesh K Deelchand, Uzay E Emir, Lynn E Eberly, and Silvia Mangia. Neurochemical and BOLD responses during neuronal activation measured in the human visual cortex at 7 Tesla. *Journal of Cerebral Blood Flow & Metabolism*, 35(4):601–610, 2015.

[11] Petr Bednařík, Ivan Tkáč, Dinesh Deelchand, Felipe Barreto, Lynn E. Eberly, Shalom Michaeli, and Silvia Mangia. Functional MRS at 7T and long TE. In *Proceedings of the International Society for Magnetic Resonance in Medicine, 24th Scientific Meeting and Exhibition*, page 3351, 2016.

[12] Ralf Mekle, Simone Kühn, Harald Pfeiffer, Semiha Aydin, Florian Schubert, and Bernd Ittermann. Detection of metabolite changes in response to a varying visual stimulation paradigm using short-TE ^{1}H MRS at 7T. *NMR in Biomedicine*, 30(2):e3672, 2017.

[13] Benoît Schaller, Lijing Xin, and Rolf Gruetter. Is the macromolecule signal tissue-specific in healthy human brain? A ^{1}H MRS study at 7 Tesla in the occipital lobe. *Magnetic resonance in medicine*, 72(4):934–940, 2014.

[14] Vincent O Boer, Peter R Luijten, and Dennis WJ Klomp. Refocused double-quantum editing for lactate detection at 7T. *Magnetic resonance in medicine*, 69(1):1–6, 2013.

[15] CS Arteaga de Castro, VO Boer, A Andreychenko, JP Wijnen, UA Heide, PR Luijten, and DWJ Klomp. Improved efficiency on editing MRS of lactate and γ-aminobutyric acid by inclusion of frequency offset corrected inversion pulses at high fields. *NMR in Biomedicine*, 26(10):1213–1219, 2013.

[16] Chen Chen, Peter Morris, Susan Francis, and Penny Gowland. *In Vivo* Detection of Lactate at 7T Using Long TE SLASER and MEGA-SLASER. In *Proceedings of the International Society for Magnetic Resonance in Medicine, 23rd Scientific Meeting and Exhibition*, page 4693, 2015.

[17] JP Wijnen, J Haarsma, VO Boer, PR Luijten, S Stigchel, SFW Neggers, and DWJ Klomp. Detection of lactate in the striatum without contamination of macromolecules by J-difference editing MRS at 7T. *NMR in Biomedicine*, 28(4):514–522, 2015.

[18] Tom WJ Scheenen, Dennis WJ Klomp, Jannie P Wijnen, and Arend Heerschap. Short echo time ^{1}H-MRSI of the human brain at 3T with minimal chemical shift displacement errors using adiabatic refocusing pulses. *Magnetic resonance in medicine*, 59(1):1–6, 2008.

[19] I Tkáč, Z Starčuk, I-Y Choi, and R Gruetter. In vivo ^{1}H NMR spectroscopy of rat brain at 1ms echo time. *Magnetic resonance in medicine*, 41:649–656, 1999.

[20] Rolf Gruetter. Automatic, localized in vivo adjustment of all first-and second-order shim coils. *Magnetic resonance in medicine*, 29(6):804–811, 1993.

[21] Lijing Xin, Benoît Schaller, Vladimir Mlynarik, Huanxiang Lu, and Rolf Gruetter. Proton T_1 relaxation times of metabolites in human occipital white and gray matter at 7T. *Magnetic resonance in medicine*, 69(4):931–936, 2013.

[22] Małgorzata Marjańska, Edward J Auerbach, Romain Valabrègue, Van de Moortele, Gregor Adriany, Michael Garwood, et al. Localized ^{1}H NMR spectroscopy in different regions of human brain in vivo at 7T: T_2 relaxation times and concentrations of cerebral metabolites. *NMR in Biomedicine*, 25(2):332–339, 2012.

[23] Alfredo L Lopez-Kolkovsky, Sebastien Mériaux, and Fawzi Boumezbeur. Metabolite and macromolecule T_1 and T_2 relaxation times in the rat brain in vivo at 17.2T. *Magnetic resonance in medicine*, 75(2):503–514, 2016.

[24] JB Murdoch and DA Lampman. Beyond WET and DRY: optimized pulses for water suppression. In *Proceedings of the Society of Magnetic Resonance in Medicine, 12th Meeting*, page 1191, 1993.

[25] K Kaminska, Jerzy Walecki, Paweł Grieb, and Piotr Bogorodzki. Magnetic resonance spectroscopy - state of art and future. *Polish Journal of Radiology*, 72(1):71–75, 2007.

[26] Emma L Hall, Mary C Stephenson, Darren Price, and Peter G Morris. Methodology for improved detection of low concentration metabolites in MRS: optimised combination of signals from multi-element coil arrays. *Neuroimage*, 86:35–42, 2014.

[27] Stephen W Provencher. Estimation of metabolite concentrations from localized in vivo proton NMR spectra. *Magnetic resonance in medicine*, 30(6):672–679, 1993.

[28] BJ Soher, P Semanchuk, D Todd, J Steinberg, and K Young. VESPA: Integrated applications for RF pulse design, spectral simulation and MRS data analysis. In *Proceedings of the International Society for Magnetic Resonance in Medicine, 19th Scientific Meeting and Exhibition*, page 1410, 2011.

[29] Jean-Baptiste Poline and Matthew Brett. The general linear model and fMRI: does love last forever? *Neuroimage*, 62(2):871–880, 2012.

[30] Xiao-Hong Zhu and Wei Chen. Observed BOLD effects on cerebral metabolite resonances in human visual cortex during visual stimulation: a functional ^{1}H MRS study at 4T. *Magnetic resonance in medicine*, 46(5):841–847, 2001.

Chapter 6

In vivo ^{1}H-localised ^{13}C MRS for deep human brain applications

6.1 Introduction

Changes in the brain's energy metabolism can reflect abnormal neuronal activity and be indicative of neurological and psychiatric syndromes. Positron emission tomography (PET) has been used to assess regional glucose metabolism in the human brain by tracing the injected glucose analogue, 2-fluoro-2-deoxy-D-glucose (FDG), through part of the glycolytic pathway. However, FDG is phosphorylated to FDG-6-PO_4, which is not a substrate for further metabolism, thus accumulating in the tissue and not being able to provide information on downstream metabolic fluxes. Additionally, PET suffers from lack of chemical specificity, as it cannot distinguish between the signal yielded from glucose itself and the one from glucose products. On the other hand, ^{13}C magnetic resonance spectroscopy (MRS) uses non-radioactive tracers to detect and distinguish signal from all metabolites with sufficient concentration involved in glucose metabolism.

Most ^{13}C MRS brain studies use [1-^{13}C]glucose as a tracer, since the ^{13}C label in the first carbon is processed in several consecutive tricarboxylic acid (TCA) cycles, as opposed to other substrates, whose label is lost faster. The feasibility of this technique relies on the transfer of the ^{13}C label to the metabolites involved in energy production and neurotransmitter cycling, such as glutamate and glutamine. As can be seen in Figure 3.5, the neurotransmitter glutamate is one of the products of the TCA cycle and is replenished through the glutamate-glutamine cycle. The ^{13}C label, initially present in the first carbon of the glucose molecule

(GlcC1), is transferred to the fourth carbon of glutamate (GluC4) and glutamine (GlnC4), in the first turn of the TCA cycle. In the second turn of the TCA cycle, the ^{13}C label is equally distributed between the position 2 and 3 in glutamate (GluC2 and GluC3) and glutamine (GlnC2 and GlnC3). This is only valid if other reactions are neglected, in particular the pyruvate carboxylase reaction, which is involved in the *de novo* synthesis of TCA cycle intermediates and downstream glutamate-glutamine in the astrocytes. The quantification of these distinct resonances combined with mathematical modelling of glucose metabolism allows the determination of the TCA cycle rate, providing a measure of neuroenergetics, as well as the glutamate-glutamine cycle rate, for assessing neurotransmission.

The choice of acquisition method for ^{13}C MRS studies is dependent on the amount of chemical information (number of resonances) one desires to obtain, as well as on the MR system capabilities. These methods can either directly detect the ^{13}C signal or indirectly provide a measurement of the ^{13}C fraction by detecting the protons attached to ^{13}C and ^{12}C nuclei. While indirect ^{1}H-[^{13}C] MRS methods are associated with an increased sensitivity compared to direct ^{13}C MRS, ^{1}H spectra have a chemical shift dispersion for the resonances of interest of less than 5 ppm. Since the number and accuracy of determined metabolic rates depend on the correct separation of glutamate and glutamine resonances, direct ^{13}C MRS becomes a more attractive option [1].

For direct ^{13}C signal detection, two major techniques can be distinguished: polarisation transfer and direct excitation. Polarisation transfer from neighbouring hydrogen nuclei allows an enhancement in the sensitivity of the ^{13}C signal of up to 4 times when compared to direct excitation. However, the signal enhancement depends on the choice of echo time (TE), which is set to the inverse of the J-coupling constant of the spin system, thus favouring the detection of spin systems with small scalar couplings with direct excitation (GluC1, GlnC1, GluC5 and GlnC5 obtained with [2-^{13}C]glucose infusion). Similarly, direct ^{13}C excitation is more suitable for the detection of metabolites with short T_2 relaxation times (e.g. glycogen), as the signal is acquired immediately after excitation. Polarisation transfer techniques are mainly chosen for detection of the resonances associated with the positions 2, 3 and 4 in glutamate and glutamine.

Most ^{13}C studies have been performed with surface coils, ensuring high radiofrequency (RF) efficiency and receive sensitivity [1]. However, surface coils suffer from inhomogeneous B_1, which can lead to inaccurate flip angles and thus signal loss. To overcome this, adiabatic RF pulses, such as the B_1 insensitive rotation (BIR) pulses [2], can be used to ensure a constant flip angle insensitive to B_1 field variations. Nevertheless, the reduction of the sensitivity in surface coil reception when the distance from the coil to the sample progressively increases still remains an issue, making challenging the acquisition of signal from deep brain structures. Therefore, *in vivo* human ^{13}C studies have been focused on the occipital region [3].

The work by Li et al. [3] describes the acquisition of ^{13}C signal from the frontal lobe, using a ^{1}H birdcage coil to increase the decoupling efficiency, as also described previously [4, 5]. Nonetheless, the sensitivity in the ^{13}C channel has not been optimised for deep brain regions as a surface coil was used for signal detection.

In this study, a ^{1}H-^{13}C birdcage coil was used to acquire ^{13}C spectra from the anterior cingulate cortex (ACC) in the human brain at 7 T. This is the first study that describes the feasibility of detecting the ^{13}C resonances in the positions 3 and 4 in glutamate and glutamine at 7 T from a deep brain structure of the human brain. A previous ^{13}C MRS study at 7 T has only explored the detection of the ^{13}C signal in the position 1 and 5 in glutamate and glutamine from the occipital lobe [6].

6.2 Methods

6.2.1 Sequence design

In this work, the polarisation transfer method, distortionless enhancement by polarisation transfer (DEPT) [7], was combined with 3D image selected *in vivo* spectroscopy (ISIS) [8] for signal localisation. Here, the acquisition is performed in the ^{13}C channel, while the ^{1}H channel is used for coherence transfer, spatial localisation, shimming steps and acquisition of localiser images.

DEPT is a method widely used for acquiring multiple ^{13}C resonances, and can

be employed to edit the ^{13}C signal into subspectra containing only the CH, CH_2 and CH_3 groups or spectra showing all the groups with optimised parameters for a specific group [9]. The polarisation transfer mechanism is similar to the one in the insensitive nuclei enhanced by polarisation transfer (INEPT) experiment [10], with the difference that the magnetisation from the ^{13}C nuclei multiplets is in phase at the end of the pulse sequence without the need for an extra refocusing delay.

The quantum coherence pathways in the DEPT sequence (Figure 6.1) can be described through the product operator formalism [11]. Let the ^{1}H magnetisation be represented by the H spins with an initial polarisation of P_H and the ^{13}C magnetisation by the C spins with an initial polarisation of P_C. The ^{1}H magnetisation, which is initially in the longitudinal axis, is transformed into transverse magnetisation and will undergo chemical shift (Ω) and J-coupling evolution during τ $(1/2J)$:

$$P_H 2H_{1x}C_z cos\left(\Omega_H \tau\right) + P_H 2H_{1y}C_z sin\left(\Omega_H \tau\right). \tag{6.1}$$

Next, the 180° pulse in the ^{1}H channel is applied simultaneously with a 90° pulse in the ^{13}C channel, which tips the ^{13}C magnetisation into the transverse plane,

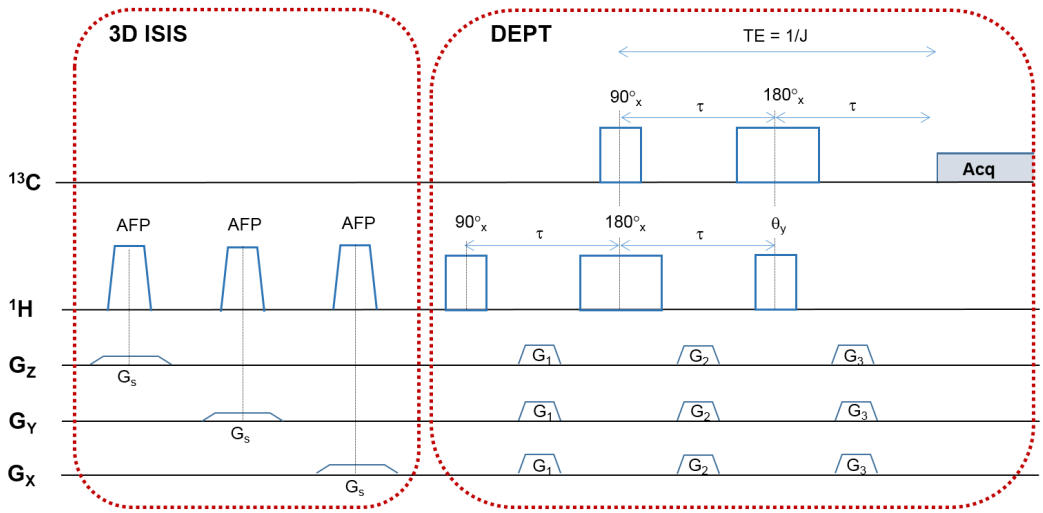


Figure 6.1: Schematic diagram of the ISIS-DEPT sequence. 3D ISIS localisation is performed on the ^{1}H channel with adiabatic full passage (AFP) pulses and slice selection gradients G_s applied concurrently. The DEPT sequence uses both channels for polarisation transfer, which occurs when TE equals $1/J_{CH}$. Crusher gradients G_1, G_2 and G_3 are applied in the first, second and third τ periods. θ is the flip angle of the last ^{1}H pulse.

creating zero-quantum and double-quantum coherences. These will evolve under the influence of H and C chemical shifts during the second τ interval:

$$-P_H 2H_{1x}C_y cos\left(\Omega_C \tau\right) + P_H 2H_{1x}C_x sin\left(\Omega_C \tau\right). \tag{6.2}$$

Note that the ^{1}H chemical shift has been refocused, but not the one of ^{13}C. Also, there is no longitudinal magnetisation for either of the spins, thus the coherences will not undergo J-coupling evolution under J_{H1C}; however the coherences will couple with the z component of H_2 and H_3 and will evolve under J_{H2C} and J_{H3C}. Depending on whether we want to describe the CH, CH_2 or CH_3 groups, the spin states after the second τ interval are:

$$\begin{aligned}
\text{CH} &\Rightarrow -P_H 2H_{1x}C_y cos\left(\Omega_C \tau\right) + P_H 2H_{1x}C_x sin\left(\Omega_C \tau\right) \\
\text{CH}_2 &\Rightarrow P_H 4H_{1x}H_{2z}C_x cos\left(\Omega_C \tau\right) + P_H 4H_{1x}H_{2z}C_y sin\left(\Omega_C \tau\right) \\
\text{CH}_3 &\Rightarrow P_H 8H_{1x}H_{2z}H_{3z}C_y cos\left(\Omega_C \tau\right) - P_H 8H_{1x}H_{2z}H_{3z}C_x sin\left(\Omega_C \tau\right).
\end{aligned} \tag{6.3}$$

Finally, after the 180° pulse in the ^{13}C channel and the final ^{1}H pulse, the heteronuclear multiple-quantum coherences are transformed into single-quantum coherences:

$$\begin{aligned}
\text{CH} \Rightarrow &- P_H 2H_{1z}C_y cos\left(\Omega_C \tau\right) sin\left(\theta\right) \\
&- P_H 2H_{1z}C_x sin\left(\Omega_C \tau\right) sin\left(\theta\right) \\
\text{CH}_2 \Rightarrow &- P_H 4H_{1z}H_{2z}C_x cos\left(\Omega_C \tau\right) sin\left(\theta\right) cos\left(\theta\right) \\
&+ P_H 4H_{1z}H_{2z}C_y sin\left(\Omega_C \tau\right) sin\left(\theta\right) cos\left(\theta\right) \\
\text{CH}_3 \Rightarrow &+ P_H 8H_{1z}H_{2z}H_{3z}C_y cos\left(\Omega_C \tau\right) sin\left(\theta\right) cos^2\left(\theta\right) \\
&+ P_H 8H_{1z}H_{2z}H_{3z}C_x sin\left(\Omega_C \tau\right) sin\left(\theta\right) cos^2\left(\theta\right).
\end{aligned} \tag{6.4}$$

Following the chemical shift evolution of the ^{13}C spins, which is then refocused, and the J-coupling evolution, the resulting ^{13}C spectrum will contain a combination of the CH, CH_2 or CH_3 resonances with a signal enhancement of $P_H/P_C\ \left(\gamma_H/\gamma_C\right)$,

modulated by the angle θ of the last ^{1}H pulse:

$$\begin{aligned} \mathrm{CH} &\Rightarrow P_H C_x sin\,(\theta) \\ \mathrm{CH_2} &\Rightarrow P_H C_x sin\,(\theta)\, cos\,(\theta) \\ \mathrm{CH_3} &\Rightarrow P_H C_x sin\,(\theta)\, cos^2\,(\theta)\,. \end{aligned} \tag{6.5}$$

The ^{1}H localisation will act on terms derived above, which evolved from the ^{1}H magnetisation with initial polarisation P_H. However, it is also important to follow the operator representing the ^{13}C initial polarisation, which is not arising from coupling with the neighbouring ^{1}H spins and is therefore non-localised. The quantum mechanical description of this coherence pathway is analogous to the one described above; ^{13}C longitudinal magnetisation with initial polarisation P_C will be rotated to the xy plane with the 90° pulse in the ^{13}C channel and will undergo chemical shift and J-coupling evolution during the second τ interval:

$$\begin{aligned} \mathrm{CH} &\Rightarrow P_C 2H_{1z}C_x cos\,(\Omega_C\tau) + P_C 2H_{1z}C_y sin\,(\Omega_C\tau) \\ \mathrm{CH_2} &\Rightarrow P_C 4H_{1z}H_{2z}C_y cos\,(\Omega_C\tau) - P_C 4H_{1z}H_{2z}C_x sin\,(\Omega_C\tau) \\ \mathrm{CH_3} &\Rightarrow -P_C 8H_{1z}H_{2z}H_{3z}C_x cos\,(\Omega_C\tau) - P_C 8H_{1z}H_{2z}H_{3z}C_y sin\,(\Omega_C\tau)\,. \end{aligned} \tag{6.6}$$

The final ^{1}H and ^{13}C pulses, as previously, will generate single-quantum coherence terms, modulated by the angle θ:

$$\begin{aligned} \mathrm{CH} \Rightarrow &+ P_C 2H_{1z}C_x cos\,(\Omega_C\tau)\, cos\,(\theta) \\ &- P_C 2H_{1z}C_y sin\,(\Omega_C\tau)\, cos\,(\theta) \\ \mathrm{CH_2} \Rightarrow &- P_C 4H_{1z}H_{2z}C_y cos\,(\Omega_C\tau)\, cos^2\,(\theta) \\ &- P_C 4H_{1z}H_{2z}C_x sin\,(\Omega_C\tau)\, cos^2\,(\theta) \\ \mathrm{CH_3} \Rightarrow &- P_C 8H_{1z}H_{2z}H_{3z}C_x cos\,(\Omega_C\tau)\, cos^3\,(\theta) \\ &+ P_C 8H_{1z}H_{2z}H_{3z}C_y sin\,(\Omega_C\tau)\, cos^3\,(\theta)\,. \end{aligned} \tag{6.7}$$

Pulses/Acquisition	^{1}H 90°	^{1}H 180°	^{1}H θ	^{13}C 90°	^{13}C 180°	Acquisition
Phase cycle # 1 (degrees)	0	0	90	0	0	90
Phase cycle # 2 (degrees)	0	0	270	0	0	270

Table 6.1: Phase cycling scheme for the DEPT sequence. θ is the final ^{1}H pulse.

Finally, the ^{13}C signal yielded at the end of the third τ interval from this coherence pathway will carry the ^{13}C initial polarisation and will be oriented along the y axis:

$$\begin{aligned} \mathrm{CH} &\Rightarrow P_C C_y cos\,(\theta) \\ \mathrm{CH_2} &\Rightarrow P_C C_y cos^2\,(\theta) \\ \mathrm{CH_3} &\Rightarrow P_C C_y cos^3\,(\theta)\,. \end{aligned} \tag{6.8}$$

As mentioned previously, these resonances are not localised, and thus must not be allowed to contribute to the signal. Therefore, a 2-step phase cycling scheme, described in Table 6.1, was implemented in the DEPT sequence to eliminate this component. The phase of the last ^{1}H pulse is varied so the pulse is applied along the y and -y direction, respectively for each phase step. The phase cycling scheme on the localised terms (CH group example, Eq. 6.5) will generate two components with opposite signs, since $sin\,(-\theta)$ is equivalent to $-sin\,(\theta)$, while for the non-localised terms (Eq. 6.8) both components have the same sign, due to the trigonometric identity $cos\,(-\theta) = cos\,(\theta)$. Finally, the phase cycling scheme on the acquisition segment will result in the subtraction of these components:

$$\begin{aligned} &P_C C_y cos\,(\theta) - P_C C_y cos\,(\theta) = 0 \\ &P_H C_x sin\,(\theta) + P_H C_x sin\,(\theta) = 2P_H C_x sin\,(\theta)\,. \end{aligned} \tag{6.9}$$

The non-localised component is thereby eliminated.

In addition to phase cycling, crusher gradient pulses (spoilers) were also added in all of the field gradient directions to further eliminate unwanted coherences related to RF profiles imperfections. All spoilers were implemented with a strength of 10 mT/m and duration of 1 ms.

All RF pulses used in the DEPT sequence were block pulses. Adiabatic pulses are often used when the B_1 field is extremely inhomogeneous, due to their insensitiv-

ity to variations in the RF field amplitude. Even though in this study, a birdcage coil is used for both ^{1}H and ^{13}C channels, which is associated with a more homogeneous B_1 field compared to a surface coil, the homogeneity of the dynamic magnetic field rapidly degrades with increasing static magnetic field strength. On the other hand, the performance of adiabatic pulses is dependent on whether the RF amplitude is above a certain threshold value. Given that the ^{1}H and ^{13}C coils have a maximum transmit B_1 field of 12 μT and 70 μT, respectively, it would not be possible to reach the adiabatic condition when using BIR pulses. Additionally, the long duration of these pulses is not compatible with the timing for the polarisation transfer.

Another consequence of not utilising adiabatic pulses is the reduced bandwidth achieved with solely amplitude-modulated pulses. Ideally, such dynamic studies require broadband excitation/inversion of the ^{13}C-labelled metabolites, since fewer assumptions in the model lead to more robust metabolic modelling. In this study, the focus is on the detection of the GluC3, GluC4, GlnC3 and GlnC4. Moreover, the signal from GluC4 and GlnC4, originated from the labelling of these metabolites in the first turn of the TCA cycle, is the most crucial for the metabolic modelling, and thus the transmit frequency was centred on these resonances. The effect of the limited bandwidth on the ^{1}H and ^{13}C signal is shown in Figure 6.2. The magnetisation in the x- and y- axis after the application of a 180° refocusing pulse was simulated through the Bloch equations to demonstrate the case of narrowest bandwidth within the sequence. In the ^{1}H channel, the pulse is centred at 2.43 ppm (green dashed line) with the resonances in the edges (black dashed lines) at 2.67 ppm and 1.82 ppm, corresponding to the multiplets of GlnC4 and GluC3, respectively. In this case, the refocusing profile is almost perfect, since 98% to 100% of the magnetisation of the spectral region of interest is refocused. On the other hand, the ^{13}C pulse is centred at 33 ppm. The GluC4 triplet resonance at 36.1 ppm is close to full refocusing (99%), while only 69% of the GlnC3 triplet resonance (25.4 ppm) magnetisation is refocused. Also, note in the ^{13}C channel that a non-nulled M_x component (red trace) appears for chemical shifts larger or smaller than the central frequency. The crusher gradients will act on these components, preventing them from contributing to the overall signal.

Spatial localisation, performed with the ISIS sequence, preceded the polarisation transfer module (Figure 6.1). Therefore, a total of 16 phase steps were implemented in the ISIS-DEPT sequence (ISIS: 8 steps × DEPT: 2 steps). The ISIS sequence used AFP inversion pulses, more specifically, offset independent trapezoid (OIT) adiabatic inversion pulses [12] with sufficiently large bandwidth at 12 μT (3829 Hz) to reduce the chemical shift displacement artefact and of sufficiently short duration to ensure that the RF power output was within the specific absorption rate (SAR) limits. ^{1}H decoupling was not applied in this study, due to the SAR limitations. Crusher gradients, identical to the ones added in the DEPT sequence, were also introduced in between the AFP pulses in all the field gradient directions to avoid transverse magnetisation terms in the ISIS preparation of the ^{1}H spins.

6.2.2 MR measurements & data processing

6.2.2.1 Phantom experiments

All measurements were performed on a 7 T Philips Achieva magnetic resonance (MR) system (Philips Healthcare, Best, Netherlands) using a ^{13}C/^{1}H volume coil (RAPID Biomedical, Würzburg, Germany) with maximum B_1 of 70 μT and 12 μT, for the ^{13}C and ^{1}H channels, respectively. Prior to the acquisition of DEPT ^{13}C

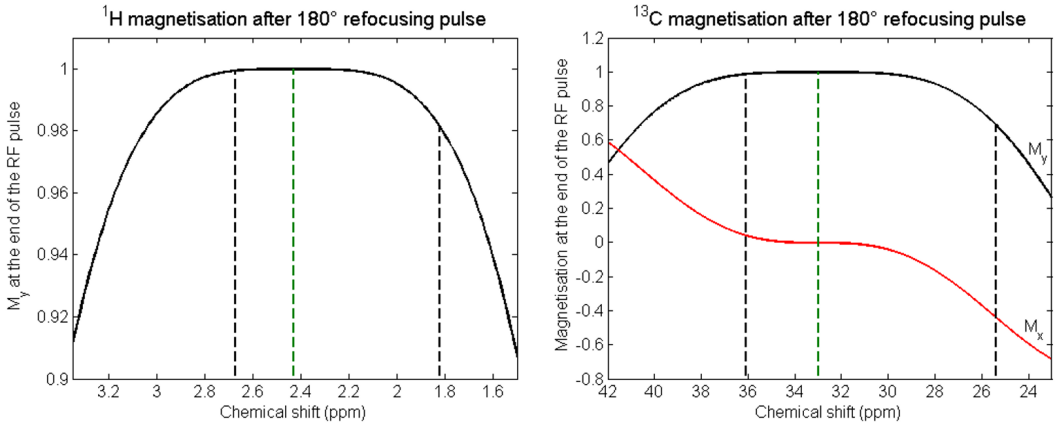


Figure 6.2: X- and y- axis magnetisation after the application of a 180° refocusing pulse simulated through the Bloch equations. In the ^{1}H channel, 98% - 100% of the magnetisation of the spectral region of interest is refocused, while in the ^{13}C channel the refocusing efficiency decreases to 69% - 99%. Pairs of crusher gradients are used to spoil the ^{13}C and ^{1}H magnetisation components arising from the imperfect 180° rotations, and avoid unwanted coherences in the detected signal. The magnetisation profiles were simulated considering a transmit B_1 field of 12 μT and 70 μT for the ^{1}H and ^{13}C channels, respectively.

spectra, the flip angle of the block pulses was calibrated to account for B_1 inhomogeneities and coil loading effects in both channels. In the ^{1}H channel, a stimulated echo acquisition mode (STEAM) [13, 14] sequence (repetition time - TR/TE = 2000/34.9 ms, 1 average) without water suppression was used to obtain a high amplitude signal in the same voxel location as the following DEPT acquisitions. In the ^{13}C channel, a high amplitude ^{13}C signal was obtained from a formic acid bubble ([^{13}C] = 20 700 mM), positioned as shown in Figure 6.7a, using an unlocalised pulse acquire sequence (TR/acquisition delay = 2000/0.55 ms, 2 averages). The flip angles were arrayed to include the amplitude/B_1, in which signal nulling was observed, being then scaled to match a theoretical 180°. The ^{13}C calibration scan was also used to adjust the ^{13}C frequency offset for the subsequent scans, based on the formic acid resonance (Table 6.2).

To test the performance of the DEPT sequence, non-localised ^{13}C spectra were acquired from a [1,2-^{13}C]acetate phantom ([^{13}C] = 32 mM). The experimental set-up also included a human head phantom (H_2O, 13 g of NaCl, 11.5 g of $CuSO_4$, Nova Medical, Wilmington, Massachusetts, USA) positioned as depicted in Figure 6.5a, to achieve similar loading conditions to an *in vivo* human experiment. The unlocalised DEPT spectra (θ = 35°, TR = 2500 ms) acquired with and without crusher gradients were compared to one acquired with a spin echo sequence (TR = 10 000 ms). The common parameters were TE = 7.89 ms, readout bandwidth (BW) = 5000 Hz, number of samples = 1024, 32 averages.

The ISIS localisation accuracy was assessed by acquiring ^{13}C spectra from the same sample within a 30x30x30 mm^3 voxel placed inside (Figure 6.6a) and on the outer edge (Figure 6.6c) of the phantom, using the ISIS-DEPT sequence (128 av-

Metabolite	Carbon atom	Spectral position (ppm)	J_{CC} (Hz)	J_{CH} (Hz)
Acetate	C2	24.5	52	127.1
Glutamate	C2	55.6	C1-C2 = 53.4	145.2
	C3	27.8	C2-C3 = 34.6	131.4
	C4	34.4	C3-C4 = 34.6	126.7
Glutamine	C2	55.1	C1-C2 = 53.4	145.4
	C3	27.1	C2-C3 = 34.9	131.4
	C4	31.7	C3-C4 = 34.9	128.3
Formic acid	C1	168.0	-	220.0

Table 6.2: Spectral position, homonuclear and heteronuclear scalar coupling constants for the relevant metabolites [15, 16, 17, 18, 19].

erages) with the same DEPT parameters as above. An additional spectrum was acquired from a 20x20x20 mm^3 voxel placed inside the phantom (Figure 6.6b), in order to compare with the one acquired with the larger volume voxel and check the signal amplitude proportionality with voxel size. The transmit frequency was set to 24.5 ppm.

Further tests were performed on a glutamate phantom with 5 mM of natural abundance ^{13}C (1.1%) with identical ISIS-DEPT parameters used in the *in vivo* human experiments (TR/TE = 2500/7.69 ms, $\theta = 45°$), except the sequence was run for 30 minutes (720 averages) with a voxel size of 30x30x30 mm^3. To attain a similar noise contribution to an *in vivo* human experiment, a volunteer was asked to remain with the head adjacent to the phantom for the duration of the scanning session, as depicted in Figure 6.7a. The transmit frequency was set to 33 ppm.

Peak areas were calculated with the amplitude of the free induction decay (FID) using accurate, robust, and efficient spectral fitting (AMARES) [20] from the jMRUI software [21]. Prior knowledge for metabolite quantification included linewidth matching based on the estimation of a peak with high amplitude and frequency constraints based on the chemical shifts and J-coupling constants in Table 6.2. Starting points for 0^{th}-order phase correction were provided, whilst 1^{st}-order phase correction was set to zero. All peaks were modelled as singlet Lorentzian functions.

6.2.2.2 Human experiments

Four subjects participated in this study: three healthy volunteers with no personal or family history of psychotic disorders (2 males, age range: 21 - 30 years old) and one volunteer diagnosed with early stage psychosis (male, 41 years old). The participants gave informed consent to a protocol approved by the local ethics committee. A nurse and medical doctor were present in all studies and performed all the medical interventions. The MR system used for these experiments was the same as described above for the phantom experiments.

Prior to the MR measurements, the volunteers underwent a preparation protocol for the experiment, which included placement of a line in the antecubital vein for intravenous infusion of [1-^{13}C]glucose and a line in the dorsal foot vein for peri-

odic blood sampling. When transferred to the scanner room, the participants were asked to introduce the foot with the venous line into a hot box for the entirety of the scanning session, to accelerate blood circulation, and thus mimic arterial blood (arterialised venous blood). The patients were positioned comfortably inside the scanner and two calcium titanate dielectric pads were placed on top of the frontal region of the skull to strengthen and improve the homogeneity of the B_1 field in that area (see section 3.3.1.4 for more information on the dielectric pads).

A summary of the MR protocol pipeline is provided in Figure 6.3. Preceding the start of the infusion, a number of pre-scans were run. Survey images were acquired to ensure the dielectric pads were correctly positioned. ^{13}C and ^{1}H calibration scans were run, as described in the phantom experiments section, except the STEAM sequence was replaced by an ISIS sequence (TR/TE = 2000/0.81 ms, 8 averages). The calibration scans were followed by two semiadiabatic localisation by adiabatic selective refocusing (sLASER) [22] scans (TR = 5000 ms, voxel size = 60x45x20 mm^3, 64 averages) with optimised TEs for the detection of both glutamate and glutamine, and of exclusively glutamate. These ^{1}H spectra are used for the conversion of the turnover curves into ^{13}C concentration (glutamate spectrum), as well as to measure the pool size of glutamate and glutamine for the metabolic modelling. TE optimisation was achieved by simulating the glutamate and glutamine signals arising from a sLASER sequence comprised of only block pulses using Versatile Simulation, Pulses, and Analysis (VESPA) [23] software with TE values ranging from 64 to 144 ms (step size of 16 ms). The optimised TE for the acquisition of glutamate and glutamine was 96 ms (interpulse timings of 12, 24, 24, and 24 ms) and of only glutamate was 144 ms (interpulse timings of 18, 36, 36, and 36 ms).

The effect of dielectric pads on the sequences described above is shown in Figure 6.4, using data from an additional healthy volunteer (female, 27 years old) for demonstration purposes. With the dielectric pads, the region of high-intensity on the survey images is redirected towards the ACC, where the spectra are acquired from (Figure 6.4a). A more homogeneous B_1 field resulted in an almost complete cancellation of the signal in the ^{1}H calibration scans, achieved at the real 180°, in contrast to the situation with no dielectric pads, in which signal nulling is not

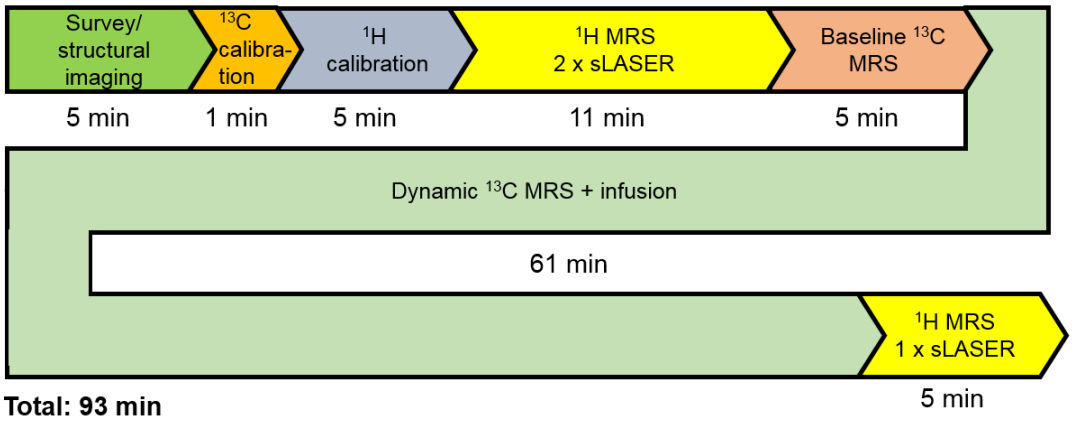


Figure 6.3: ^{13}C human study MR protocol pipeline.

observed (Figure 6.4d). In addition, a significant increase in signal-to-noise ratio (SNR) is observed in the ^{1}H spectrum (Figure 6.4e). As expected, the presence of the dielectric pads did not significantly affect the ^{13}C calibration spectra (Figure 6.4c). B_1 inhomogeneities in ^{13}C experiments are not as severe as in ^{1}H MRS, as the RF wavelength is four times larger, minimising the generation of standing waves.

Immediately before the infusion, an ISIS-DEPT sequence (128 averages) was run to assess potential baseline distortion and/or lipid contamination. To minimise the presence of lipids in the spectra, one saturation slab (see subsection 3.3.1.3 for more information) was placed over the subject's scalp (Figure 6.4b) in all ISIS-DEPT scans ($\theta = 45°$, TR/TE = 2500/7.69 ms, $BW = 5000$ Hz, number of samples = 1024, voxel size = 85x50x30 mm^3). Subsequent ISIS-DEPT scans (4x368 averages) were run during infusion of the ^{13}C substrate.

The infusion protocol was designed to obtain a rapid high steady-state isotopic enrichment of the substrate. The intravenous glucose concentration is raised from euglycaemic levels ($\sim$ 4 mM following overnight fast) to hyperglycaemic levels (10 - 12 mM). The periodic blood sampling during the infusion (every 5 minutes) was used to control the glucose infusion rate and provide information on the isotopic enrichment time courses for the metabolic modelling. Finally, the TE = 144 ms sLASER scan was repeated for quantification of the ^{1}H-^{13}C multiplets of GluC4, in order to obtain its fractional enrichment for absolute scaling of the ^{13}C turnover curves. The total scan time of each ^{13}C human study was approximately 90 min-

utes.

The dynamic ^{13}C spectra were averaged into blocks of 240 averages, yielding a time series with 10 minutes of temporal resolution (6 spectra). The spectral analysis performed for the *in vivo* data was identical to the one performed for the *in vitro* data. Due to the limited SNR of the human data, additional constraints were

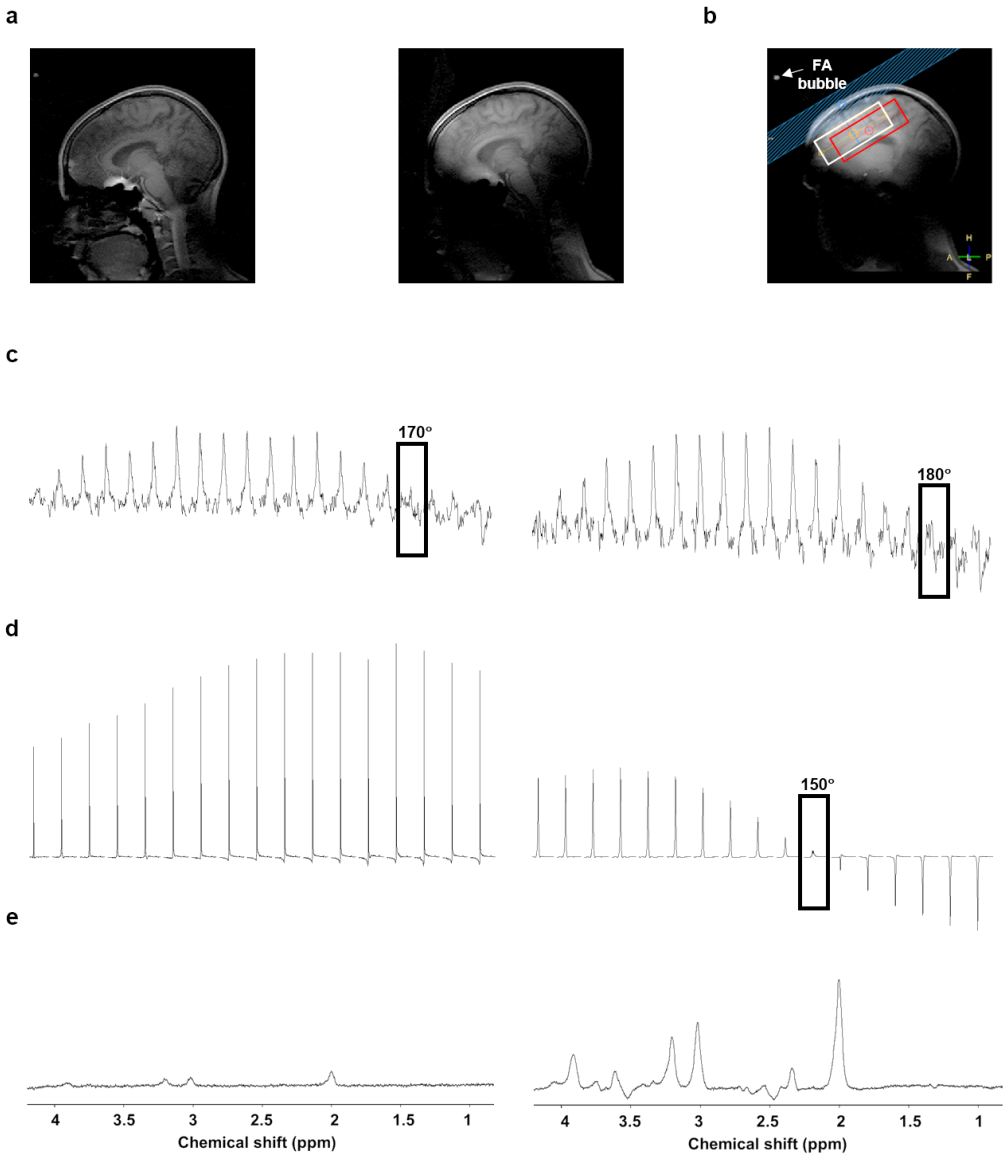


Figure 6.4: Effect of dielectric pads, placed on top of the subject's frontal region, on the sequences acquired prior to the ^{13}C dynamic scans: survey images (a), ^{13}C calibration scan (c), ^{1}H calibration scan (d) and sLASER (TE = 96 ms) sequence (e). Images on the left and right represent the condition prior and after the placement of the dielectric pads, respectively. The survey image in b) shows the position of the GluC4-shifted volume (white box) onto the ACC for the acquisition of the ISIS-DEPT spectra. Also note the formic acid (FA) bubble observable on the same image. The ^{13}C spectra, which show only one peak of the doublet yielded by the formic acid resonance, were zero-filled to 2048 points, phase corrected and line-broadened with a 15 Hz Lorentzian filter.

applied to the prior knowledge of AMARES for the calculation of peak areas. The frequency of the central peaks of GluC4, GlnC4, GluC3 and GlnC3 was restrained to a range of 0.2 ppm centred on the resonances listed in Table 6.2. The frequency of the remaining peaks was constrained based on their J-coupling constants, also listed in Table 6.2. The linewidth of all peaks was matched to the one of the GluC4 central peak.

The same analysis as described above was performed in an area without resonances to obtain an estimate of the noise contribution in the quantification, which was subsequently subtracted from the peak area measures. Area values for each triplet were combined to determine GluC4, GlnC4, GluC3 and GlnC3 turnover curves for each subject.

6.3 Results

6.3.1 Phantom experiments

The unlocalised DEPT SNR gain on the AceC2 resonances (^{13}C signal in the position 2 in acetate) was 2.98 compared to the ^{13}C spin echo signal acquired with identical TE (Figure 6.5b). There was an increase in SNR of approximately 5% when the crusher gradients were removed from the sequence. This confirms the role of the gradients in spoiling the original ^{13}C magnetisation that does not arise from the polarisation transfer pathway. The ^{1}H ISIS localization scheme proved to be effective, as minimal signal was detected in the configuration with the acetate-shifted voxel placed adjacent to the phantom (Figure 6.6c). Furthermore, the AceC2 signal was reduced by approximately 3.24 when the volume decreased by 3.38 times, validating the proportionality of the signal amplitude with the voxel size (Figures 6.6a and b).

In the acquisitions on the glutamate phantom, the narrow bandwidth of the block pulses, due to the limited available B_1, was reflected in the reduced enhancement of the GluC3 resonances as compared to the GluC4 peaks, on which the carrier frequency was centred. The relative areas of the GluC3 and GluC4 triplet peaks to the GluC4 central peak are depicted in Figure 6.7b. Similarly, the bandwidth limitation does not allow the quantification of the GluC2 doublet, due to the poor

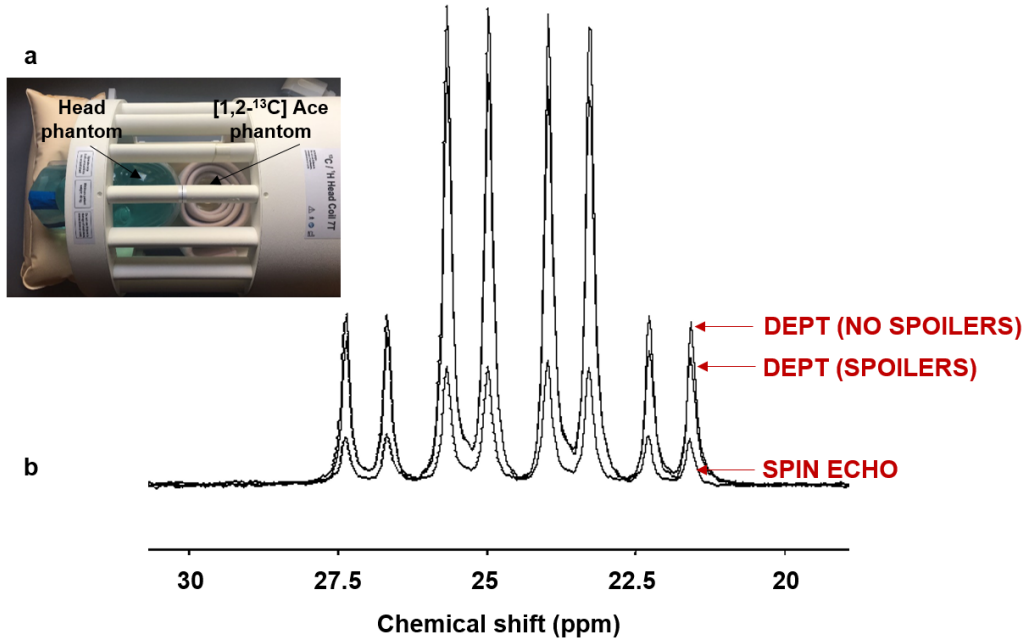


Figure 6.5: ^{13}C *in vitro* experiments. Experimental set-up with a [1,2-^{13}C]acetate phantom ([^{13}C] = 32 mM) and a human head phantom to achieve similar loading conditions to the *in vivo* experiments (a). Comparison of ^{13}C spectra using unlocalised DEPT (with and without spoilers - $\theta = 35°$, TR = 2500 ms) and spin echo (TR = 10 000 ms) sequences (b). The common parameters were TE = 7.89 ms, BW = 5000 Hz, number of samples = 1024, 32 averages. The transmit frequency was set to 24.5 ppm. The spectra were zero-filled to 2048 points, phase corrected and displayed in jMRUI with 8 Hz of line broadening.

excitation/refocusing profile for these resonances, visible as out-of-phase peaks.

6.3.2 Human experiments

The ^{13}C time series spectra from one subject are shown in Figure 6.8. The offset frequency was set at 33 ppm. However, as the B_0 field is not homogeneous across the coil, the static magnetic field on the formic acid bubble, which was used to adjust the ^{13}C frequency offset, is not the same as the one in the subject's brain, leading to perceivable frequency shifts. For this reason, the GluC4 central resonance appears at 36.7 ppm in Figure 6.8, instead of the expected 34.4 ppm. Frequency shifts varied between 4.4 and 1.9 ppm for all subjects' data.

The fitting of the GluC4, GlnC4, GluC3 and GlnC3 resonances in the 60-minute averaged spectrum is depicted in Figure 6.9 for the same subject as above. Note the flat residue between the data and the AMARES fit. In this case, only two resonances of the GlnC3 triplet were successfully fitted.

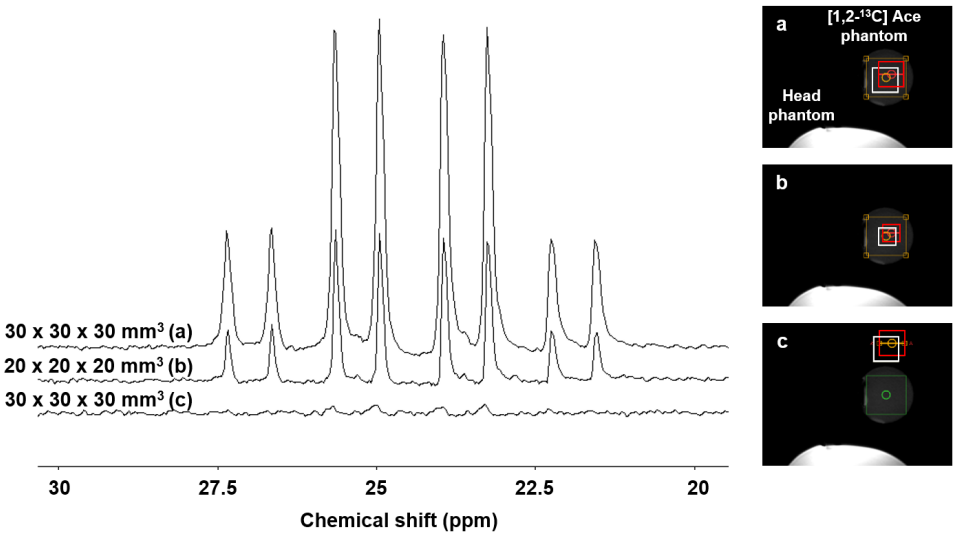


Figure 6.6: ^{13}C ISIS-DEPT spectra from a [1,2-^{13}C]acetate phantom ([^{13}C] = 32 mM) with a similar set-up as the experiment depicted in Figure 6.5a. The ISIS-DEPT sequences (θ = 35°, TR/TE = 2500/7.89 ms, BW = 5000 Hz, number of samples = 1024, 128 averages) were run with three different voxel configurations: a) 30x30x30 mm^3 voxel inside the phantom, b) 20x20x20 mm^3 voxel inside the phantom and c) 30x30x30 mm^3 voxel on the outer edge of the phantom. The transmit frequency was set to 24.5 ppm. The white boxes on the survey images represent the acetate-shifted voxel. The spectra were zero-filled to 2048 points, phase corrected and displayed in jMRUI with 8 Hz of line broadening.

In Figure 6.10, group-averaged GluC4, GlnC4, GluC3 and GlnC3 turnover curves calculated from the individual subject dynamic ^{13}C spectra are shown.

6.4 Discussion

In vivo ^{13}C MRS is currently the only method which provides information on cell-specific neuroenergetics and neurotransmission cycling. However, its use is limited by several factors, including the complexity and cost of ^{13}C-labelled substrate infusion experiments, added to the low sensitivity of the ^{13}C signal and RF heating concerns. The technical issues have driven the majority of brain ^{13}C studies to be constrained to the occipital region. In this study, these issues were addressed, in order to enable the acquisition of ^{13}C spectra from the ACC. The ACC is part of the salience network hypothesised to play a key role in schizophrenia [24], thus making the study of this brain structure of interest for the investigation of the pathogenesis of psychiatric disease. The work shown here included the development of an appropriate MRS sequence, its validation with the relevant phantoms

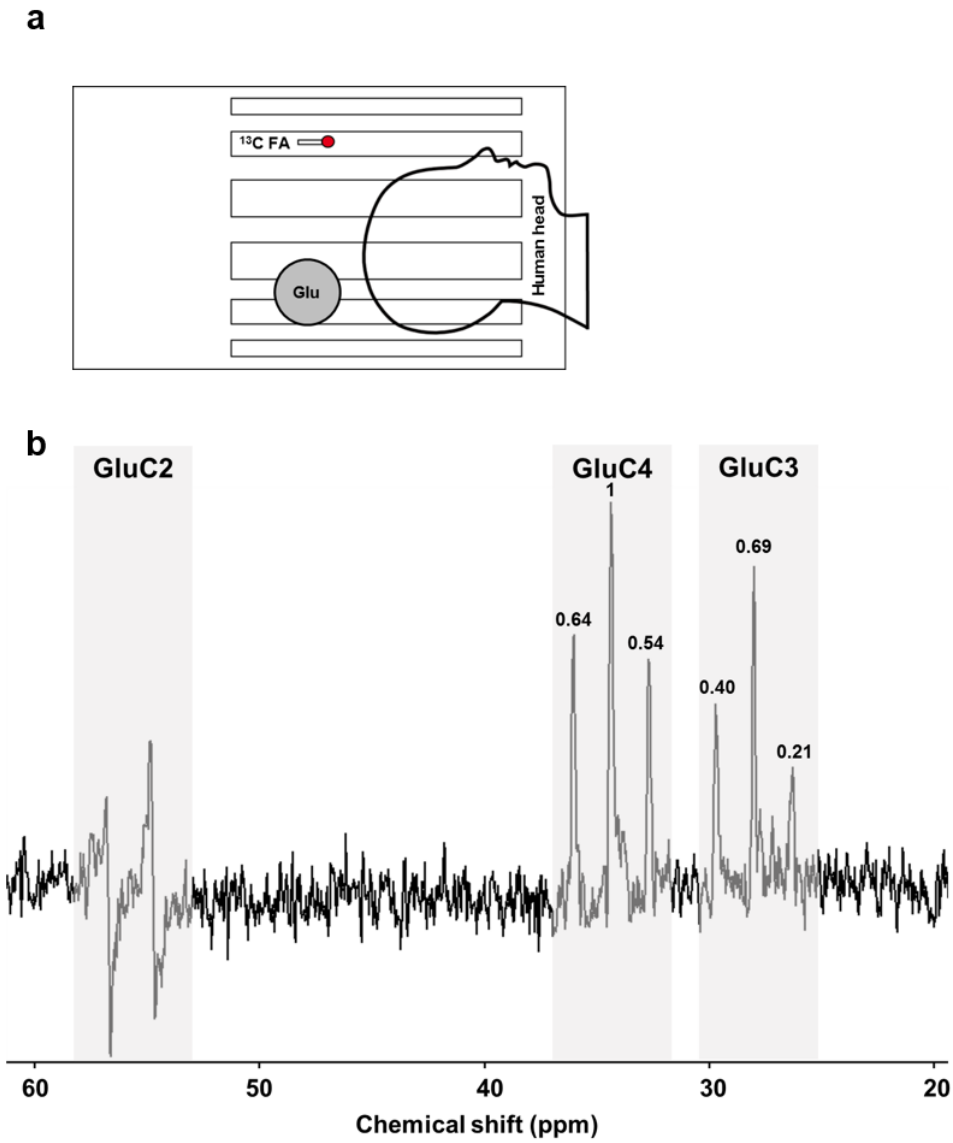


Figure 6.7: ^{13}C spectrum from a glutamate phantom ([^{13}C] = 5 mM) using the ISIS-DEPT sequence (θ = 45°, TR/TE = 2500/7.69 ms, BW = 5000 Hz, number of samples = 1024, 720 averages, voxel size = 30x30x30 mm^3). The transmit frequency was set to 33 ppm. The phantom was introduced in the coil together with a volunteer's head to simulate the noise contribution of an *in vivo* experiment (a). The relative areas of the GluC3 and GluC4 triplets peaks are displayed in b). The spectrum was zero-filled to 2048 points, phase corrected and displayed in jMRUI with 8 Hz of line broadening.

and the application of this technique in healthy volunteers and a patient with early schizophrenia.

An ISIS-DEPT sequence developed in-house was used to collect the ^{13}C data. Care was taken to ensure that no signal from the non-localised component sur-

vived at the end of the acquisition of the spectra. Thus, a phase cycling scheme was applied to the last ^{1}H pulse and acquisition step. Furthermore, crusher gradients were also included in the ISIS and DEPT segments to spoil the unwanted coherences. Ultimately, the aim was to achieve a signal enhancement of four-fold, promoted by the polarisation transfer mechanism in the DEPT module.

The effectiveness of the polarisation transfer was tested with an acetate phantom and showed an unlocalised DEPT SNR gain of approximately 3 when compared to signal acquired with a spin echo sequence. This experiment also allowed the

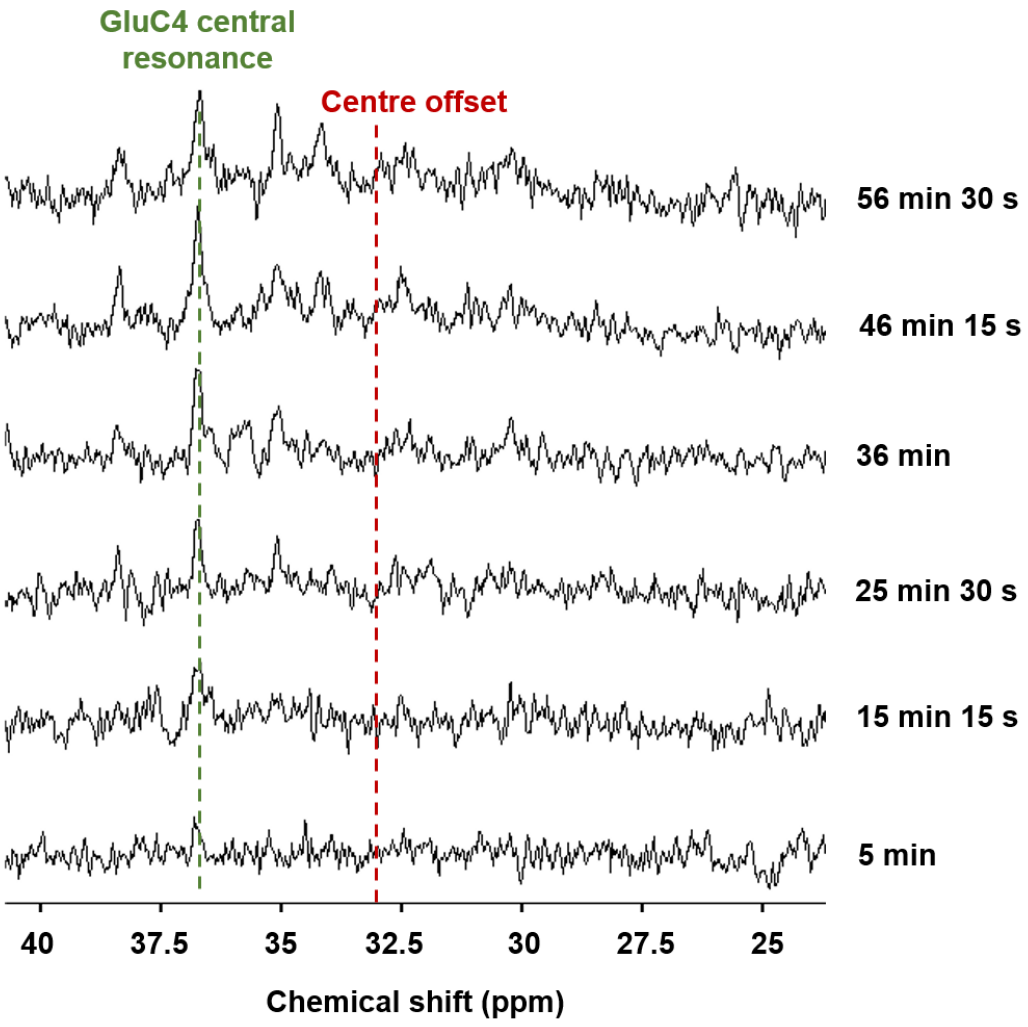


Figure 6.8: Time series spectra obtained during the infusion of [1-^{13}C]glucose from one subject's ACC. Dynamic ^{13}C data were acquired using the ISIS-DEPT sequence ($\theta = 45°$, TR/TE = 2500/7.69 ms, $BW = 5000$ Hz, number of samples = 1024, voxel size = 85x50x30 mm^3) and were averaged into blocks of 240 averages to yield a temporal resolution of 10 minutes. The transmit frequency (centre offset) was set to 33 ppm. The spectra were zero-filled to 2048 points, phase corrected and displayed in jMRUI with 8 Hz of line broadening.

performance of the crusher gradients in eliminating unwanted coherences to be tested. A decrease in SNR of approximately 5% was observed when the gradients were active in the sequence. In addition, the localisation accuracy proved to be adequate when tested with three different configurations (voxel placed adjacent, completely inside and outside the Ace phantom).

The use of a 7 T system in this study permitted an increment in the signal sensitivity, which is of great importance for direct ^{13}C MRS experiments. However, higher field systems also impose several constraints, mainly related to the RF power deposition, which increases with the field strength. This limits the magnitude of the transmit field of the coil, thus also reducing the bandwidth of the RF pulses. In addition, the use of decoupling was avoided to ensure acceptable average and local SAR in the subject during RF exposure. Nevertheless, an *in vitro* experiment performed on a natural abundance ^{13}C glutamate phantom (30 minutes of acquisition) revealed a sufficient SNR for the detection of the glutamate triplets, even

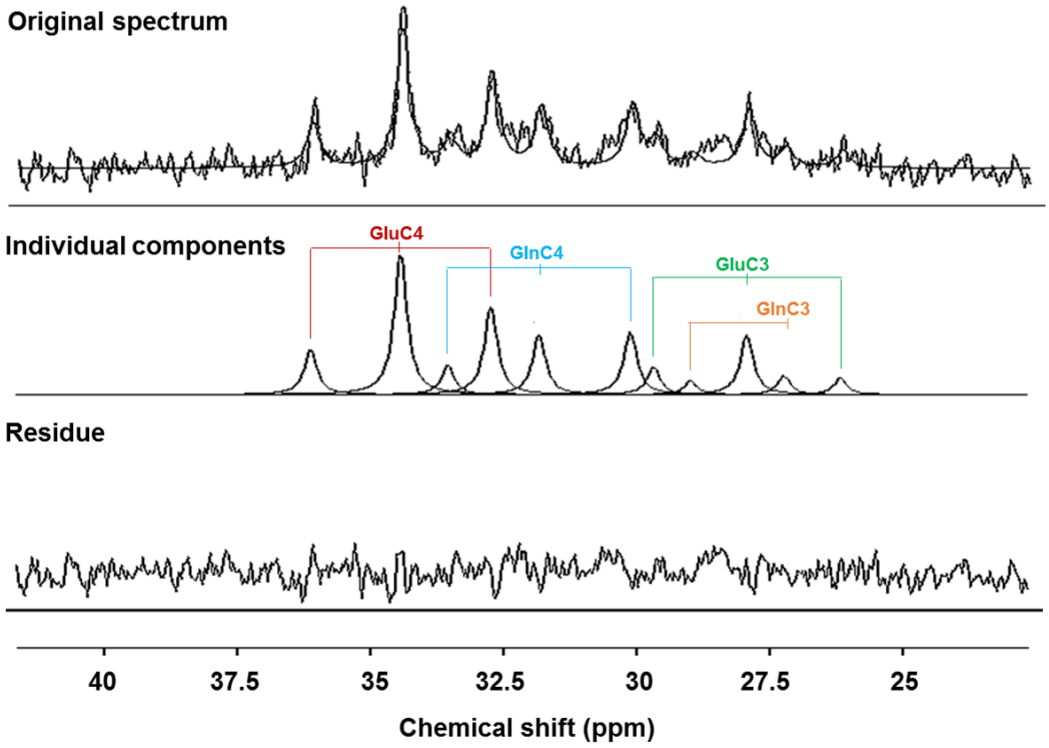


Figure 6.9: Example of a 60-minute averaged individual subject spectrum (ISIS-DEPT, $\theta = 45°$, TR/TE = 2500/7.69 ms, $BW = 5000$ Hz, number of samples = 1024, voxel size = 85x50x30 mm^3) obtained during the infusion of the ^{13}C substrate and corresponding AMARES fits for the GluC4, GlnC4, GluC3 and GlnC3 resonances and resulting residue. The GluC4 central peak position was shifted to 34.4 ppm. The spectrum was zero-filled to 2048 points, phase corrected and displayed in jMRUI with 8 Hz of line broadening.

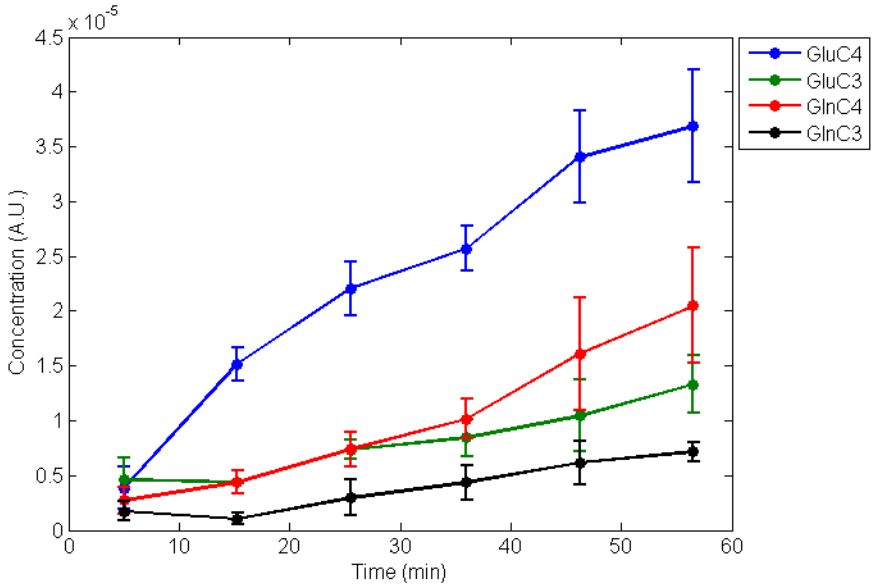


Figure 6.10: GluC4, GlnC4, GluC3 and GlnC3 turnover curves obtained during the infusion of [1-^{13}C]glucose. The group-averaged (N = 4) time courses were calculated from the individual subject spectra with a temporal resolution of 10 minutes. Error bars represent standard error of the mean.

without decoupling. Moreover, the RF pulse bandwidth allowed the detection of GluC4 and GluC3, despite the reduced signal enhancement of the GluC3 triplets. The distortion of the GluC2 resonances, due to the bandwidth limitation indicates that this carbon position is not quantifiable, which means that more assumptions need to be made when modelling the dynamic ^{13}C data.

The MR protocol for the *in vivo* experiments included the use of dielectric pads to steer a constructively interfering B_1 field into the ACC region. Results of the scans preceding the dynamic ^{13}C spectra acquisition showed a considerable improvement in the ^{1}H MRS; signal nulling was achieved close to the nominal 180° in the ^{1}H calibration series and a significant increase in SNR was observed in the sLASER spectra. A homogeneous B_1 field within the volume-of-interest in the ^{1}H channel is crucial for the DEPT acquisitions, as it affects the performance of the polarisation transfer mechanism. With the optimised sequences and set-up, it was possible to obtain time series spectra with a temporal resolution of 10 minutes and reasonable SNR. The use of saturation slabs permitted the acquisition of spectra with minimal lipid contamination from the scalp. From the dynamic ^{13}C data, GluC4, GlnC4, GluC3 and GlnC3 turnover curves during the infusion were obtained. The temporal evolution of these curves is in agreement with the

ones obtained in previous studies in rodents [25, 26, 27, 28]; a higher fractional enrichment was observed in GluC4, followed by GluC3, GlnC4 and GlnC3. At 60 minutes of infusion of [1-^{13}C]glucose, steady-state of the labelled metabolic products had not been achieved.

The aim of this work was to show the feasibility of acquiring dynamic ^{13}C spectra from a deep brain structure. Further work has to be done to translate these results into meaningful TCA cycle and glutamate-glutamine cycle rates. For the calculation of the quantitative metabolic fluxes, the turnover curves have to be scaled to ^{13}C concentration, which needs a reference point. This can be done if the ^{13}C concentration of one of the resonances, e.g., GluC4 is known at a given time point, typically at the last time point, to ensure enough SNR and stability in the ^{13}C concentration. For that, the glutamate total pool size is initially extracted from the spectrum acquired with the sLASER sequence with a TE = 96 ms before the start of the infusion. Posteriorly, information on the fractional enrichment of the ^{13}C label on the GluC4 resonance has to be obtained. A proton-observed carbon edited (POCE) sequence [29] is commonly used immediately after the last ISIS-DEPT acquisition, as it can directly determine the ^{13}C isotopic enrichment. The POCE sequence is a ^{1}H-[^{13}C] MRS technique, which selects the protons bound to ^{13}C atoms, by means of J-difference editing. However, this requires the implementation of a new pulse sequence in the MR system.

Boumezbeur et al. [30] proposed a more straightforward approach for the detection of the ^{13}C incorporation into glutamate. A standard ^{1}H MRS sequence was used to examine the decrease in ^{12}C-bounded glutamate protons and the increase in ^{13}C satellites. These two components should have the same peak area with opposite signs. In this work, a similar strategy was considered. A sLASER sequence with TE = 144 ms was run before and after the infusion and the pair of spectra was compared. No satellite peaks could be detected in the post-infusion spectrum. The difference between this study and the one of Boumezbeur et al. is that the latter was performed at 3 T, which minimises the overlap between the ^{1}H glutamate peaks (GluC4 and GluC3) and its ^{13}C satellite peaks. At higher field strengths, the frequency difference between the ^{1}H glutamate peaks increases, whereas the heteronuclear scalar coupling remains the same, leading to a partial overlap of

these peaks. There is a complete overlap at 6.1 T [30]. Inaccurate determination of the isotopic enrichment can lead to systematic errors in the analysis of the dynamic ^{13}C spectra. Therefore, a more robust method needs to be used in this study, most likely involving the implementation of the POCE sequence.

Another procedure that could improve the accuracy of the quantification of the ^{13}C spectra is the addition of a prior knowledge constraint related to the amplitude of the multiplet peaks, which accounts for the asymmetric signal enhancement of all resonances, due to the limited bandwidth and different efficiency of the DEPT sequence on the chemical groups of interest. Furthermore, frequency shifts were observed in the *in vivo* data, which varied between 4.4 and 1.9 ppm. Thus, calibration curves as a function of the frequency offset could be generated using data acquired from the natural abundance ^{13}C glutamate phantom. The curves would provide the real amplitudes of each peak relative to the GluC4 central peak for each frequency offset.

In conclusion, this work presented a full methodology for the detection and analysis of dynamic ^{13}C spectra from a deep brain region, with sufficient SNR and without decoupling at ultra high-field. More importantly, despite the complexity of the experiment and the prolonged time that the subjects had to remain in the magnet, it was possible to acquire good quality data from a patient with early schizophrenia. This further demonstrates the feasibility of applying this technique for the study of psychosis.

Bibliography

[1] Robin A de Graaf, Douglas L Rothman, and Kevin L Behar. State of the art direct ^{13}C and indirect ^{1}H-[^{13}C] NMR spectroscopy in vivo. a practical guide. *NMR in biomedicine*, 24(8):958–972, 2011.

[2] R Scott Staewen, Anton J Johnson, Brian D Ross, Todd Parrish, Hellmut Merkle, and Michael Garwood. 3-D FLASH imaging using a single surface coil and a new adiabatic pulse, BIR-4. *Investigative radiology*, 25(5):559–567, 1990.

[3] Shizhe Li, Yan Zhang, Shumin Wang, Maria Ferraris Araneta, Christopher S Johnson, Yun Xiang, Robert B Innis, and Jun Shen. ^{13}C MRS of occipital and frontal lobes at 3T using a volume coil for stochastic proton decoupling. *NMR in Biomedicine*, 23(8):977–985, 2010.

[4] DWJ Klomp, WKJ Renema, M Van Der Graaf, BE De Galan, APM Kentgens, and A Heerschap. Sensitivity-enhanced ^{13}C MR spectroscopy of the human brain at 3 Tesla. *Magnetic resonance in medicine*, 55(2):271–278, 2006.

[5] DWJ Klomp, APM Kentgens, and A Heerschap. Polarization transfer for sensitivity-enhanced MRS using a single radio frequency transmit channel. *NMR in biomedicine*, 21(5):444–452, 2008.

[6] Shizhe Li, Li An, Shao Yu, Maria Ferraris Araneta, Christopher S Johnson, Shumin Wang, and Jun Shen. ^{13}C MRS of human brain at 7 Tesla using [2-^{13}C] glucose infusion and low power broadband stochastic proton decoupling. *Magnetic resonance in medicine*, 75(3):954–961, 2016.

[7] DM Doddrell, DT Pegg, and M Ro Bendall. Distortionless enhancement of NMR signals by polarization transfer. *Journal of Magnetic Resonance (1969)*, 48(2):323–327, 1982.

[8] Roger J Ordidge, Alan Connelly, and Joost AB Lohman. Image-selected in vivo spectroscopy (ISIS). A new technique for spatially selective NMR spectroscopy. *Journal of Magnetic Resonance (1969)*, 66(2):283–294, 1986.

[9] Peter Hore, Jonathan Jones, and Stephen Wimperis. *NMR-The Toolkit: How Pulse Sequences Work*. Oxford University Press, USA, 2015.

[10] Gareth A Morris and Ray Freeman. Enhancement of nuclear magnetic resonance signals by polarization transfer. *Journal of the American Chemical Society*, 101:760–762, 1979.

[11] Malcolm H Levitt. *Spin dynamics: basics of nuclear magnetic resonance*. John Wiley & Sons, 2001.

[12] Baolian Yang and David Leslie Foxall. Broad bandwidth magnetic resonance spectroscopy at high static (B0) magnetic field using polarization transfer, December 27 2016. US Patent 9,529,064.

[13] Jens Frahm, Klaus-Dietmar Merboldt, and Wolfgang Hänicke. Localized proton spectroscopy using stimulated echoes. *Journal of Magnetic Resonance (1969)*, 72(3):502–508, 1987.

[14] J Frahm, H Bruhn, ML Gyngell, KD Merboldt, W Hänicke, and R Sauter. Localized high-resolution proton NMR spectroscopy using stimulated echoes: Initial applications to human brain in vivo. *Magnetic resonance in medicine*, 9(1):79–93, 1989.

[15] Robin A De Graaf. *In vivo NMR spectroscopy: principles and techniques*. John Wiley & Sons, 2013.

[16] Mor Mishkovsky, Tian Cheng, Arnaud Comment, and Rolf Gruetter. Localized in vivo hyperpolarization transfer sequences. *Magnetic resonance in medicine*, 68(2):349–352, 2012.

[17] Pierre-Gilles Henry, Ivan Tkáč, and Rolf Gruetter. ^{1}H-localized broadband ^{13}C NMR spectroscopy of the rat brain in vivo at 9.4T. *Magnetic resonance in medicine*, 50(4):684–692, 2003.

[18] Peter B Barker, Xavier Golay, Dmitri Artemov, Ronald Ouwerkerk, Mari A Smith, and AJ Shaka. Broadband proton decoupling for in vivo brain spectroscopy in humans. *Magnetic resonance in medicine*, 45(2):226–232, 2001.

[19] Séverine Moret, Paul J Dyson, and Gábor Laurenczy. Direct, in situ determination of pH and solute concentrations in formic acid dehydrogenation and CO_2 hydrogenation in pressurised aqueous solutions using ^{1}H and ^{13}C NMR spectroscopy. *Dalton Transactions*, 42(13):4353–4356, 2013.

[20] Leentje Vanhamme, Aad van den Boogaart, and Sabine Van Huffel. Improved method for accurate and efficient quantification of MRS data with use of prior knowledge. *Journal of Magnetic Resonance*, 129(1):35–43, 1997.

[21] A Naressi, C Couturier, JM Devos, M Janssen, C Mangeat, R De Beer, and D Graveron-Demilly. Java-based graphical user interface for the MRUI quantitation package. *Magnetic resonance materials in physics, biology and medicine*, 12(2-3):141–152, 2001.

[22] Tom WJ Scheenen, Dennis WJ Klomp, Jannie P Wijnen, and Arend Heerschap. Short echo time ^{1}H-MRSI of the human brain at 3T with minimal chemical shift displacement errors using adiabatic refocusing pulses. *Magnetic resonance in medicine*, 59(1):1–6, 2008.

[23] BJ Soher, P Semanchuk, D Todd, J Steinberg, and K Young. VESPA: Integrated applications for RF pulse design, spectral simulation and MRS data analysis. In *Proceedings of the International Society for Magnetic Resonance in Medicine, 19th Scientific Meeting and Exhibition*, page 1410, 2011.

[24] Thomas P White, Verghese Joseph, Susan T Francis, and Peter F Liddle. Aberrant salience network (bilateral insula and anterior cingulate cortex) connectivity during information processing in schizophrenia. *Schizophrenia research*, 123(2):105–115, 2010.

[25] Pierre-Gilles Henry, Gülin Öz, Stephen Provencher, and Rolf Gruetter. Toward dynamic isotopomer analysis in the rat brain in vivo: automatic quantitation of ^{13}C NMR spectra using LCModel. *NMR in biomedicine*, 16(6-7):400–412, 2003.

[26] Dinesh Kumar Deelchand, Kâmil Uğurbil, and Pierre-Gilles Henry. Investigating brain metabolism at high fields using localized ^{13}C NMR spectroscopy without ^{1}H decoupling. *Magnetic resonance in medicine*, 55(2):279–286, 2006.

[27] João MN Duarte, Bernard Lanz, and Rolf Gruetter. Compartmentalized cerebral metabolism of [1,6-^{13}C] glucose determined by in vivo ^{13}C NMR spectroscopy at 14.1T. *Frontiers in Neuroenergetics*, 3(3):1–15, 2011.

[28] Marta Lai, Rolf Gruetter, and Bernard Lanz. Progress towards in vivo brain ^{13}C-MRS in mice: Metabolic flux analysis in small tissue volumes. *Analytical biochemistry*, 529:229–244, 2017.

[29] DL Rothman, KL Behar, HP Hetherington, JA Den Hollander, MR Bendall, OAC Petroff, and RG Shulman. ^{1}H-observe/^{13}C-decouple spectroscopic measurements of lactate and glutamate in the rat brain in vivo. *Proceedings of the National Academy of Sciences*, 82(6):1633–1637, 1985.

[30] Fawzi Boumezbeur, Laurent Besret, Julien Valette, Françoise Vaufrey, Pierre-Gilles Henry, Velislav Slavov, Eric Giacomini, Philippe Hantraye, Gilles Bloch, and Vincent Lebon. NMR measurement of brain oxidative metabolism in monkeys using ^{13}C-labeled glucose without a ^{13}C radiofrequency channel. *Magnetic resonance in medicine*, 52(1):33–40, 2004.

Chapter 7

Final remarks

This thesis was focused on the development of new methodologies for the assessment of brain metabolism mechanisms related to neuroenergetics and neurotransmission. Thus, the target metabolites were lactate, a product of non-oxidative metabolism, as well as glutamate and glutamine, both related to neurotransmission. In the case of lactate, its detection is hampered by its low concentration in normal brain and superposition with signals of higher concentration compounds. In Chapter 4, optimisation of the stimulated echo acquisition mode (STEAM) [1, 2] sequence parameters through implementation of a multi-compartment model to characterise J-coupled signals resulted in the detection of a non-contaminated lactate doublet, with sufficient signal-to-noise ratio. This approach is advantageous for use in magnetic resonance (MR) systems which only have implemented basic magnetic resonance spectroscopy (MRS) protocols. Recently, the application of more elaborate sequences, such as the semiadiabatic localisation by adiabatic selective refocusing (sLASER) [3] sequence, has been gaining popularity in ultra high-field MRS; not only is the full intensity of the signal retained, but the chemical shift displacement artefact is significantly reduced due to the inclusion of high bandwidth adiabatic refocusing pulses. Moreover, their implementation in MR scanners of various vendors has become a common practice.

Therefore, in the functional MRS experiment described in Chapter 5, a sLASER sequence was used for the acquisition of dynamic ^{1}H spectra during the application of a visual stimulation paradigm. A similar approach to the one described in the previous chapter was adopted in this chapter; the J-modulation effects were exploited to achieve a dissociation between the lactate peak and the overlapping

resonances. Furthermore, the non-fully relaxed macromolecules at an echo time of 144 ms were fitted with Lorentzian lineshapes. The methodology described in this study added to the use of a longer stimulation period provided a foundation for future studies to investigate the transient/sustained contribution of specific metabolic pathways during neuronal activation. In fact, the determination of the mechanism that dominates in certain cerebral states can provide valuable information for the understanding of brain disease and how metabolic dysfunction in these pathways contribute to it.

Over the past 30 years, ^{13}C MRS has become a relevant asset for establishing a link between neuroenergetics and neurotransmission. In Chapter 6, a protocol was especially designed for the acquisition of dynamic ^{13}C spectra in a well-defined region deep in the human brain at 7 T, which opens the possibility for subsequent ^{13}C infusion studies to probe alterations in human brain energetics and neuronal signalling in any diseased brain region.

Previous ^{13}C MRS studies have reported that approximately 75% of neuronal oxidative adenosine triphosphate (ATP) production is coupled to neurotransmission [4]. These studies show that in resting conditions, neuronal activity accounts for the majority of glucose consumption. These measurements were also performed on the activated brain [5], revealing a fractional increase of 30% in the neuronal oxygen utilisation rate during visual stimulation, which supports the theory that glucose and oxygen consumption are not coupled during neuronal stimulation and is in agreement with the concurrent increase in cerebral ^{1}H lactate signal . Hence, the information provided by ^{13}C MRS is pertinent and consistent with ^{1}H measurements, emphasising the fact that these should be used as complementary techniques. However, ^{13}C MRS has to overcome several challenges that prevent it to become a routine tool. With regards to its low sensitivity, the use of hyperpolarised ^{13}C MRS has been shown to be promising in animal models [6, 7]. Additionally, other studies have demonstrated the feasibility of simplified ^{13}C protocols substituting the intravenous infusion of ^{13}C substrates by oral administration of labelled compounds [8]. Despite these obstacles, ^{13}C MRS has been successfully applied to the study of numerous brain pathologies [9, 10, 11, 12, 13].

Although MRS is able to provide useful information at the metabolic level, non-

invasively and without the use ionising radiation, it is still not widely accepted in the clinical setting. The barrier to its widespread use can be attributed to a lack of standardisation across sites and data quality assurance. As with any quantitative technique, the use of robust data acquisition and analysis methods is essential and the appropriate protocol must be chosen according to the metabolite(s) of interest and MR system capabilities, as well as magnetic field strength. Nevertheless, the contribution of MRS to the investigation of brain disease mechanisms and to the evaluation of therapeutic responsiveness cannot be argued. Raising awareness for potential pitfalls and the importance of rigorous methodology will unquestionably increase the acceptance of this technique as a relevant tool for research and clinical practice.

Bibliography

[1] Jens Frahm, Klaus-Dietmar Merboldt, and Wolfgang Hänicke. Localized proton spectroscopy using stimulated echoes. *Journal of Magnetic Resonance (1969)*, 72(3):502–508, 1987.

[2] J Frahm, H Bruhn, ML Gyngell, KD Merboldt, W Hänicke, and R Sauter. Localized high-resolution proton NMR spectroscopy using stimulated echoes: Initial applications to human brain in vivo. *Magnetic resonance in medicine*, 9(1):79–93, 1989.

[3] Tom WJ Scheenen, Dennis WJ Klomp, Jannie P Wijnen, and Arend Heerschap. Short echo time ^{1}H-MRSI of the human brain at 3T with minimal chemical shift displacement errors using adiabatic refocusing pulses. *Magnetic resonance in medicine*, 59(1):1–6, 2008.

[4] Douglas L Rothman, Henk M De Feyter, Robin A Graaf, Graeme F Mason, and Kevin L Behar. ^{13}C MRS studies of neuroenergetics and neurotransmitter cycling in humans. *NMR in biomedicine*, 24(8):943–957, 2011.

[5] Wei Chen, Xiao-Hong Zhu, Rolf Gruetter, Elizabeth R Seaquist, Gregor Adriany, and Kamil Ugurbil. Study of tricarboxylic acid cycle flux changes in human visual cortex during hemifield visual stimulation using ^{1}H-{^{13}C} MRS and fMRI. *Magnetic resonance in medicine*, 45(3):349–355, 2001.

[6] Pratip Bhattacharya, Eduard Y Chekmenev, William H Perman, Kent C Harris, Alexander P Lin, Valerie A Norton, Chou T Tan, Brian D Ross, and Daniel P Weitekamp. Towards hyperpolarized ^{13}C-succinate imaging of brain cancer. *Journal of magnetic resonance*, 186(1):150–155, 2007.

[7] Małgorzata Marjańska, Isabelle Iltis, Alexander A Shestov, Dinesh K Deelchand, Christopher Nelson, Kâmil Uğurbil, and Pierre-Gilles Henry. In vivo ^{13}C spectroscopy in the rat brain using hyperpolarized [1-^{13}C] pyruvate and [2-^{13}C] pyruvate. *Journal of Magnetic Resonance*, 206(2):210–218, 2010.

[8] Graeme F Mason, Kitt Falk Petersen, Robin A de Graaf, Tomoyuki Kanamatsu, Taisuke Otsuki, and Douglas L Rothman. A comparison of ^{13}C NMR measurements of the rates of glutamine synthesis and the tricarboxylic acid cycle during oral and intravenous administration of [1-^{13}C] glucose. *Brain research protocols*, 10(3):181–190, 2003.

[9] Jannie P Wijnen, Marinette Van der Graaf, Tom WJ Scheenen, Dennis WJ Klomp, Bastiaan E de Galan, Albert JS Idema, and Arend Heerschap. In vivo

^{13}C magnetic resonance spectroscopy of a human brain tumor after application of ^{13}C-1-enriched glucose. *Magnetic resonance imaging*, 28(5):690–697, 2010.

[10] Stefan Blüml, Angel Moreno-Torres, and Brian D Ross. [1-^{13}C] glucose MRS in chronic hepatic encephalopathy in man. *Magnetic resonance in medicine*, 45(6):981–993, 2001.

[11] Alexander P Lin, Frederick Shic, Cathleen Enriquez, and Brian D Ross. Reduced glutamate neurotransmission in patients with Alzheimer's disease - an in vivo ^{13}C magnetic resonance spectroscopy study. *Magnetic Resonance Materials in Physics, Biology and Medicine*, 16(1):29–42, 2003.

[12] Ognen AC Petroff, Laura D Errante, Douglas L Rothman, Jung H Kim, and Dennis D Spencer. Glutamate–glutamine cycling in the epileptic human hippocampus. *Epilepsia*, 43(7):703–710, 2002.

[13] Stefan Blüml, Angel Moreno, Jong-Hee Hwang, and Brian D Ross. 1-^{13}C glucose magnetic resonance spectroscopy of pediatric and adult brain disorders. *NMR in biomedicine*, 14(1):19–32, 2001.

Appendix

The evolution of the coherence pathway that yields S_{A1} shown in Eq. 4.1 will be explained, in order to show the use of the product operator formalism in the derivations presented in Chapter 4. The density operator of A spins at time point 0^-, i.e., before the application of any pulse, is given by:

$$\rho\left(0^-\right) = A_z. \tag{1}$$

The application of the first 90° pulse will result in a rotation around the x axis, yielding a single-quantum coherence:

$$\rho\left(0^+\right) = -A_y. \tag{2}$$

The chemical shift evolution during the first echo time (TE)/2 interval is denoted as follows:

$$\rho = -A_y cos\left[\frac{\Omega_A TE}{2} + \gamma\left(G_1 \cdot r\right) t_1\right] + A_x sin\left[\frac{\Omega_A TE}{2} + \gamma\left(G_1 \cdot r\right) t_1\right], \tag{3}$$

where the dephasing given by the phase in the brackets is due to the chemical shift of the spin relative to the transmit frequency (Ω) and to the gradient of strength G_1 (Figure 3.11) with duration t_1 that affects location r.

The J-coupling evolution during the same interval is calculated cumulatively for n pairs of spins, starting from $n = 1(AX_1)$:

$$\begin{aligned}\rho = &- A_y cos\left[\frac{\Omega_A TE}{2} + \gamma\left(G_1 \cdot r\right) t_1\right] cos\left(\frac{\pi JTE}{2}\right) + 2A_x X_{1z} cos\left[\frac{\Omega_A TE}{2} + \gamma\left(G_1 \cdot r\right) t_1\right] sin\left(\frac{\pi JTE}{2}\right) \\ &+ A_x sin\left[\frac{\Omega_A TE}{2} + \gamma\left(G_1 \cdot r\right) t_1\right] cos\left(\frac{\pi JTE}{2}\right) + 2A_y X_{1z} sin\left[\frac{\Omega_A TE}{2} + \gamma\left(G_1 \cdot r\right) t_1\right] sin\left(\frac{\pi JTE}{2}\right).\end{aligned} \tag{4}$$

At the end of first TE/2 interval and after considering the n^{th} pair, the spin density operator is given by:

$$\rho\left(\frac{TE^{-}}{2}\right) = 2sin\left(\frac{\pi JTE}{2}\right)cos^{n-1}\left(\frac{\pi JTE}{2}\right)X_z\left\{\begin{array}{l} A_x cos\left[\frac{\Omega_A TE}{2} + \gamma\left(G_1 \cdot r\right)t_1\right] \\ +A_y sin\left[\frac{\Omega_A TE}{2} + \gamma\left(G_1 \cdot r\right)t_1\right] \end{array}\right\}, \tag{5}$$

where only terms with $X_z A_x$ and $X_z A_y$ remain, as explained in subsection 4.2. Note that $X_{1z} + ... + X_{nz} = X_z$, and so on.

After the application of the second radiofrequency pulse, the previous equation is transformed into:

$$\rho\left(\frac{TE^{+}}{2}\right) = -2X_y A_x sin\left(\frac{\pi JTE}{2}\right)cos^{n-1}\left(\frac{\pi JTE}{2}\right)cos\left[\frac{\Omega_A TE}{2} + \gamma\left(G_1 \cdot r\right)t_1\right], \tag{6}$$

where only zero-quantum coherences were preserved. At the end of the mixing time (TM) period, the expression for the spin density operator is:

$$\rho\left(\frac{TE^{-}}{2} + TM^{-}\right) = -2sin\left(\frac{\pi JTE}{2}\right)cos^{n-1}\left(\frac{\pi JTE}{2}\right)cos^{n-1}\left(\pi JTM\right)\left\{\begin{array}{l} X_y A_x cos\left(\Omega_A TM\right)cos\left(\Omega_X TM\right) \\ -X_x A_x cos\left(\Omega_A TM\right)sin\left(\Omega_X TM\right) \\ +X_y A_y sin\left(\Omega_A TM\right)cos\left(\Omega_X TM\right) \\ -X_x A_y sin\left(\Omega_A TM\right)sin\left(\Omega_X TM\right) \end{array}\right\}$$
$$\times cos\left[\frac{\Omega_A TE}{2} + \gamma\left(G_1 \cdot r\right)t_1\right]. \tag{7}$$

When applying the final 90° pulse, only single-quantum coherence terms observable at the X resonance are maintained, as given in:

$$\begin{array}{l} \rho\left(\frac{TE}{2} + TM^{+}\right) = 2X_x A_z sin\left(\frac{\pi JTE}{2}\right)cos^{n-1}\left(\frac{\pi JTE}{2}\right)cos^{n-1}\left(\pi JTM\right)sin\left(\Omega_A TM\right)\sin\left(\Omega_X TM\right) \\ \times cos\left[\frac{\Omega_A TE}{2} + \gamma\left(G_1 \cdot r\right)t_1\right]. \end{array} \tag{8}$$

Combining the effects of the chemical shift and J-coupling evolution during the last TE/2 interval, it is possible to obtain the expression for terms that contain X_y, as they are the ones detected at the end of the stimulated echo acquisition mode (STEAM) sequence:

$$\begin{array}{l} \rho\left(TE + TM\right) = sin^2\left(\frac{\pi JTE}{2}\right)cos^{n-1}\left(\frac{\pi JTE}{2}\right)cos^{n-1}\left(\pi JTM\right)sin\left(\Omega_A TM\right)sin\left(\Omega_X TM\right) \\ \times cos\left[\frac{\Omega_A TE}{2} + \gamma\left(G_1 \cdot r\right)t_1\right]cos\left[\frac{\Omega_X TE}{2} + \gamma\left(G_3 \cdot r\right)t_3\right]. \end{array} \tag{9}$$

Subsequently, the following trigonometric identity is used on the terms that contain the dephasing gradients:

$$cos\left[\frac{\Omega_A TE}{2}+\gamma\left(G_1\cdot r\right)t_1\right]cos\left[\frac{\Omega_X TE}{2}+\gamma\left(G_3\cdot r\right)t_3\right]=\frac{1}{2}\left\{cos\left[\frac{\Delta\Omega TE}{2}+\gamma\left(G_1\cdot r\right)t_1-\gamma\left(G_3\cdot r\right)t_3\right]\right.$$
$$\left.+cos\left[\frac{\left(\Omega_A+\Omega_X\right)TE}{2}+\gamma\left(G_1\cdot r\right)t_1+\gamma\left(G_3\cdot r\right)t_3\right]\right\}. \tag{10}$$

As the measured single-quantum signal is proportional to the transverse magnetisation integrated over the volume-of-interest, any spatial dependency will be nulled, due to incoherent phase accumulation. Taking also into account that the dephasing created by both G_1 and G_3 is the same, the final expression is given by:

$$S_{A1}\left(TE+TM\right)=\frac{1}{4}sin^2\left(\frac{\pi JTE}{2}\right)cos^{n-1}\left(\frac{\pi JTE}{2}\right)cos^{n-1}\left(\pi JTM\right)cos\left(\Delta\Omega TM\right)cos\left(\frac{\Delta\Omega TE}{2}\right). \tag{11}$$

To express $\Delta\Omega$ in Hz, Eq. 11 is transformed into S_{A1} of Eq. 4.1:

$$S_{A1}\left(TE+TM\right)=\frac{1}{4}sin^2\left(\frac{\pi JTE}{2}\right)cos^{n-1}\left(\frac{\pi JTE}{2}\right)cos^{n-1}\left(\pi JTM\right)cos\left(2\pi\Delta\Omega TM\right)cos\left(\pi\Delta\Omega TE\right). \tag{12}$$